MICROSTRUCTURAL STUDY OF LASER-INDUCED RAPID LATERAL SOLIDIFICATION OF METAL THIN FILMS

by

Rong Zhong

BS, Material Science and Engineering, Zhejiang University, 1999

MS, Material Science and Engineering, Institute of Metal Research, Chinese Academy of Sciences, 2002

Submitted to the Graduate Faculty of

Swanson School of Engineering in partial fulfillment

of the requirements for the degree of

Doctor of Philosophy

University of Pittsburgh

2010

UNIVERSITY OF PITTSBURGH

SWANSON SCHOOL OF ENGINEERING

This dissertation was presented

by

Rong Zhong

It was defended on

April 6th, 2010

and approved by

John A. Barnard, PhD, Professor, Department of Mechanical Engineering and Materials Science, Swanson School of Engineering

Judith C. Yang, PhD, Associate Professor, Department of Mechanical Engineering and Materials Science, Swanson School of Engineering

Jörg M. K. Wiezorek, PhD, Associate Professor, Department of Mechanical Engineering and Materials Science, Swanson School of Engineering

James W. McCamy, PhD, Sr. Research Associate, Glass Technology Center, PPG Inc.

Dissertation Director: John P. Leonard, PhD, Assistant Professor, Department of Mechanical Engineering and Materials Science, Swanson School of Engineering

MICROSTRUCTURAL STUDY OF LASER-INDUCED RAPID LATERAL SOLIDIFICATION OF METAL THIN FILMS

Rong Zhong, Ph.D.

University of Pittsburgh, 2010

Solidification is a common process used in the manufacture of bulk metals, and is fundamentally a phase transformation from liquid to solid that has been studied for many years. A lot of fundamental theories of solidification under near equilibrium conditions have been developed and are widely accepted. In the case of rapid solidification, which is characterized by rapid heat loss and a high interface velocity, non-equilibrium conditions prevail and are not yet understood very well. Due to the promising properties of new alloys and microstructures produced by rapid solidification, industrial interest in this process remains strong. As the present theories of solidification are mainly based on equilibrium conditions, there is strong motivation for developing new theories that explain the solidification behavior under non-equilibrium conditions. In this research, we present experimental results of rapid lateral solidification under the newly geometric heat flow and growth direction, and address critical questions associated with the current theories. This includes identification and quantification of mechanisms governing defect generation and texture formation.

In this research, a pulsed excimer laser was applied as an energy source to melt thin film metallic multilayers of Cu, Cu-Nb, Ag and Au. This leaded to rapid resolidification upon cooling, and unique solidification microstructures. Using this technique, we were able to successfully prepare RLS (rapid lateral solidification) microstructures that were reproduceable and controllable through the laser process parameters. Much of the work presented here was an investigation of the rapid solidification process indirectly by examination of the post-solidified microstructure using electron microscopy. In this thesis we have quantitatively studied several aspects of the microstructure, including:

- Microstructure of four zones formed during rapid solidification
- Mechanism of texture selection
- Stacking fault density versus solidification velocity

It is believed that the microstructure and defects formed in rapid solidification are affected by the thermal gradient and by the high solidification velocity. Based on these experimental results, we are now able to address a number of open questions relating to orientation selection, kinetics of defect formation, S-L interfacial stability, and heat flow in RLS.

TABLE OF CONTENTS

LIST OF TABLES

LIST OF FIGURES

PREFACE

To

My Parents and my Sister

And all my

Advisors

1.0 INTRODUCTION

Solidification is the phase transformation from liquid to solid as the system temperature is decreased. The conditions under which solidification takes place play a significant role in determining the properties of the resulting solid. Some characteristics of metals may be controlled by changing the solidification velocity, adding solute atoms, controlling the grain size and so on. In particular, increasing the solidification velocity affects the microstructure of the resulting solid in multiple ways, including the phase, defect density, grain size and the incorporation of solute atoms. Rapid solidification is a solidification process during which the temperature decreases at a rate of more than 100 K/s and interface velocity is higher than 1 cm/sec. [**1**,**2**]

Laser processing has many advantages as compared with other rapid solidification processes due to its special properties. Lithographic techniques can be used in laser processing, allowing for easy and inexpensive pattern design using tools and processes already present in the electronic industry. A pulsed excimer laser can provide a rapid, uniform and adjustable energy source for solidification research of non-equilibrium and annealing treatment.

1.1 TECHNIQUES FOR SOLIDIFICATION

There are many techniques of solidification including casting, spray, spinning, laser melting and so on. These techniques may be divided into two broad classes: constrained solidification, where the growth direction and the velocity are constrained by heat flow; and free solidification, where the solid can grow freely in every direction into the supercooled liquid. Solidification techniques may also be defined by solidification velocity. When the temperature decreases at a rate greater than 100 K/s and the interface velocity is higher than 1 cm/s, the process is called rapid solidification. [**2**]

The most common solidification techniques are introduced below, along with a discussion of their characteristics including the growth direction (GD), which is defined as the travel direction of the S-L

(solid-liquid) interface, the heat flux direction (Q) from high temperature to low temperature, and the microstructure formation.

1.1.1 Constrained Solidification (GD in the Opposite Direction of Q)

In the listed techniques of constrained solidification, the GD and S-L interface velocity are constrained by Q, where GD is always found in the opposite direction of Q.

1.1.1.1 Casting and Ingot from Overheated Liquid

Castings and ingots are an effective method to manufacture bulk metallic structures and have been studied extensively [**1**]. In general, three solidification zones in ingots and castings can be distinguished, as shown in Figure 1(b): (I) Chill zone of equiaxed crystals, II) Columnar zone of column-like grains and III) Equiaxed zone by nucleation.

After the liquid is poured into the mould, heat is transferred outward from the liquid to the mould wall, where the heat flux rate is determined by the temperature gradient, heat transfer coefficient and the thermal conductivity of the mold (shown in Figure 1(a)). At first, a relatively thin layer of chill zone (I) microstructure is produced at the interface between the liquid and mould wall because of nucleation (rapid appearance of many crystals in the liquid) during the rapid cooling process. Secondly, the columnar zone (II) is formed and extends into the liquid. Thirdly, as the heat transfers outward continuously and the temperature decreases, an equiaxed zone (III) is produced at the end of solidification, typically by heterogeneous nucleation where the nuclei are the small particles dropped from the sub-dendritic tips formed in zone II. In fact, the equiaxed zone (III) is typically absent in the pure metals and prevails in alloys.

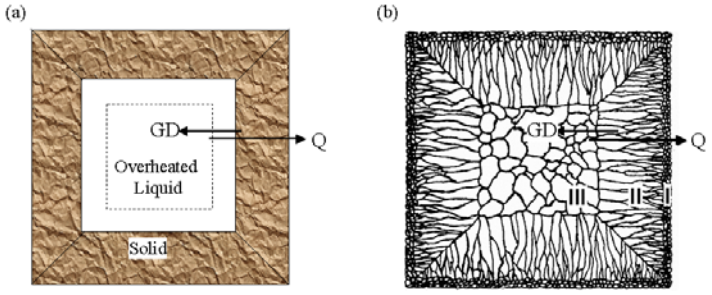

Figure 1. (a) Constrained solidification process of casting; (b) Microstructure of three zones in the casting: I. chill zone of equiaxed crystals; II. columnar zone of elongated grains; III. central equiaxed zone by nucleation [**1**].

1.1.1.2 Melt Spinning

The melt spinning method shown in Figure 2(a) can be used to fabricate ribbons by rapid solidification. Here the molten metal drops on a drum rotated at high velocity and forms a thin layer [**5**]. Because the drum is continuously cooled and the thickness of the liquid is very small, the heat is mainly transferred to the drum and the ribbon forms immediately at the point of initial contact.

As shown in Figure 2(b), the solidification starts at the contact interface of the liquid and the drum with a high supercooling temperature and grows in a direction opposite to that of the heat transfer (Q). The solidification velocity is the maximum at the beginning and then decreases due to the decreasing of heat transfer and recalescence. However, both of these effects are weak enough to maintain a low supercooling temperature and therefore a high growth velocity.

The microstructure of melt spinning is shown in Figure 2(c) where the chill zone is initially formed at the interface of the drum and the liquid, and then the columnar grains grow upward from the chill zone. [**6**]

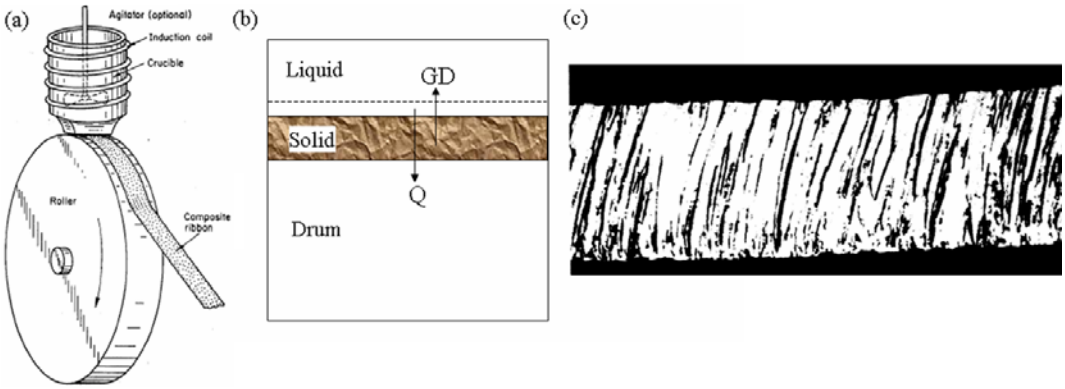

Figure 2. (a) Schematic illustration of spinning process [**5**]; (b) Constrained solidification: the solid forms firstly at the interface of the drum and the liquid; (c) Microstructure of a 50 μm copper ribbon which was spun at about 35 ms^{-1} [**6**].

1.1.1.3 Beam Melting of Bulk Metals

A schematic of the surface melting process is shown in Figure 3(a), where the surface of the metal bulk is melted by a single pulse or continuous traversing heat source of a laser or electron beam [**2**]. The depth of melting is controlled by the amount of applied energy. These thin molten layers typically solidify via rapid solidification upward as the heat is transferred downward into the bulk very rapidly as shown in Figure 3(b). Although the heat transfer and GD here are similar to the spinning technology, the

solidification starts with the seeds provided by the original metal bulk but not with a chill zone initiated by nucleation.

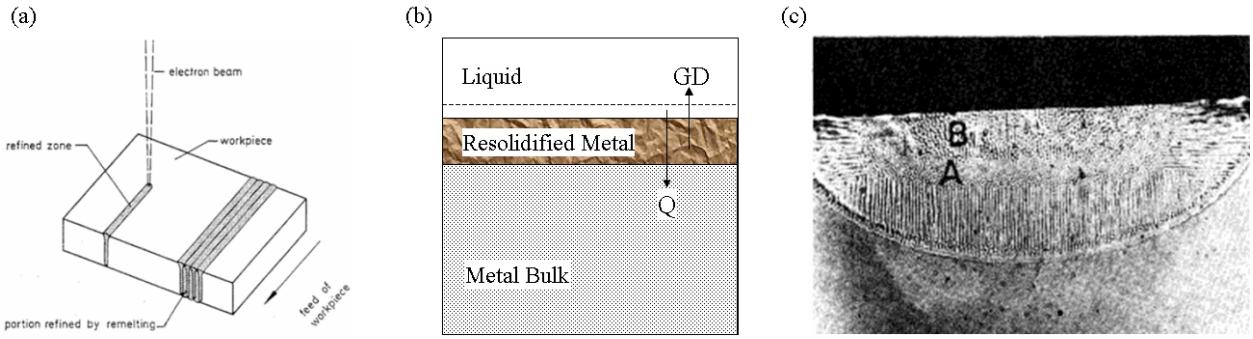

Figure 3. (a) Schematic illustration of the bulk melted by laser beam [2]; (b) Constrained solidification: the original bulk provides the seeds for the resolidification; (c) Microstructure of the resolidified laser melted region in Ni-based alloy [7].

The typical microstructure in the laser melted regions of a Ni-based alloy is shown in Figure 3(c), where the thermal gradient develops a large component along the heat transfer direction [**7**]. In this example, the solidification occurs by the growth of the cellular dendrites (A) with the seeds, i.e., crystals of the crystals provided by the Ni-based alloy bulk, which is competing with the equiaxial regrowth of the substrate. Near the top of the melt pool, the equiaxed zone (B) is formed due to the alloy constituents.

1.1.2 Free Solidification (GD in the Same Direction of Q)

In the listed techniques of free solidification, the solid can grow freely to the liquid where GD is always found is the same direction of Q.

1.1.2.1 Fluxing of Supercooled Liquid

Another method to produce bulk metal ingots uses a highly supercooled liquid and rapid solidification. Here, a metallic liquid is kept in a silica crucible and covered by a soda-glass slag, and the temperature of the liquid is continuously reduced. Because the interface of the silica crucible is typically very inert with respect to nucleation, a chill zone is not formed at the surface of the silica crucible. If the purity of the metal is very high, this will also suppress the heterogeneous nucleation effects in the pool, and thus a highly supercooled liquid can be formed.

As shown in Figure 4(a), a nucleus will appear in the supercooled liquid and grow outward spontaneously to the liquid. The growth velocity is highest at the beginning of the solidification as the heat is mainly released to the supercooled liquid in front of the S-L interface. This rapid solidification process is classified as the free solidification [**3**] in which the heat flux (Q) direction is the same as the GD. Here recalescence, the released heat to the liquid because of solidification process, is very strong and decreases the movements of the S-L interface.

The typical microstructure of the ingot synthesized with a highly supercooled liquid is shown in Figure 4(b) [**3**], where all of the subgrains were generated from a single nucleus appeared in the right side. The supercooling temperature in this copper ingot reached as high as 207 °C before the nucleation.

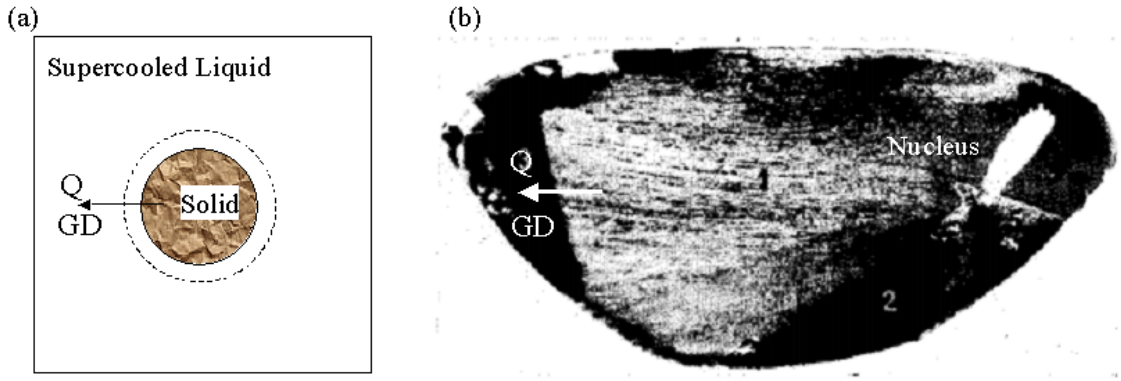

Figure 4. (a) Free solidification: a nucleus is formed in the supercooled liquid; (b) Microstructure of the copper ingot supercooled by 207 °C and grew up from the nucleus in the right side [**3**].

1.1.2.2 Droplet Supercooling

Here tiny droplets of liquid are formed as a spray by using a highly velocity gas jets (Figure 5 (a)) [**2**]. The temperature of the fine liquid droplets decreases rapidly, and a high supercooling temperature is reached. As with fluxed supercooling, nuclei form in the supercooled liquid and grow rapidly. This is also classified as a free solidification process.

Figure 5(b) schematically shows this solidification process, where a nucleus is formed near the surface of the supercooled liquid because the temperature is lowest or there may be surface impurities present. During the growth of this nucleus, the heat (Q) is transferred into the supercooling liquid in the same direction as GD.

The microstructure of particles fabricated by spray is shown in Figure 5(c) [**4**].

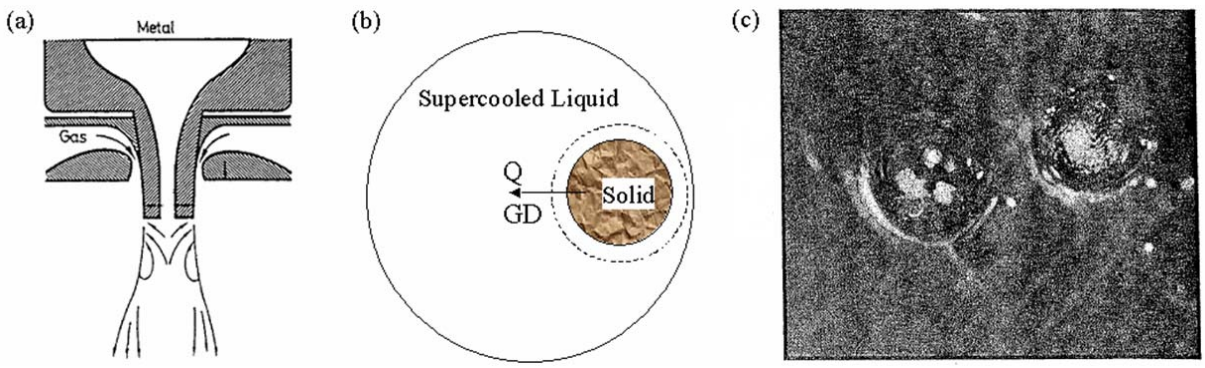

Figure 5. (a) Schematic illustration of spray used in the rapid solidification [**2**]; (b) Free solidification: a nucleus is formed in the supercooled liquid; (c) Microstructure of Au droplet solidified at 830 ℃ [**5**].

1.1.3 Constrained Solidification (QD Perpendicular to Q)

The bulk metal described in section 1.1.1.3 can be replaced by multiple thin films but with the same application of the energy source as shown in Figure 6(a) [**2**]. However, after the laser melts the metal film between the two capping layers, the heat mainly transfers downward into the substrate, but the GD is perpendicular to the heat transfer direction and parallel with the surface (shown in Figure 6(b)). The rapid solidification starts from the seeds of the original crystals in the metal film and grows laterally to the center of the liquid pool. The supercooling temperature at the beginning of the solidification is zero and then decreases rapidly due to the special direction of the heat transfer and the small thickness of the metal film. Here the growth velocity is zero at the beginning and then proceeds faster and faster.

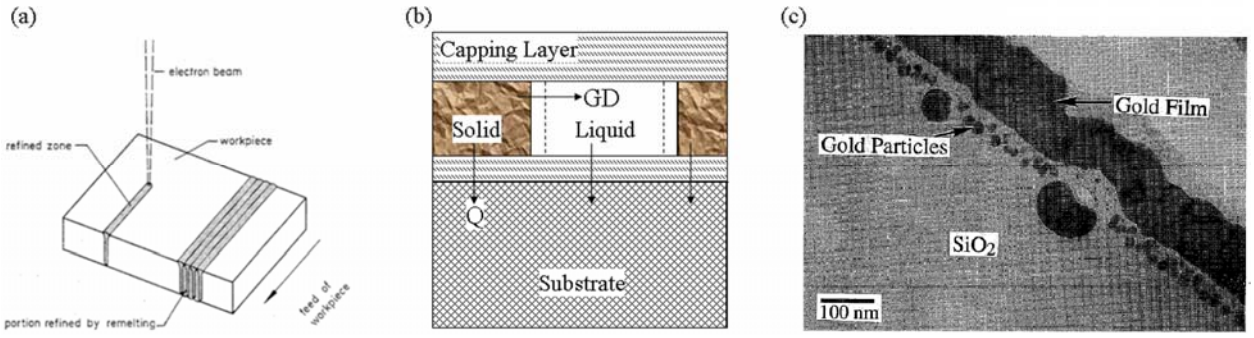

Figure 6. (a) Schematic illustration of the multiple films melted by laser beam [2]; (b) Constrained solidification: the original bulk provides the seeds for the resolidification; (c) Microstructure of RLS (rapid lateral solidification): Au capped between SiO_2. [6]

This technique, corresponding to our rapid lateral solidification (RLS) process [**3**, **6**, **7**], is unique in that it is the only process where Q and GD are perpendicular. RLS is currently only possible in selected metals, and limiting the roughness of films is very important for the success of RLS. The capping layers used here are silica, which is inert to nucleation and prevents dewetting of the film [**3**, **7**].

1.2 TEXTURE FORMATION IN SOLIDIFICATION OF PURE METALS

Directional solidification of metals is obtained by various processes such as casting, rapid quenching on a cold surface, or beam melting. Solidification proceeds by the advance of a liquid-solid interface into the molten phase, producing various microstructures ranging from a single crystal to a fine equiaxed microstructure, depending on the composition, rate of heat extraction and interfacial stability. Under certain conditions, long parallel crystallites can extend along the solidification growth direction to form a columnar microstructure. Often these grains have a preferred orientation, or solidification texture, relative to the growth direction. Frequently, solidification texture is the result of a competitive occlusion process with less preferred orientations, where grains with preferred orientation are allowed to expand laterally at the expense of neighboring grains as the solidification front advances. The origins of this texture have been of technical and fundamental interest for many decades [8-10] but a comprehensive understanding of this process remains elusive.

In directional solidification of pure FCC metals, composition effects are absent, and a predominant <001> growth texture has been observed in Cu [3, 6, 11, 12], Al [8, 13], Bi [14], and Pb [8, 15]. This is found across many orders of magnitude in solidification velocity, suggesting that solidification along the <100> direction is both kinetically and energetically favored. The association of the <100> texture with thermal dendrites is well known [15, 16]. Interfacial stability theory for pure metals [17, 18] suggests a weak anisotropy may be present through orientation-dependent interfacial energy, or in the case of slow solidification, determined by facet and defect anisotropy [1, 19].

At sufficient velocities and undercooling for FCC metals, the S-L interface becomes atomistically rough [1, 19], so that the thermal dendritic instability, if present, can only depend on heat flow and must therefore be isotropic. It thus remains an open question how the <100> texture can arise in these rapidly solidified materials. Recently, atomistic models of the thermodynamics [10, 20] and kinetics [21] in pure FCC metal solidification suggest there is a preferred <100> growth orientation but the lack of further experimental data has prevented further advances.

1.3 RAPID LATERAL SOLIDIFICATION (RLS)

Rapid lateral solidification (RLS) is a type of laser melting and rapid solidification, but with some important geometric and thermal differences as shown schematically in Figure 7. In this work, the multilayer configuration consists of a layer of 200 nm metal film sandwiched between two SiO_2 films on a Si substrate. These SiO_2 films are used to maintain a confined environment for the metal solidification and prevent the oxidation or dewetting of the metal film [**3**, **7**]. A single excimer laser pulse with approximately 28ns duration is applied to heat the sample and the energy is absorbed by the metal film. The shape of the melted region is controlled by the mask to choose a very small central area of laser beam with high quality where the energy density is uniform. With a 5X demagnification, the laser forms a narrow line 5-60 μm wide on the sample where a small pool of metal liquid is generated as shown in Figure 7(a). This is identified as the complete melting region, where the metal film is melted through its entire thickness. After the termination of the pulse, the temperature of this metal liquid decreases rapidly because the heat is conducted downward into the colder substrate.

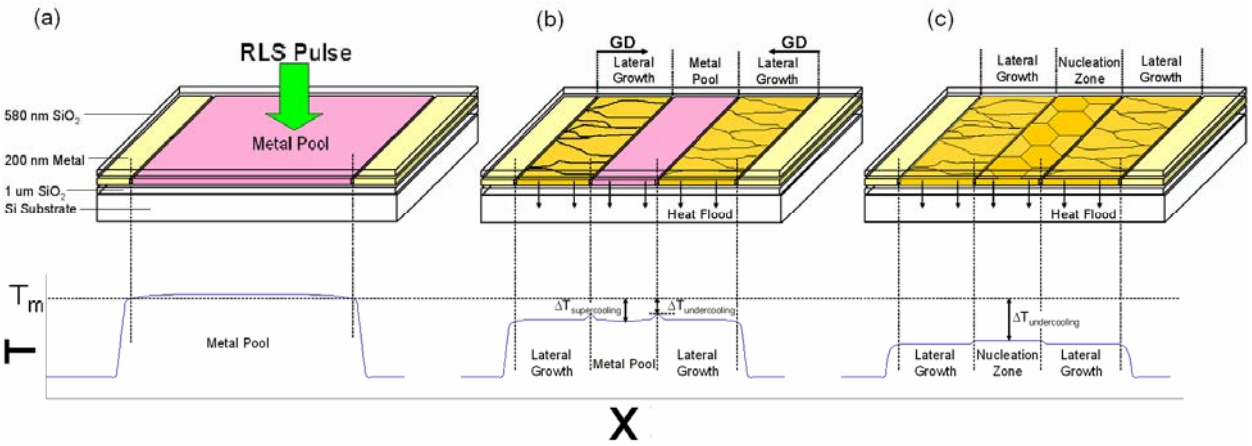

Figure 7. Model of rapid resolidification process: (a) The temperature of liquid metal hits the melting temperature (T_m) and rapid resolidification starts at the pool edge; (b) The S-L interface moves to the center and a lateral growth zone forms; (c) The supercooling temperature reaches the maximum and a nucleation zone is generated in the center.

Solidification starts at the pool edge and continues laterally to the center very rapidly. The result is a solidification microstructure formed with an initially zero velocity but accelerated toward the center (Figure 7(b)). During this process, latent heat is released at the solid-liquid (S-L) interface, raising the local temperature as shown in the schematic profile. When the S-L interface moves laterally toward the

center, parallel grains are formed in what is called the lateral growth zone. Here the undercooling temperature ($\Delta T_{undercooling}$) of the S-L interface increases because the heat transfers continually to the Si substrate. Therefore, the velocity of S-L interface can become higher and higher due to the kinetic relationship in rapid solidification [**1**, **2**]:

$$v_{interface} \approx \mu(T_{interface} - T_m) = \mu\Delta T_{undercooling} \qquad \textbf{Equation 1}$$

But away from the interface the temperature of the liquid is lower, and a high supercooling temperature ($\Delta T_{supercooling}$) can be reached in the liquid metal. If the supercooling temperature ($\Delta T_{supercooling}$) in the central liquid pool reaches a critical value, crystal nuclei can appear and result in a nucleation zone formed in the central area shown in Figure 7(c). RLS terminates when the opposing solidification fronts meet in the middle, or when they encounter this nucleation zone.h

The timescale of the RLS is estimated from simulations to be less than 400 ns, and the maximum quenching rate in the pool to be $10^7 \sim 10^{10}$ K/s, depending on the laser and film conditions. The solidification velocity is estimated to exceed 100 m/s. During RLS, the heat flow is primarily downward and perpendicular to the growth direction (GD). This geometry makes the system different than other rapid solidification methods, and given the presently estimated quench rates and velocities it is believed that the S-L interface is kinetically limited. These conditions and the presence of a laterally moving interface make this system ideal for rapid solidification research.

The grains formed in RLS can reach up to 25 μm in length and 1 μm width with a 200 nm thickness film, which is difficult be fabricated by other technologies. Due to their special shape, lower defect densities and fewer grain boundaries than as-deposited metal films, these materials may have applications in the electronics industry as interconnects with high conductivity and low electromigration. This would be a significant improvement over the presently used electrodeposited film containing an abundance of pinholes, grain boundaries and dislocations.

1.3.1 Heat Flow Effects of Rapid Solidification

The technology and fundamentals of the solidification process in pure metals is provided in detail in Chapter 2. In most previous experiments in the literature, the heat flow is parallel with the direction of solidification (shown in Figure 8(a) and (b)), which has very important effects on the solidification processes, such as recalescense and interfacial instability. When the latent heat is released into the liquid, the temperature of liquid will increase and reduce the S-L interface velocity, i.e. the solidification velocity. This effect is defined as recalescence [**22**], and this heat must be conducted into the solid or the liquid. It

is well known that there is instability in an interface moving into a supercooled liquid [**1**] in free solidification shown in Figure 8(b). This instability is known as a thermal dendritic instability and is thought to generate undulations or protrusions in the S-L interface that affect the microstructure and texture of the solidified material. Changes in the liquid temperature gradient affect the degree of instability in the S-L interface.

However in the current research as shown in Figure 8(c), the RLS geometry is different with other solidification techniques. During RLS, GD is classified to the constrained solidification in the micrometer scale. Here in the micrometer scale, the GD of solidification is perpendicular to the overall heat flow Q, i.e. the GD pointes from solid to liquid and Q is released into the substrate. But in the nanometer scale, RLS is a type of free solidification, where Q is released from the moving S-L interface and conducted locally forward into the liquid and backward into the cooling solid.

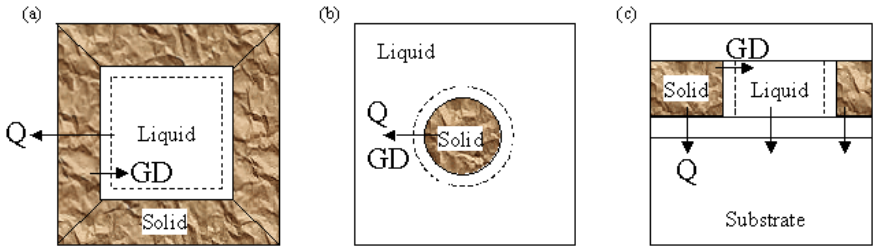

Figure 8. (a) Constrained solidification: in casting, ingot or spinning solidification; (b) Free solidification: in equiaxed zone of ingots or droplet solidification; (c) Constrained solidification of RLS ((rapid lateral solidification): in multiple-film solidification.

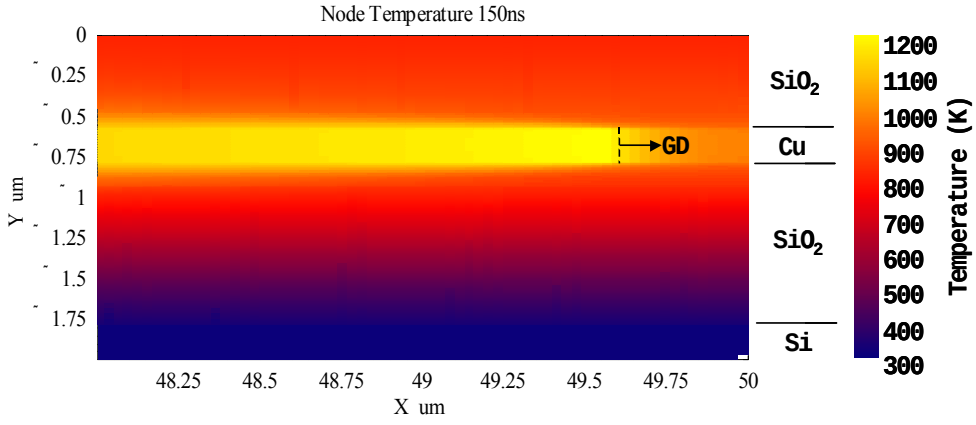

Figure 9. Temperature field calculated for rapid lateral solidification of Cu thin film using 3DNS. Dashed line indicates position of S-L interface.

The simulation of the heat profile in the nanometer scale in RLS samples are shown in Figure 9, where most heat is absorbed by Cu film and the highest temperature (1200 K) is reached there. The top SiO_2 layer is heated up to about 900 K, but the temperature of the bottom SiO_2 layer decreases rapidly from about 900 K to room temperature. The simulation shows that during RLS, the temperature of the S-L interface is higher than both the solid and liquid, thus heat flows from the S-L interface into both the solid and liquid. At the same time, heat transfers into the substrate and therefore avoids recalescense.

In the micrometer scales the thermal gradient remains perpendicular to the S-L interface. And in the nanometer scales the thermal gradient is negative in both solid and liquid. This likely suggests that Q affects the stability/instability of the S-L interface in a weaker way than other techniques, but at this time direct observation of the moving interface is not possible in experiment.

1.3.2 Microstructure in Pure Metal Thin Films Processed by RLS

An examination of RLS microstructure reveals several zones with different characteristics. The grains formed at the beginning of RLS appear to be unstable because growth of most of the grains is terminated as solidification proceeds. This is called the occlusion zone (zone I). After this stage, the remaining grains grow in a columnar morphology in the columnar zone (zone II); here the size and the microstructure of the grains changes little. In Cu films, we find another unstable zone (zone III) at the end of RLS, and some grains appear to form a fan shape while the others disappear. An abundance of dislocations are generated in zone III and grain boundaries become unclear. In wide melt zone lines a region (zone IV) of equiaxed grains is found in the center of the solidified region. This is consistent with nucleation of grains in the supercooled melt pool, and meets with zone III at the end of RLS.

A microstructural analysis of Cu and Ag films shows that most of the grains formed in RLS choose a similar orientation in the growth direction, i.e. strong textures are detected. Also, the stacking fault densities in Cu and Ag films have been estimated on the basis of the transmission electron microscopy (TEM) techniques. Statistical studies of many grains can provide information on texture grain size evolution during growth. A SEM-EBSD characterization technique has now been successfully adapted to this study of RLS microstructures, and the data are presented in the results sections below. Besides the ribbon geometry, the texture formed in the grains by RLS microstructures may be another advantage for application.

An example of the RLS structure of copper films is shown in Figure 9. The four zone microstructure will be introduced and discussed in details in Chapter 3.0.

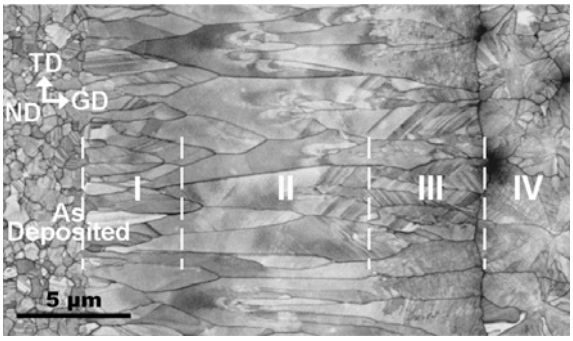

Figure 10. The microstructure of copper films formed in RSL.

1.4 SUMMARY

As discussed earlier, solidification can be classified into three basic types. Constrained solidification in Figure 8(a) prevails in the directional growth of castings, ingots and spinning, where the heat, Q, transfers from the liquid to the solid and opposes the growth direction (GD). Therefore, the temperature gradient is positive and thermal dendritic formation is suppressed. During this process, if the heat transfer rate is lower than the rate of release of latent heat of solidification, the S-L interface velocity is limited by the heat diffusion process and will proceed without undercooling. If the heat transfer rate is higher than the rate of latent heat release, the S-L interface velocity may increase and be kinetically limited, obeying the interface response function with undercooling, such as with the thin layer solidification in spinning.

Free solidification (Figure 8(b)) occurs during the growth of solid nuclei in the supercooled liquid, such as the equiaxed zone of ingots or droplet solidification, where a nucleus appears in the supercooled liquid and grows outward freely. In free solidification, the heat transfer direction is coincident with the GD. Heat flows from the solid into the liquid and causes recalescence, which decreases the growth velocity. So, the temperature gradient here is negative, and thermal dendrites can be formed at the unstable interface. During this process, the S-L interface velocity can be limited by the heat diffusion or kinetically limited by the interface response function when undercooled.

Our RLS process is shown schematically in Figure 8(c) where the metal film is sandwiched between two layers of SiO2 on a substrate of bulk Si. Because the thickness of the metal film can be decreased to nanometers, the recalescence effect is limited and most of the heat flux is mainly transferred downward to the silicon substrate. In this condition, the GD is perpendicular to the heat transfer direction. Therefore, the temperature in the S-L interface can be much higher than the solid or liquid because of heat latent

release. On the micrometer scale, however, we note that heatflow may also occur into the supercooled liquid forward along GD, which raises the possibility of thermal dendritic formation as in free solidification. In this way we describe RLS as constrained overall by the heat diffusion process downward in macro scale, but locally at the interface it is a type of free solidification. During RLS, the S-L interface velocity typically increases, changing from the heat diffusion limited conditions to the interface response function (kinetic) limited conditions and experiences ever higher interfacial high undercooling.

For these reasons, RLS provides a unique experimental geometry to study the fundamentals of rapid solidification. The ability to prepare high purity metal thin films, melted by the excimer laser provides new information for the study of texture formation, dislocation activation and S-L interface movement with the limited recalescence and the special heat transfer conditions.

2.0 EXPERIMENTAL

Copper is a widely used as a metallization material in the electronics industry because of its low electrical resistivity and low electromigration effects [**23**-**27**], while silver is being considered for future interconnect technologies. Gold is less commonly used in applications, but is of fundamental interest in physical metallurgy due to its non-reactive nature. Overall the fundamental properties of these FCC metals have been thoroughly researched, so that properties, defect behavior and microstructural evolution in these thin films are known and understood very well. Together, these reasons make Cu, Ag and Au appealing materials for new research to explore unanswered scientific questions associated with rapid solidification.

Investigations of the RLS process and the resulting microstructure were completely studied in detail through the use of optical microscopy, TEM and SEM. This included laser fluence effects on RLS distance, texture formation, grain size statistics and stacking fault density in Cu and Ag films.

2.1 FILM DEPOSITION

In this research, metal and SiO_2 films were deposited by sputtering at the nanofabrication facility of Carnegie Mellon University. Films consisting of a metal layer and a SiO_2 capping layer were prepared by room-temperature sputter deposition on a thermally oxidized silicon wafer where the thickness of the thermal oxide was 1 μm [**6**]. The 100 nm, 200 nm, 500 nm or 1000 nm thick metal films were deposited first on the SiO_2-coated Si substrate by DC sputtering. The purity of the Cu, Ag, Au and Cu-Nb targets were higher than 99.999% and vacuum base pressure less than 10^{-7} torr to avoid contamination during the sputtering. Then the target was changed to SiO_2 and RF magnetron sputtering was used to deposit the 580 nm SiO_2 capping layer. After deposition, samples were kept in the chamber with high vacuum for at least 10 minutes for cooling.

The quality of the films deposited by the sputtering, such as roughness, oxidation and so on, is much higher than many of the other techniques for manufacture of thin films. These are critical to guarantee the

success of RLS treated by the laser. The thick SiO_2 cap layer was used to avoid of dewetting of metal films during RLS [**3**, **7**]. Although the thickness of the metal film can be varied somewhat, 200 nm is considered an optimum for successful RLS and picked as a standard condition in this research in order to get rid of dewet or cap damage. When decreasing the thickness, the strength of the film would be decreased and therefore increase the tendency to dewet, or thermal strain during RLS would induce fractures in the film. With increasing film thickness the laser fluence needed for melting and RLS increases, which can lead to cap damage and difficulties for analysis by TEM. In this study, the sample identification was denoted by the metal material plus the film thickness, as shown in Table 1.

Table 1. Samples fabricated and used in the present research

Sample Name	Cu100	Cu200	Cu500	Cu1000	Ag100	Ag200	Au200	CuNb200
Material	Cu	Cu	Cu	Cu	Ag	Ag	Au	$Cu_{(0.95)}Nb_{(0.05)}$
Thickness	100nm	200nm	500nm	1 μm	100nm	200nm	200nm	200nm
SiO_2 cap	580nm	580nm	580nm	580nm	580nm	580nm	580nm	580nm

2.2 LASER IRRADIATION

After deposition, the samples were irradiated with a single pulse from a 248 nm (KrF) excimer laser, projected through a single-slit Cu mask with 5× demagnification. Here the mask is used to define the melting shape and dimension. A very small central area of laser beam with high quality is chosen for the uniform energy density as shown in Figure 11. Through a series of single-shot calibration experiments and curve fitting it was estimated that the resolution of this projection technique could approach 3 μm, corresponding to the sharpness of the sidewalls of the beam.

Each type of samples was treated by the laser from low energy to high energy by adjusting the filter in the machine to change the RLS conditions. It was found that if the laser fluence was too low, no melting could be detected. When the fluence was increased, a thin surface layer of the metal film began to be melted, which was identified as the partial melting (PM) threshold. At higher fluences, the metal film between the SiO_2 layers was fully changed to liquid, corresponding to the complete melting (CM) regime. The lowest observed fluence for this change was identified as the CM threshold. RLS was found to take place only in the range of fluences between the CM threshold and a higher damage threshold

corresponding to approximately 2.5~3 times the CM threshold. Above this maximum, the top SiO2 film would be broken.

In the present experiments, the laser projection system was configured to provide localized and complete melting of the metal film in a narrow line approximately 60~120 microns wide and 1 mm in length. At the termination of the pulse, the liquid cooled and RLS began, with the quenching rate assumed to be about $10^7 \sim 10^{10}$ K/s.

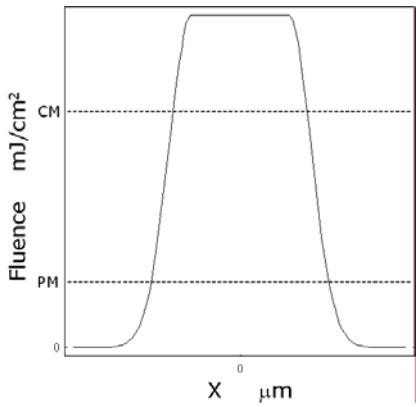

Figure 11. Schematic of the RLS profile projected on sample, where CM and PM of the RLS are detected by optical microscopy.

2.2.1 Transmission Electron Microscopy (TEM) Sample Preparation

Electron microscopy is well suited for characterization of microstructure, texture, stacking faults and other aspects of the RLS microstructure. Although the X-ray diffraction is often considered a standard method to measure the texture, the samples treated by laser could only be identified by TEM and SEM due to the small spatial scale of the RLS regions. In this work, samples were examined in a JEOL 2000FX scanning transmission electron microscope (STEM) and in a JEOL 200CX (TEM) to identify the microstructure, texture, and stacking faults formed during RLS processing. Different processes were developed to prepare the TEM samples according to the different interfacial adhesion between the SiO_2 layers and the metal films.

The interfacial force between the Cu and SiO_2 layers was found to be relatively strong. In order to prepare TEM samples of these films, an acid based back-etch technique was adapted to the metal-on-SiO_2 configuration which is shown in Figure 12. First the Cu200 samples were ultrasonically cut into a 3 mm

diameter disc, and then the Si substrate was mechanically thinned from the back to about 200 μm. It was then coated with a film of protective wax and a crater etched from the back using a concentrated mixture of HF:HNO_3 (1:3). Once the SiO_2 underlayer was reached, HF:HNO_3 (1:20) was used to widen the exposed area. After the film of wax on the samples was removed by chloroform, the samples were dipped into pure HF for 50~55 seconds to remove the 1 μm underlayer and 580 nm SiO_2 cap to expose the free-standing metal film.

Due to the weak interface adhesion force between Ag and SiO_2, the Ag200 samples were prepared by a lift-off process shown in Figure 13. First the sample was cut to a square shape about 3×3 mm^2, and then it was dipped into pure HF until the metal film was peeled off from the substrate and floated on the liquid; finally a Cu grid was applied to catch the floating metal film. Because the etching rate of the pure HF on the SiO_2 layer was measured to be about 20~24 nm/s, the sample was kept into the pure HF at least 25~30 seconds to make sure that the SiO_2 layer was gone.

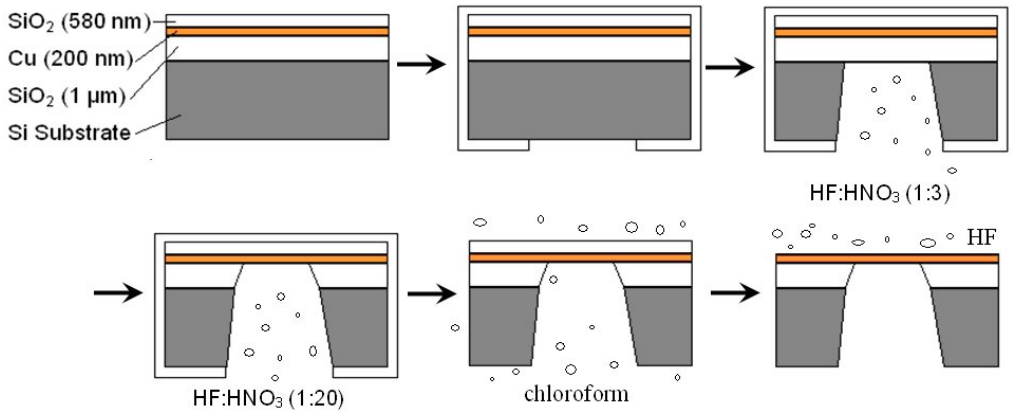

Figure 12. Process of Cu200 TEM sample preparation with an acid based back-etch technique.

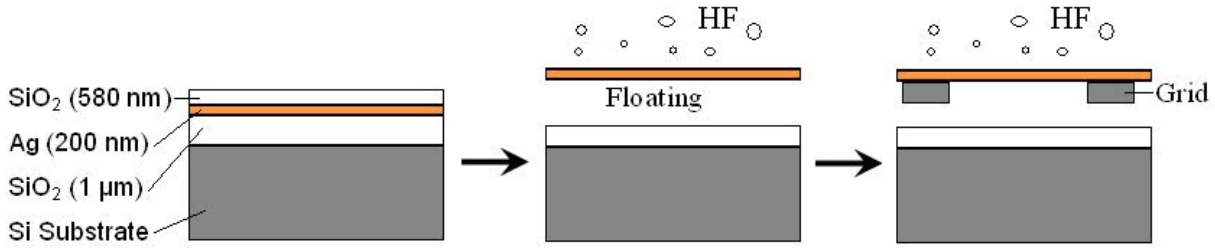

Figure 13. Process of Ag200 TEM sample preparation with a lift-off technique.

2.2.2 Scanning Electron Microscopy (SEM) Sample Preparation

It was found that SEM was an ideal technique to characterize the RLS microstructure in all of the metal films investigated. Here it was possible for the micro-texture to be quantitatively investigated using Orientation Imaging Microscopy (OIM). It provided an automated method to reveal and to study the relationship of grain orientation versus growth location in the RLS microstructure. In the present work, the texture of the RLS area treated by laser was examined in a Philips XL30 scanning electron microscope using EBSD pattern analysis.

Because the SEM electron beam cannot penetrate through the thick insulating layer of capping SiO_2, the top silica layer on the Cu and Cu-Nb films were removed by RIE (Reactive Ion Etching) at the rate of 92±2 nm/min. The adopted recipe was CHF_3=3 sccm, O_2=2 sccm, Voltage=300 Watt, and the background pressure=15 mTorr. Although the reactive time to remove the 580±60 nm silica layer was 380±50 s at the rate of 92±2 nm/min, because the Cu layer did not react with the RIE gases, the copper sample could be left in the RIE chamber for as long as 1500 s to get a very clean surface without oxide residue.

However, the silver and gold films were found to be highly reactive with all of the RIE recipes tried. For these samples, the top silica layer on the silver and gold films were removed by the pure HF solution at the rate of 22±2 nm/s. Again, although the reactive time to remove the 580±60 nm silica layer is about 22~32 s at the rate of 22±2 nm/s, the samples were put into the pure HF solution for 50 s to get a very clean surface without oxide residue.

Finally, the laser treated rapidly solidified area of the sample was examined in a Philips XL30 SEM (Scanning Electron Microscopy). OIM (Orientation Image Mapping) data was collected was collected under the EBSD (Electron Back Scattering Diffraction) mode from random selections of groups of grains in the RLS region. Each dataset represented relatively large regions spanning the entire width of the line, up to 60 or 100 μm wide, and up to 40 μm transversely along the line. This typically corresponded to more than 200 grains in each metal film was studied for the texture formation. From these data, it was possible to resolve grain orientations relative to the growth direction and the film normal direction. To ensure precise angular information, the normal direction of EBSD was calibrated by the calibrated <001> silicon, and the growth direction was calibrated by the edge line of the RLS region.

3.0 RLS CHARACTERISTICS

In our research, the absolute energy [J] of the incident laser pulse and the area of the laser pulses can be measured [**28**]. Using this information and other calibration experiments relating to the beam profile, it is possible to determine the absolute energy density, called fluence, for a single pulse incident on the sample surface.

The fluence was increased from the low energy to high energy in a series of experiments. At first, the metal film was found to be melted partially on the top part of the layer, called partial melting (PM). The fluence for the transition point to PM is called PM threshold. And then, with the further increasing energy the metal film would be melted through the whole thickness where RLS appeared, called completely melting (CM). The fluence for this transition from PM to CM is called CM threshold. Finally, the energy was too high and broke the top silica cap.

The calibrated PM, CM and the maximum fluence were determined using optical microscopy of laser processed films in Cu, Ag, Au and Cu-Nb films for different wide lines, as shown in Table 2.

Table 2. PM threshold, CM threshold and the maximum fluence found in the calibration experiments.

Metal	PM Threshold mJ/cm^2	CM Threshold mJ/cm^2	Maximum Fluence mJ/cm^2
Cu100 (60 μm line)	308	390	1008
Cu200 (60 μm line)	504	582	1270
Cu500 (120 μm line)	825	1229	3177
Cu1000 (120 μm line)	1052	1428	2973
Ag100 (60 μm line)	168	211	654
Ag200 (60 μm line)	213	279	816
Au200 (60 μm line)	282	376	896
CuNb200 (60 μm line)	302	526	1169

However, the incident laser energy cannot be totally absorbed by the metal films, some of which will be reflected. For the different metal thin films, there is difference in optical index between metals and silica top layers. In experiments involving Cu, Ag and Au, it was therefore important to normalize for this optical index. This is accomplished by using the ratio of the input energy over the CM threshold. When experimental conditions are normalized in this way, it is reasonable to assume that the temperatures of Cu, Ag and Au were approximately the same for the similar ratio of E/E_{CM}, and thus induced an initially similar quenching rate.

All of the following research is done in the CM ranges separately, and in general the E/E_{CM} ratio of 3.0, 2.3, 1.7 and 1.2 are chosen up for comparison. The 100 nm and 200 nm thick thin films were melted by the laser in an area of 1 mm long and 60 μm wide, and the 500 nm and 1 μm thick thin films were melted in an area of 1 mm long and 100 μm wide. Examples of irradiated 100 μm lines used for in this study are shown in Figure 14.

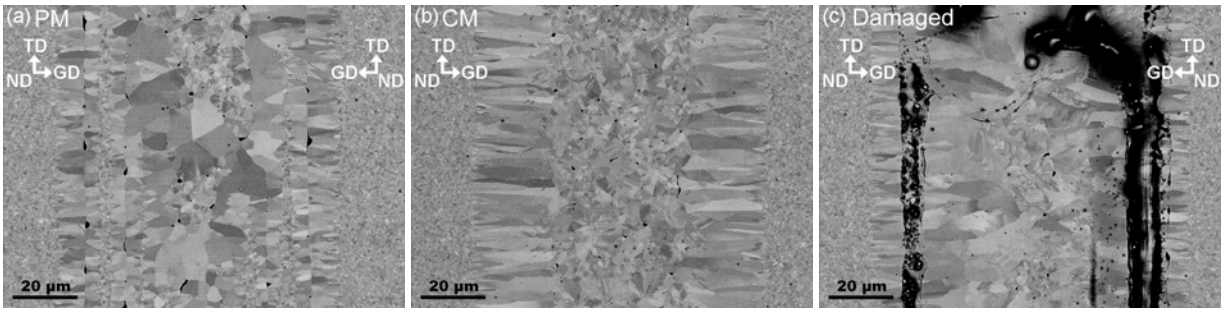

Figure 14. Microscopy images of (a) PM, (b) CM and (c) damaged film of Cu1000.

3.1 FOUR ZONE RLS MICROSTRUCTURE IDENTIFIED

A number of experiments were conducted to identify metals, it was found that some metals were able to form RLS, such as Cu, Ag and Au, while some other metals were not, such as Ni and Cr. However, Cu-Nb alloy was able to form RLS although we could not achieve RLS in the pure Ni. All of the RLS regions for Cu, Ag, Au and CU-Nb showed the similar microstructure with some individual characters. For those metals that could not form RLS in our research, the reason of no RLS might be caused by the wrong thickness, rough surface, oxidation, impurity and so on. Therefore, no conclusion can be made about why RLS can or cannot proceed in specific materials.

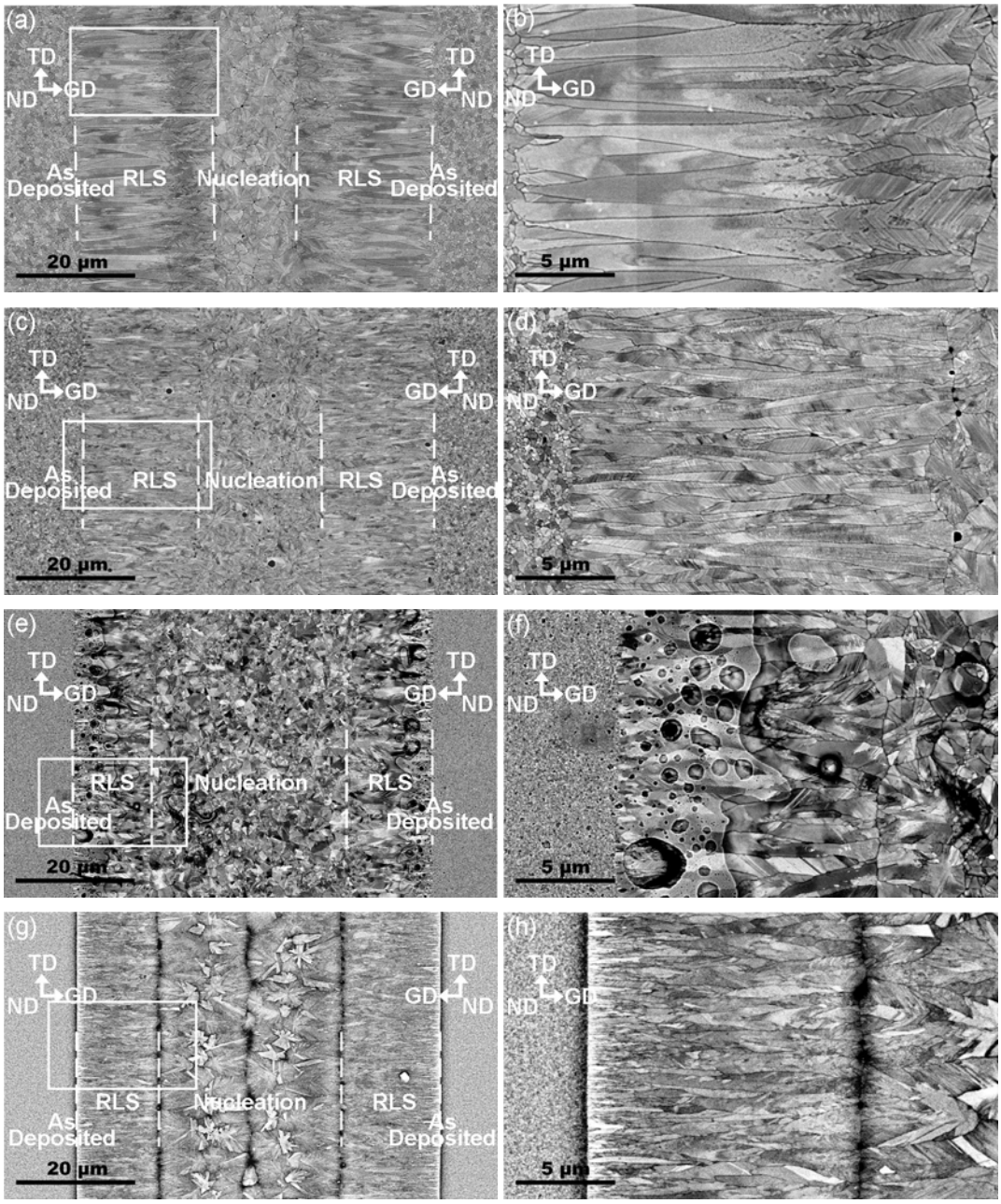

Figure 15. SEM characteristics of (a) and (b) Cu200 (E/E_{CM}=2.3), (c) and (d) Ag200 (E/E_{CM}=2.3), (e) and (f) Au200 (E/E_{CM}=2.3), (g) and (h) Cu-Nb200 (E/E_{CM}=2.3).

The SEM microstructure of the 60 μm width of RLS region formed in Cu200, Ag200, Au200 and Cu-Nb200 films are shown in Figure 15, where (b), (d), (f) and (h) show the RLS microstructure details in the small rectangles in (a), (c), (e) and (g). In all of these films, the RLS regions grow from the edge of the pool to the center and are ended by the nucleation. Although the ratio of E/E_{CM} is about 2.3 in each

film where the initial temperatures is assumed to be the same, the RLS distances and grain sizes depend on materials.

The RLS distance in the Cu200 film is the longest and the grains are the widest, with a large number of stacking faults can be found at the end of RLS (shown in Figure 15(a) and (b)). However, the grain width of the silver film is smallest and a high density of the stacking fault (SF) is uniformly everywhere (shown in Figure 15(c) and (d)). The gold thin film has severe winkles as shown in Figure 15(e) and (f), and here the RLS distance is shorter than the other materials. Shown in Figure 15(g) and (h), the Cu-Nb alloy has a similar microstructure to the pure Cu thin film, but with a shorter RLS distance and smaller grain width.

Several 60 μm wide RLS lines in Cu (690 mJ/cm^2, E/E_{CM}=1.7) and Ag (595 mJ/cm^2, E/E_{CM}=2.3) films were examined by bright field TEM in plan view. Examples of typical Cu and Ag microstructures are shown in Figure 16(a) and (b), respectively. Both Cu and Ag films consisted of elongated ribbon- or sheet-like grains in the RLS regions. Although there are similar to the columnar grains found universally in bulk metals made by casting [**29**], spinning [**6**] and other techniques [**3**,**30**], there are important differences in the RLS microstructure, geometry and the heat flow.

Investigation via TEM revealed that the RLS microstructure can in general be subdivided into four distinct microstructural regions or zones. All four zones are present in copper films, while only three zones are found in the Ag films. In addition, statistical measurements of grain width in the different zones were made that support these classifications. These zones are shown in Figure 16 (a) and (b) and are defined as follows:

I) **Occlusion (zone I).** Solidification of the irradiated metal begins in zone I when the temperature of the liquid pool decreases and reaches the melting point T_M. Solidification initiates at seeds (nucleation sites), provided by the unmelted polycrystalline grains at the edge of the melted pool. Initially the solidification velocity is slow, then proceeds faster and faster as heat is transferred perpendicularly (downward) into the Si substrate. Solidification thus proceeds as opposing fronts from both sides of the line to grow laterally toward the center of the pool. This results in columnar growth similar to casting, but without the initial chill-zone. It is found that some grains expand wider and wider in the plane of the film plane at the expense of their neighbors. As a result, many grains are occluded and disappear as solidification proceeds. It has also been found from TEM analysis that these grains expand vertically to span the full film thickness as they grow.

As the growth velocity in zone I is initially low, one must consider the possibility that occlusion may be caused by either an anisotropically interfacial energy at the L-S interface or anisotropic growth kinetics,

possibly coupled with thermally dendritic instability effects at the S-L interface. The mechanism of this selective expansion of some grains has not been well understood to date, and remains one of the major open questions in rapid solidification, as discussed below. However, in this research we have achieved some new results in the followed chapters and tried to answer the question with our best knowledge.

II) **Stable (columnar) growth.** The successful grains emerging from zone I advance forward along the growth direction (GD) toward the center and form a columnar, or long ribbon-like shape. In this zone of columnar solidification, fewer grains shrink and disappear, while most grains maintain a uniform width during growth. In some cases, grains expand and appear to divide into several narrow subgrains. Here it is possible that new grains generated during the solidification in this zone might involve defects or mechanical stress. Although the mechanism is as yet unknown, it appears that columnar growth represents a dimension balance between expansion of grain width and splintering process, with the mean width of the grains remaining stable in this stage.

Thirty-five grains in zone II of a Cu film were chosen for analysis by TEM to determine their orientation using Kikuchi patterns. This analysis showed that the texture of zone II in Cu film is <100> along the GD and <100> and <110> in the normal direction (ND) of the film. More comprehensive studies using EBSD, described later confirmed that this texture is statistically significant.

This result is consistent with the literature in which the <100> has been found to be a favored solidification growth direction in some pure FCC metals, and it is thought to be related to thermal dendrites. Due to the high heat flux by conduction from the metal film into the substrate, it is expected that the solidification of zone II into the supercooled liquid reaches a high velocity. Under these conditions, it is possible that the instability of the S-L interface decreases and therefore the thermal dendritic growth might not as important as in zone I.

III) **Defective (fan) growth.** This stage of growth has been found in the Cu and CuNi films treated by RLS but not in Ag and Au films. In this zone, the stable columnar growth of the elongated grains in zone II changes to a more unstable solidification, in which some grains widen rapidly and form a fan-like shape at the expense of their neighbors, being similar with zone I.

The orientation data taken from zone III shows that the texture along ND changes to <111>. However, there is no sharp change in microstructure (such as the appearance of new grains) that can be associated with the texture change from zone II to zone III. However, there is a much higher defect density is observed in zone III, including twins, stacking faults, dislocations and so on.

The formation of this fan growth zone in Cu may be a kinetic effect, or might instead be resulted from the segregation of oxygen in Cu because this stage happens at the end of solidification [**31**]. The

absence of fan growth zone in Ag might be due to recrystallization, which often can take place during the cooling process [**3**]. Zone III is a much more complicated region than zones I and II, requiring much more extensive experimentation and analysis to understand the mechanisms.

IV) **Nucleation.** This region is found in the middle of the irradiated region, and characterized by an equiaxed polycrystalline microstructure, with radial subgrain structures extending from single points inside each grain. This is attributed to a spontaneous nucleation process occurring in the center of the supercooled liquid pool which in general starts from the interface of the liquid metal and the silica cap layer. Growth of grains extends outward and meets with zone III in a wavy line and stops RLS.

All of the samples, such as Cu100 (Figure 17), Cu200 (Figure 18), Cu500 (Figure 19), Cu1000 (Figure 20), Ag100 (Figure 21), Ag200 (Figure 22), Au200 (Figure 23), Cu-Nb200 (Figure 24), treated with the different laser energy (E/E_{CM}=1.2, 1.7, 2.3 and 3.0) were studied in SEM, and zone I, II, III and IV determined by visual observation were defined above.

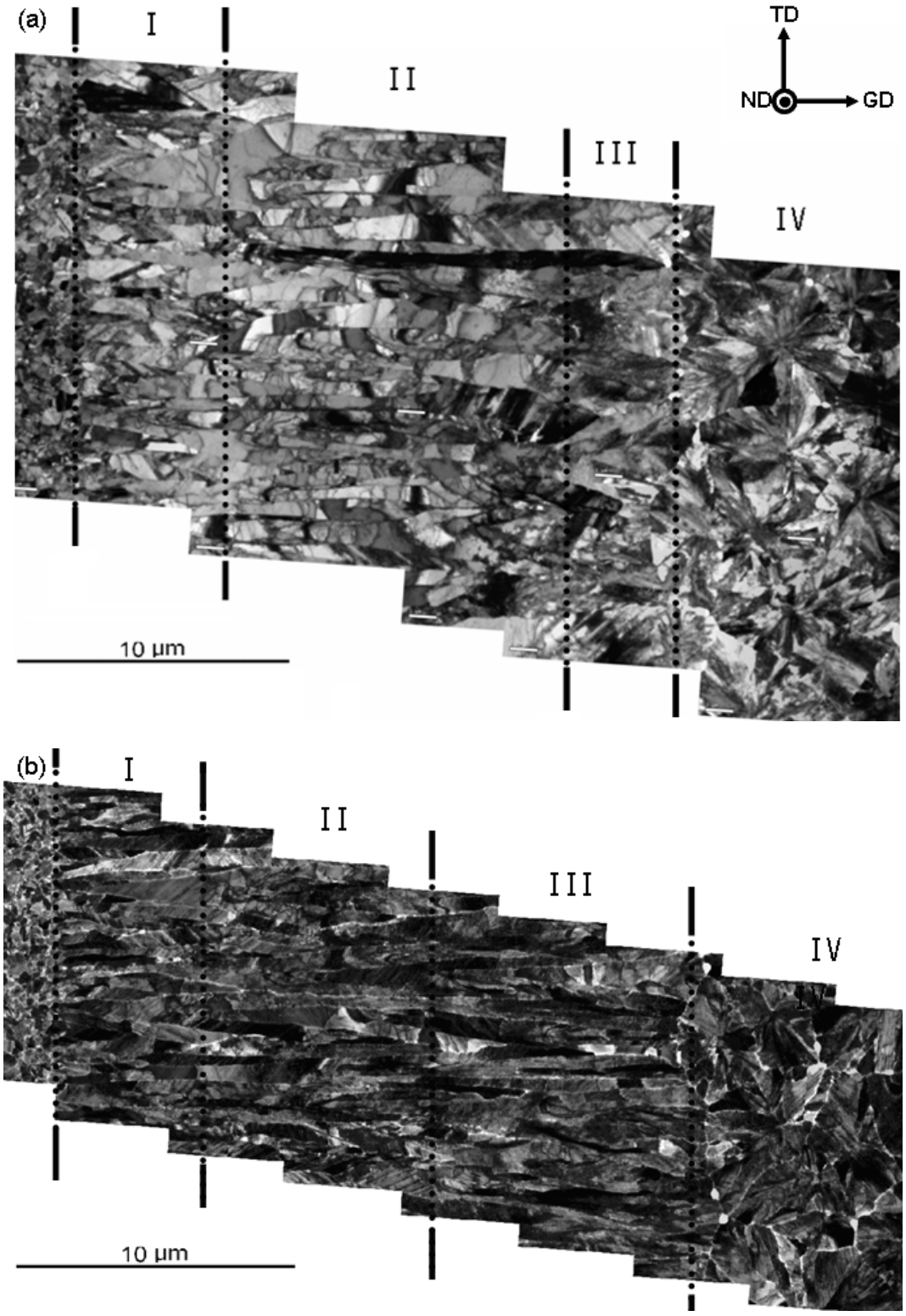

Figure 16. TEM characteristics of (a) Cu (E/E_{CM}=1.6), and (b) Ag (E/E_{CM}=2.3). Each of them shows four zones in the cross section: (I) occlusion zone, (II) columnar growth zone, (III) fan growth zone and (IV) nucleation zone.

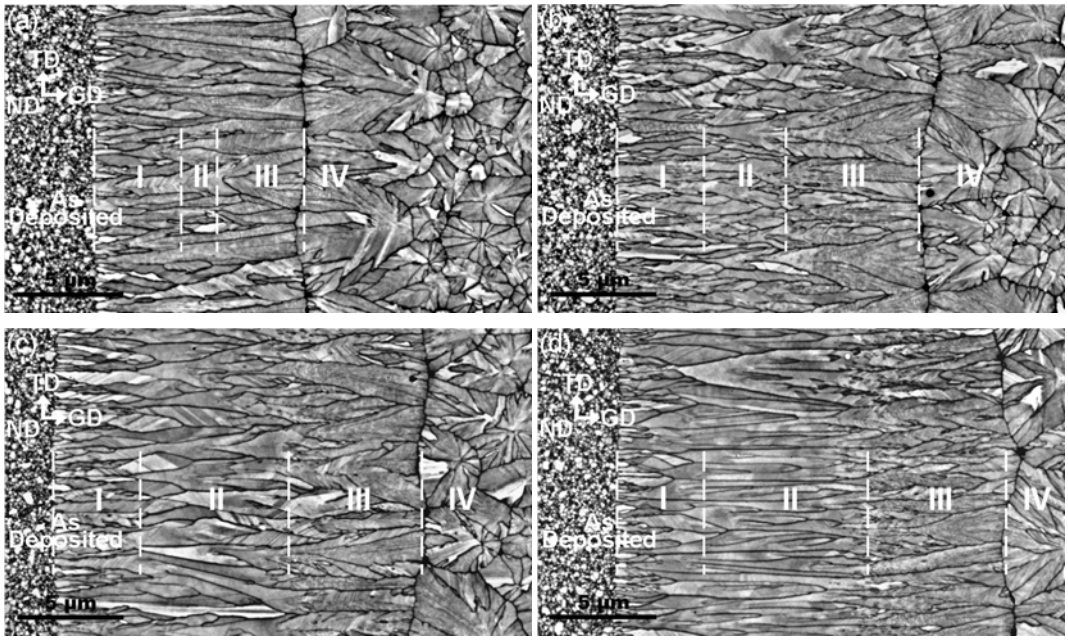

Figure 17. SEM microstructure of Zone I, zone II, zone III and zone IV in Cu100: (a) E/E_{CM}=1.2, (b) E/E_{CM}=1.7, (c) E/E_{CM}=2.3 and (d) E/E_{CM}=3.0.

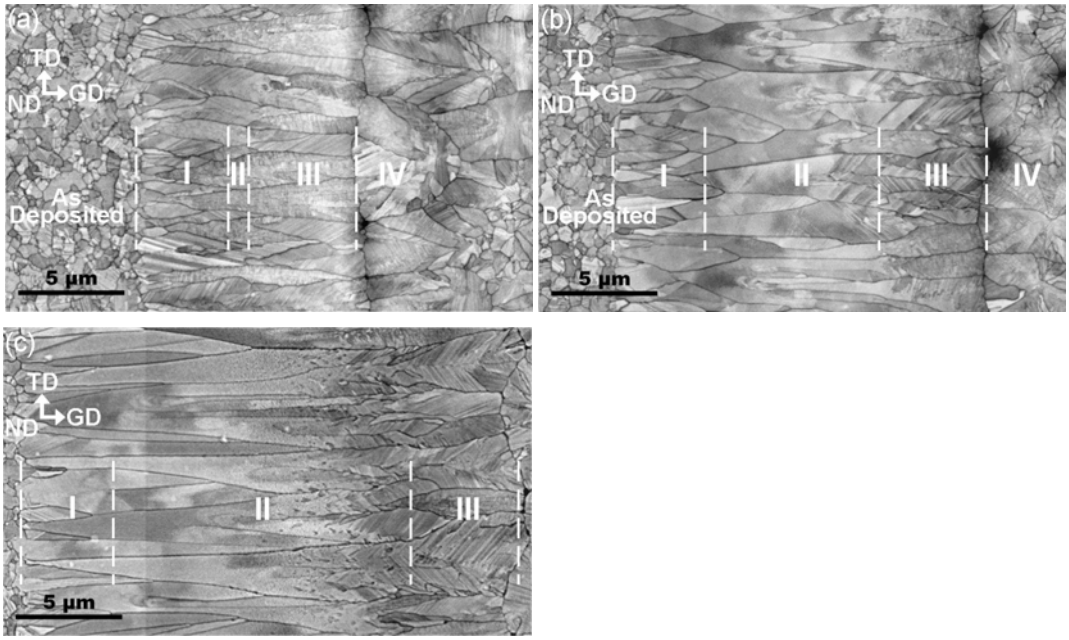

Figure 18. SEM microstructure of Zone I, zone II, zone III and zone IV in Cu200: (a) E/E_{CM}=1.2, (b) E/E_{CM}=1.7and (c) E/E_{CM}=2.3.

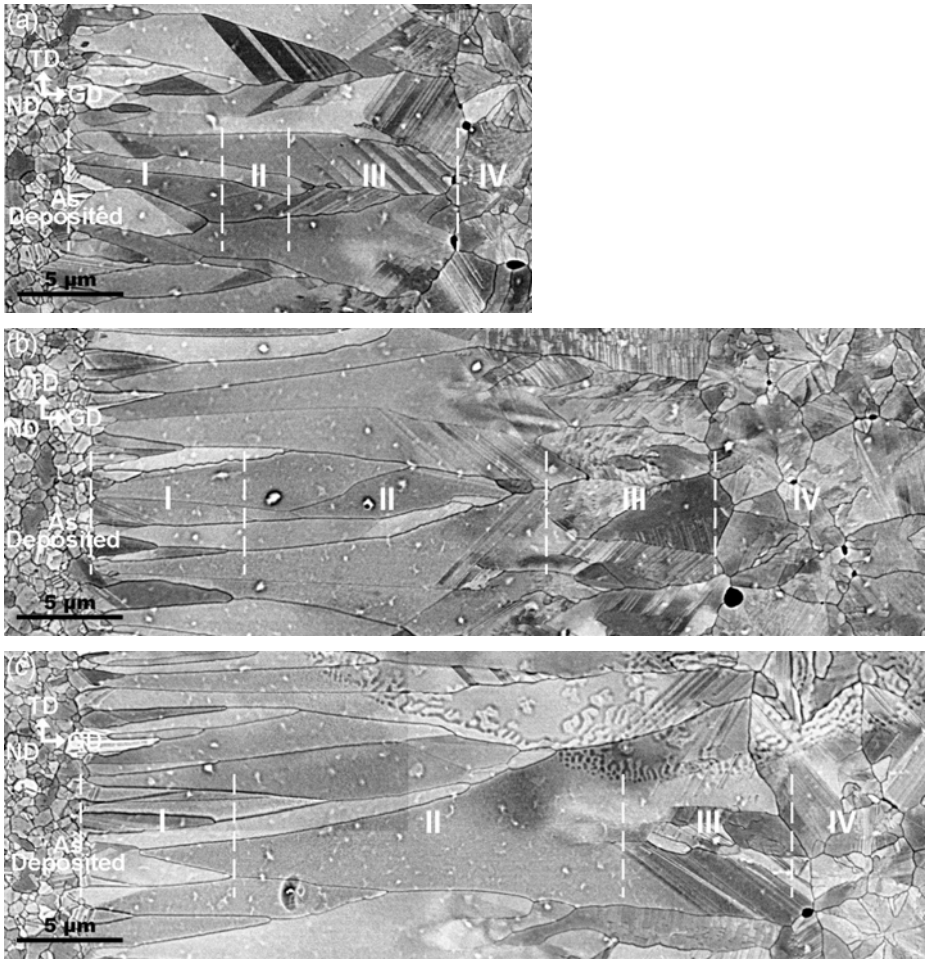

Figure 19. SEM microstructure of Zone I, zone II, zone III and zone IV in Cu500: (a) E/E_{CM}=1.2, (b) E/E_{CM}=1.7and (c) E/E_{CM}=2.3.

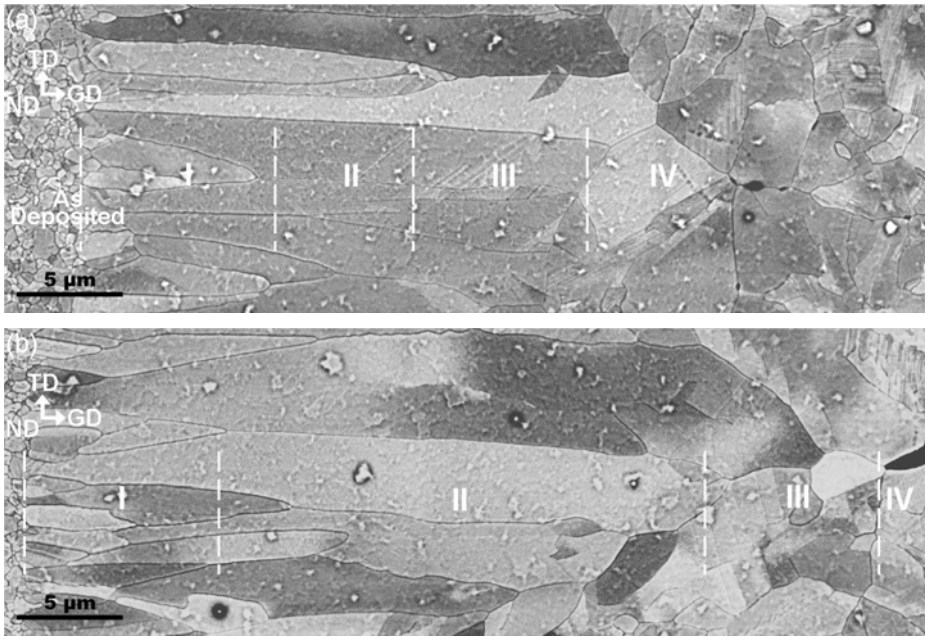

Figure 20. SEM microstructure of Zone I, zone II, zone III and zone IV in Cu1000: (a) E/E_{CM}=1.2 and (b) E/E_{CM}=1.7.

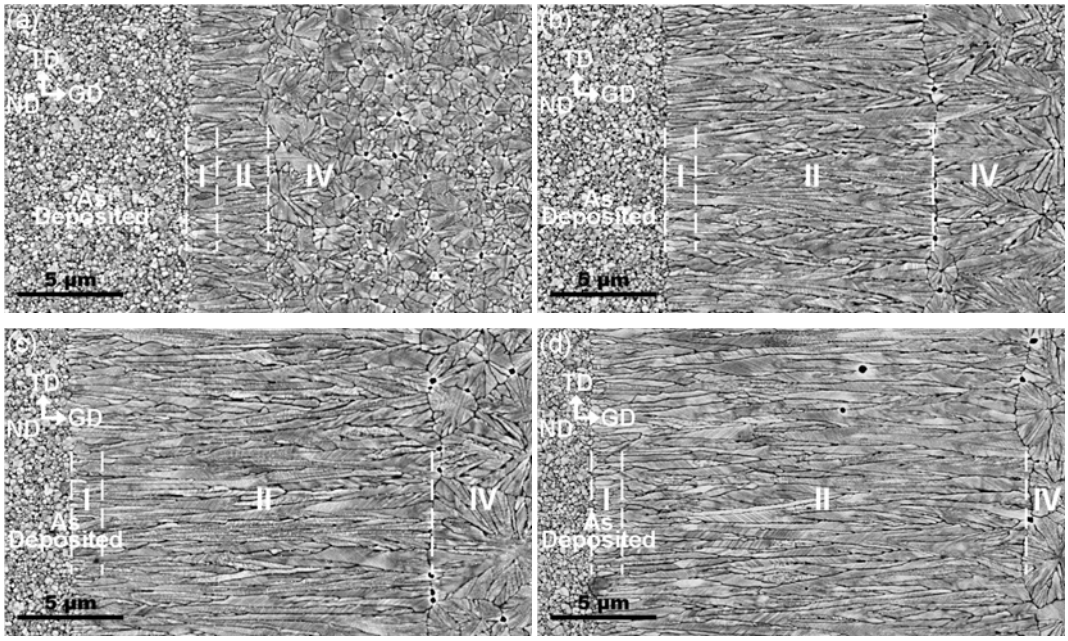

Figure 21. SEM microstructure of Zone I, zone II, zone III and zone IV in Ag100: (a) E/E_{CM}=1.2, (b) E/E_{CM}=1.7, (c) E/E_{CM}=2.3 and (d) E/E_{CM}=3.0.

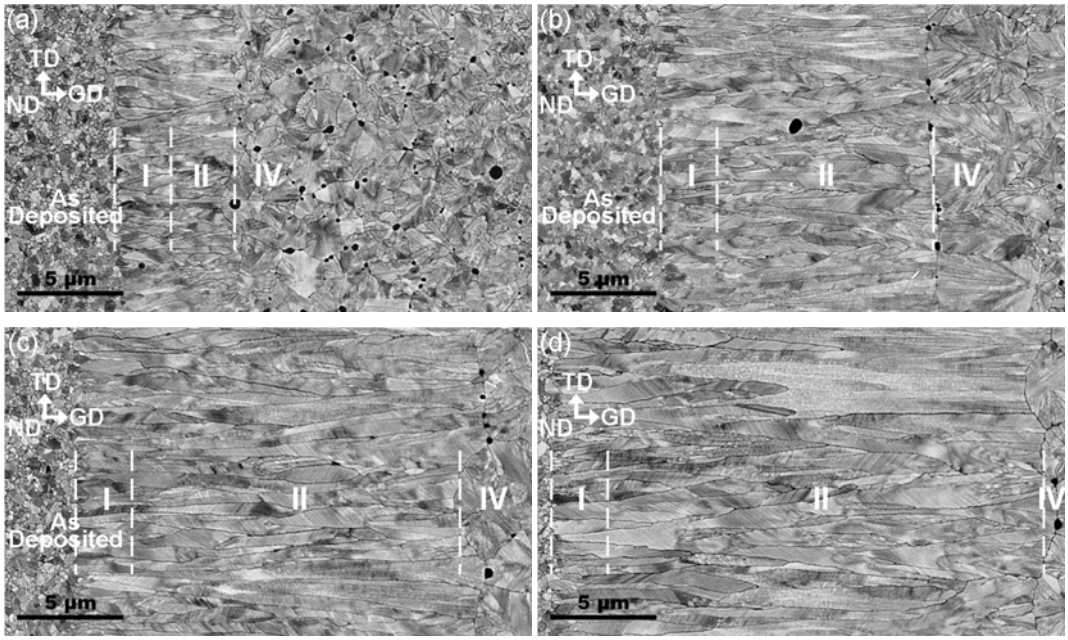

Figure 22. SEM microstructure of Zone I, zone II, zone III and zone IV in Ag200: (a) E/E_{CM}=1.2, (b) E/E_{CM}=1.7, (c) E/E_{CM}=2.3 and (d) E/E_{CM}=3.0.

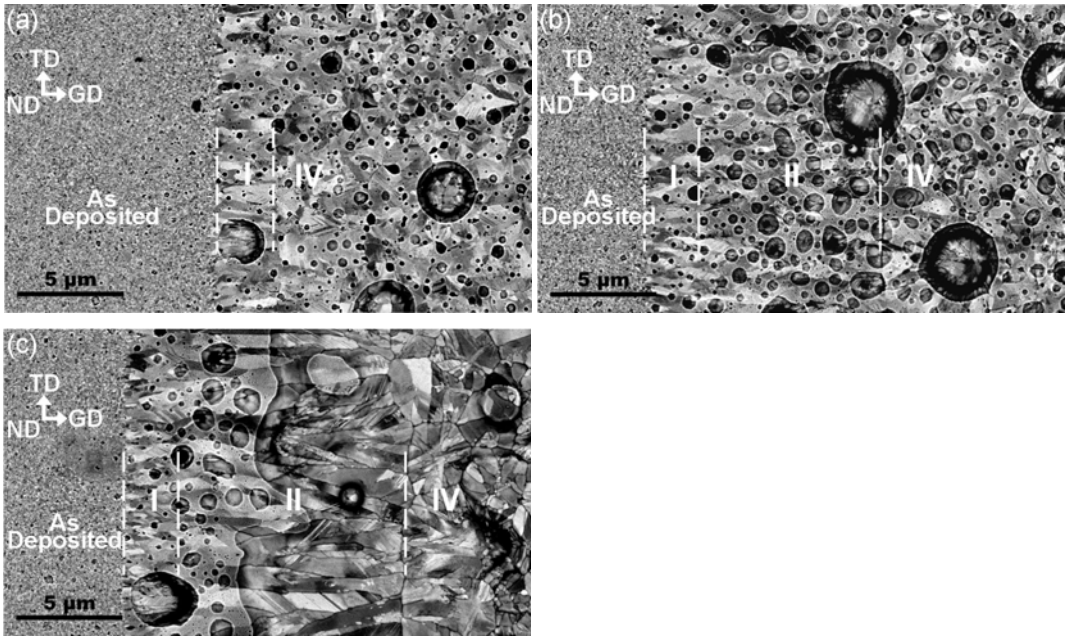

Figure 23. SEM microstructure of Zone I, zone II, zone III and zone IV in Au200: (a) E/E_{CM}=1.2, (b) E/E_{CM}=1.7and (c) E/E_{CM}=2.3.

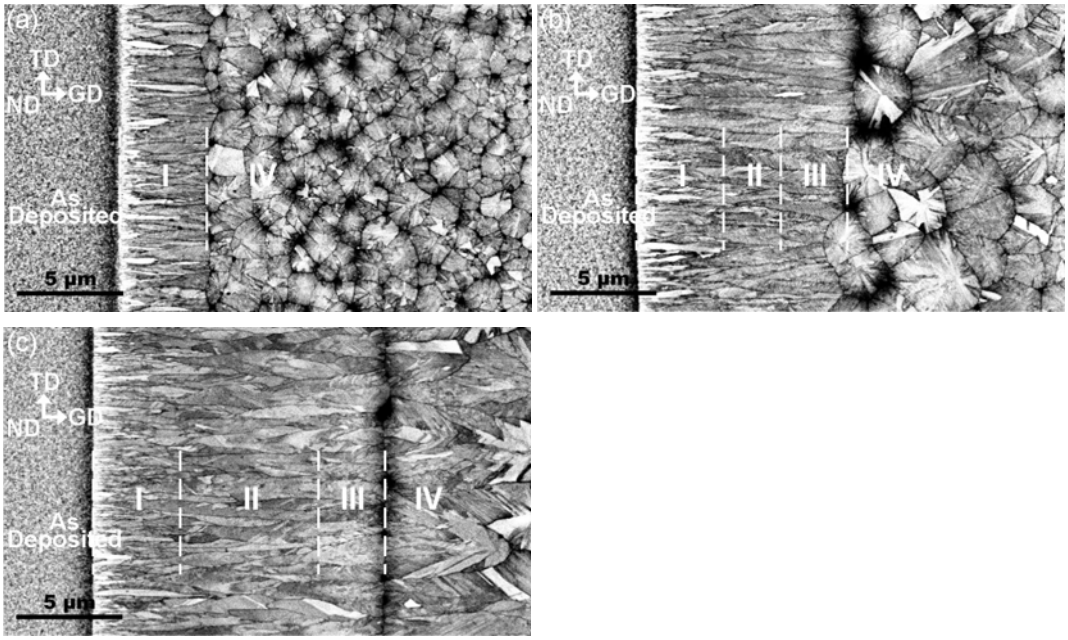

Figure 24. SEM microstructure of Zone I, zone II, zone III and zone IV in Cu-Nb200: (a) E/E_{CM}=1.2, (b) E/E_{CM}=1.7and (c) E/E_{CM}=2.3.

3.2 STATISTICAL MEASUREMENT TECHNIQUES USED TO DEFINE RLS ZONES

In zone I the mean width of individual grains increases significantly as most grains disappear, and a small number of successful grains grow wider. In zone II, new grains are generated at a rate similar to the rate of disappearance, so that the mean width remains relatively stable. Finally in zone III (for Cu and Au), some grains expand rapidly and exhibit a fan shape at the expense and disappearance of the other grains. In order to quantitatively describe these transitions, 16 random areas of RLS with a dimension of 25 μm × 19 μm are chosen for the statistical measurement to characterizing the different stages of RLS. Due to the special geometry of the RLS microstructure, the mean width of the grains is used to describe the different RLS stages.

Shown in Figure 25, the mean width of the Cu200 grains at the different distance into the RLS determined (called RLS distance) are determined, and then the RLS areas are divided into zone I, zone II and zone III by the inflection points of the curves. For the Cu200 sample treated with the low laser energy (E/E_{CM}=1.2), the total RLS distance is about 10 μm and zone I is 5 μm wide, zone III is 4 μm wide and zone II is almost absent under the given conditions. For the RLS area treated with the medium laser energy (E/E_{CM}=1.7), the total RLS distance is about 17 μm and the width of zone I is 6 μm, zone II is 8μm and zone III is 3 μm. For the sample treated with the high laser energy (E/E_{CM}=2.3), the total RLS distance is about 22 μm and the width of zone I is 4 μm, zone II is 13μm and zone III is 5 μm.

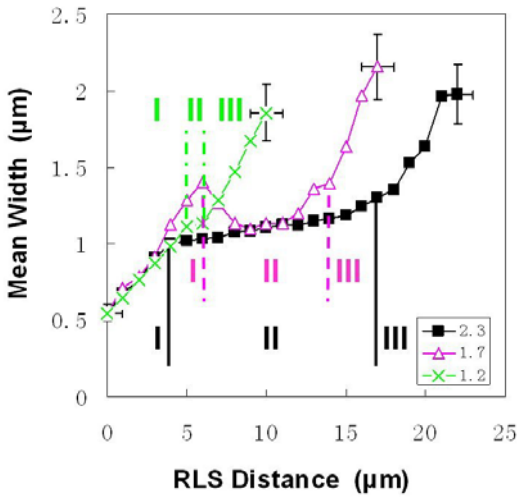

Figure 25. The mean width of Cu200 grains changes at the different RLS distance, where the zone I, zone II and zone III are divided by the inflection points of the curves. The curves represent the different laser energy conditions, i.e. E/E_{CM}=1.2, 1.7 and 2.3.

In conclusion, both zones I and III are always about 5 μm , and zone II increases with the increasing laser fluence. In zone I the mean width of the grains increases rapidly from 0.5 μm to 1 μm, in zone II the mean width is stable at about 1.15 μm, and in zone III the mean width increases rapidly again from about 1.3 μm to about 2 μm.

All of the given data are summarized with other films together in Table 3.

Table 3. The growth length and mean width of zone I, II and III in different materials with the changing energy ratio and the film thickness.

Metal	E/E_{CM}	RLS Distance	Zone I		Zone II		Zone III	
			Length	Mean Width	Length	Mean Width	Length	Mean Width
		(μm)	(μm)	(μm)	(μm)	(μm)	(μm)	(μm)
Cu200	1.2	10	5	0.82	1	1.12	4	1.48
	1.7	17	6	0.97	8	1.24	3	1.79
	2.3	22	4	0.78	13	1.12	5	1.63
Cu100	1.7	13	4	0.33	6	0.57	3	0.83
Cu200		17	6	0.97	8	1.24	3	1.79
Cu500		28	16	1.74	9	3.09	3	3.58
Cu1000		40	13	1.61	18	4.21	9	7.56
Cu200	2.3	22	4	0.78	13	1.12	5	1.63
Ag200		19	4	0.42	15	0.63	/	/
Au200		12	4	0.51	8	0.82	/	/

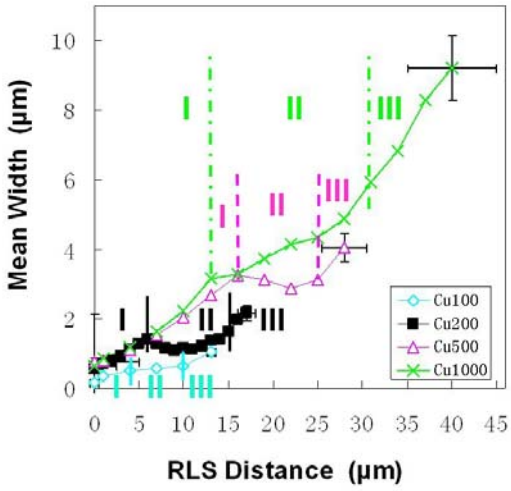

Figure 26. The mean width of Cu100, Cu200, Cu500, Cu1000 grains change at the different RLS distance, where the zone I, zone II and zone III are divided by the inflection points of the curves. The curves represented the RLS region which was treated by the laser energy of E/E_{CM}=1.7.

The Cu100, Cu200, Cu500 and Cu1000 samples are treated by the energy with a ratio of E/E_{CM}=1.7, then the mean width of the grains is measured at the different RLS distance (Figure 26). Shown in Figure 26, the same method is used to find out the zone I, zone II and zone III, i.e. the zones are divided by the inflection points of the curves.

For the copper films of different thickness, both of the total RLS regions and the mean width of the grains increase with the increasing thickness. The mean width of zone II in Cu100 is about 0.57 μm, in Cu200 is about 1.24 μm, in Cu500 is about 3.09 μm, and in Cu1000 is about 4.21 μm.

Different metal films with the same thickness were also processed under similar laser energy conditions and studied with the same method as shown in Figure 27. The Cu200, Ag200 and Au200, which were treated by the laser energy of E/E_{CM}=2.3, and zone I, II and III determined by the inflection points of the curves. The division of zones in Cu200 is very clear due to the sharp change of the mean width of the grains, while zone III is absent in both of Ag200 and Au200.

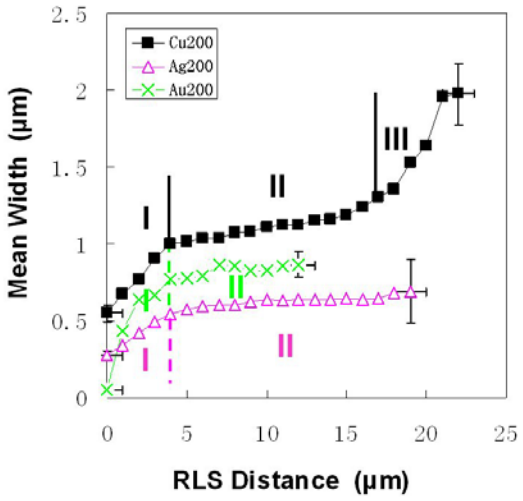

Figure 27. The mean width of Cu200, Ag200, Au200 grains changes at the different RLS distance, where the zone I, zone II and zone III are divided by the inflection points of the curves. The curves represent the RLS region which is treated by the laser energy of E/E_{CM}= 2.3.

In Cu200 the total RLS length is about 22 μm, where zone I is about 4 μm, zone II is 13 μm and zone III is about 5 μm. In Ag200 the total RLS length is about 19 μm, where zone I is about 4 μm and zone II is 15 μm. In Au200 the total RLS region is 12 μm, zone I is about 4μm and zone II is 8μm. It is obvious that the length of zone I is the same in these three metal films, but the length of zone II depends on the

material. In addition, in Cu200 the mean width of zone II is about 1.12 μm, in Ag200 the mean width is about 0.63 μm, in Au200 the mean width is about 0.82 μm.

In summary, several trends can be observed in this data:

1. Zone III is found in Cu films but not Ag or Au films, which suggests that zone III is formed due to an impurity or oxidation.
2. With the same film thickness and the energy ratio, zone I of Cu, Ag and Au has approximately the same growth distance, while zone II length (Au<Cu<Ag) and the mean grain width (Ag<Au<Cu) are dependent on the metal.
3. With the same thickness and material, zone II of Cu film increases with the increasing laser energy, while zone I and III are independent of the energy. Meanwhile, no evidence shows that the mean width is affected by the increasing laser energy.
4. With the same material and energy ratio, the growth length of zone I and II increases with the increasing film thickness (100 nm to 500 nm), and so does the mean grain size. However, the length of zone III is independent with the thickness.
5. A splintering or subgrain initiation process appears to be associated with a stable zone II during RLS. It is likely that stress decreases with the increasing film thickness, thereby suppressing the splintering process. When the thickness reached 1000 nm in the copper film, the splintering process is almost absent, along with the stable zone II.

These statistical methods we have developed are found to be useful for delineating and quantifying the microstructure structures throughout the entire RLS process. Although this data is collected after solidification, it is believed that grain boundary motion and/or coarsening is minimal, so that these represent structures formed during solidification.

3.3 ENERGY EFFECT ON LATERAL GROWTH DISTANCE

The energy absorbed by metal films is a very important parameter that determines the maximum temperature of the liquid pool and therefore affects the quenching rate of RLS. Adding more laser energy increases the temperature slowing down the quenching rate of RLS, and allows more time for nucleation (which ends RLS). As a result, the maximized lateral growth distance of RLS is increased.

Most thermophysical properties of Ag and Cu are similar, as shown in Table 4 [**32-34**]. The effect of the laser fluence on the maximized RLS distance of Cu and Al was analyzed separately as shown in Figure 28, where the film thickness is changed from 100 nm to 1000 nm. When the fluence of the laser pulse is increased from the CM threshold to the maximum, the RLS distance is found to increase rapidly and linearly at low energy, then increase more slowly at higher energy. It is obvious here that the maximized RLS distances of Cu and Ag films show a similar relationship but over a different input energy range, which is caused by the different reflective coefficients of the Cu and Ag surface. And the maximized RLS distance of metal films with different thickness show a similar relation too, where the different input energy range is caused by the different energy requirement for melting the different metal volume.

However, the maximized RLS distance is much longer in thicker films than that in the thinner ones at the same energy ratio. Considering the lower quenching rate in the thicker films which allows more time for RLS process, it is reasonable that the maximized RLS distance can reach almost 47.5 μm in Cu1000 but only 22.0 μm in Cu200. And it is obvious in both of Ag and Cu that the thinner film can reach a higher energy ratio due to the lower volume change which will break up the top SiO_2 layer.

Shown in Figure 29, the relationship between the laser energy and the RLS distance is studied in different materials with the same film thickness. The thickness in (a) and (b) is set up to 200 nm (the standard condition), and (c) and (d) is set up to 100 nm. All of the metal films follow the similar principle but again the RLS is in a different energy range due to the different energy requirement shown in (a) and (c).

Table 4. Relevant thermophysical properties of pure Cu and Ag. [32-34]

Property	Cu	Ag
Melting temperature T_M [K]	1356	1234
Density at 293 K [g/cm^3]	8.93	10.5
Latent heat [J/mol]	12970	11090
Heat capacity solid [J/mol]	$30.29 + 10.71 \times 10^{-3}T$	$21.3 + 8.54 \times 10^{-3}T$
Heat capacity liquid [J/mol]	31.4	30.5
Thermal conductivity solid [W/(m K)]	385	406
Index of refraction [n + ik] (248nm)	1.47+1.78i	1.30+1.35i

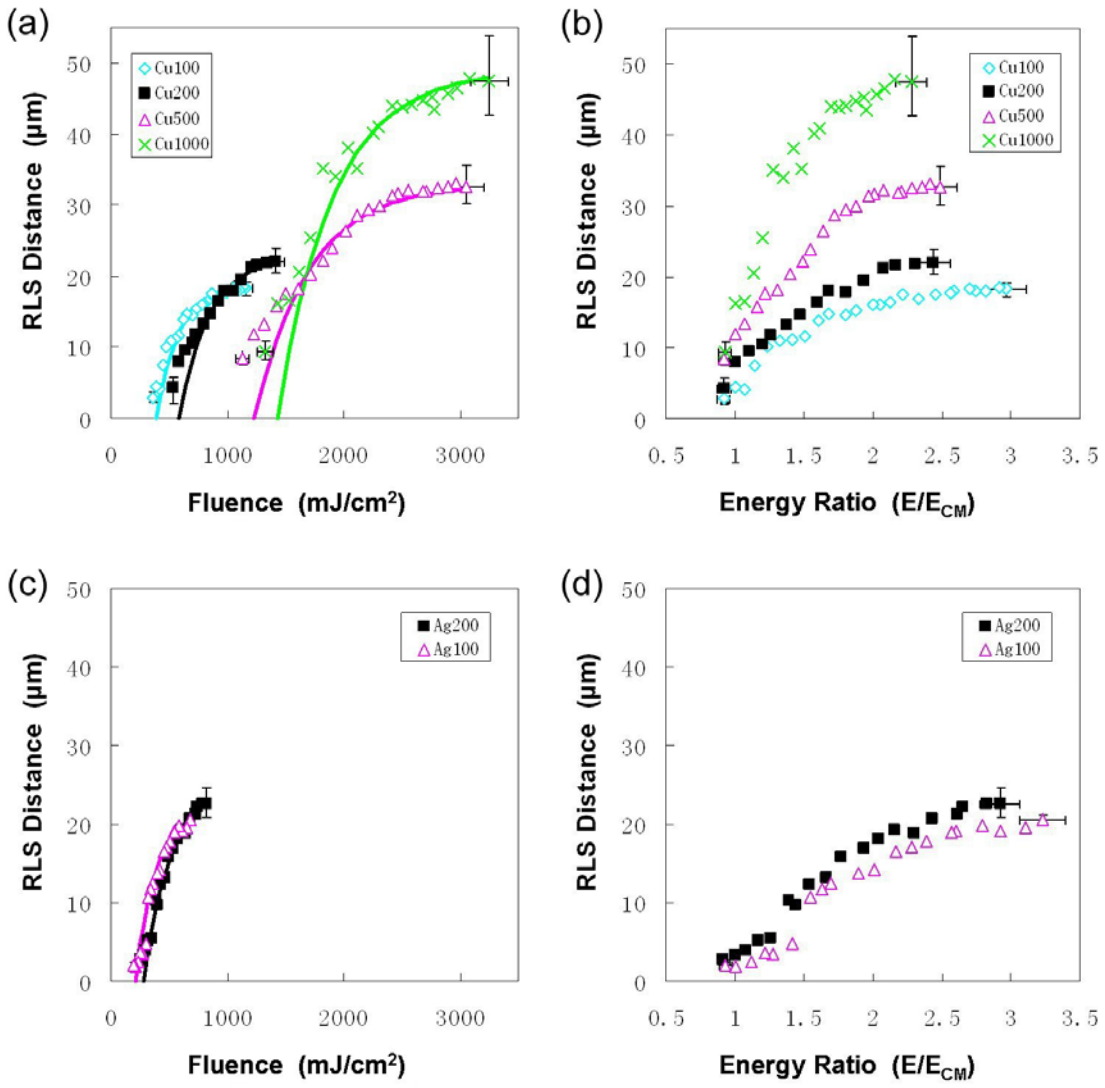

Figure 28. The maximized RLS distance of copper and silver films changes at the different fluence or energy ratio, where the film thickness is varied in each graph: (a) and (b) Cu100, Cu200, Cu500 and Cu1000, (c) and (d) Ag100 and Ag200.

The normalized input fluence relative to the CM threshold versus RLS distance is shown in Figure 29(b) and (d). As the melting temperatures of Cu and Ag are similar it is likely that the thermal history is likewise similar, and it can be seen that the measured RLS distances are very close in both 100 nm and 200 nm thickness. Also, Au200 and Cu-Nb200 are very close to each other in (b), and the maximized RLS distances are much shorter than Cu200 and Ag200. Here the shorter RLS distance of Au200 may be caused by the metal properties, while the RLS in Cu-Nb200 may be stopped by the earlier nucleation than Cu200 samples due to the presence of the Nb.

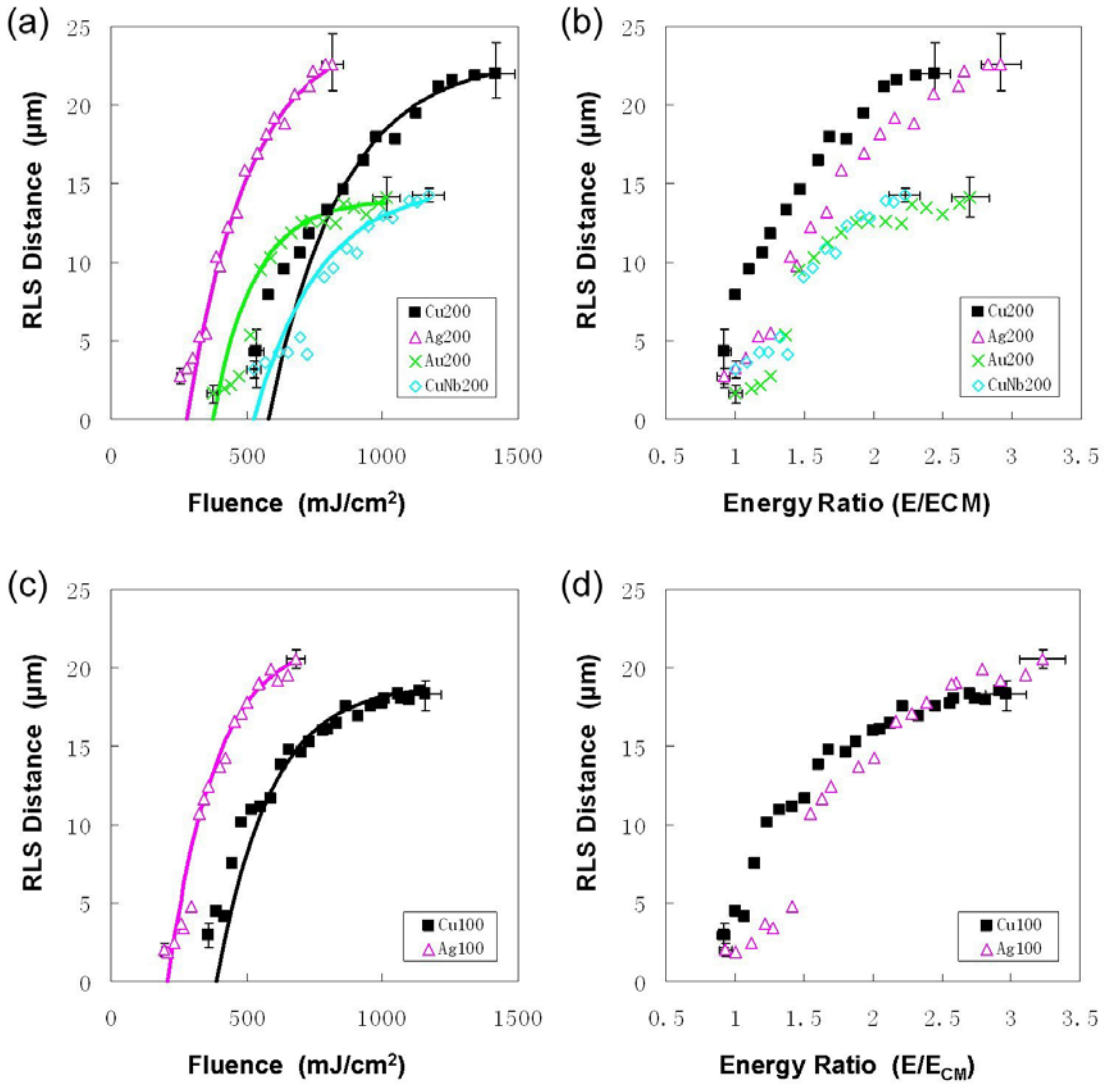

Figure 29. The maximized RLS distance of metal films changes at the different fluence or energy ratio, where the film thickness is fixed in each graph: (a) and (b) Cu200, Ag200, Au200 and Cu-Nb200, (c) and (d) Cu100 and Ag100.

The experimental data in Figure 28 and Figure 29 are fit well by the functions.

$$\chi \approx \chi_{\max}\{1-\exp[-\alpha(E-E_{CM})]\} \qquad \textbf{Equation 2}$$

$$\chi \approx \chi_{\max}\{1-\exp[-\beta(\frac{E}{E_{CM}}-1)]\}, \qquad \alpha=\frac{\beta}{E_{CM}} \qquad \textbf{Equation 3}$$

where χ_{max} is the maximum distance (μm) of the rapid lateral solidification at the condition of the infinite energy, α and β are the coefficient relatively to the changes of the quenching rate and the nucleation

temperature, E_{CM} is the absorbed energy at the complete melting threshold. All of the parameters are listed in the Table 5. Here E_{CM} is experimental determined, and the best fit parameters for the model for the metals are shown by the solid lines in Figure 28 and Figure 29.

Table 5. The parameters are experimentally determined for Equation 2 and 3.

Metal	E_{CM} (mJ/cm^2)	x_{max} (μm)	α (cm^2/mJ)	β
Cu100	390	19	0.00513	2.0
Cu200	582	23	0.00378	2.2
Cu500	1229	33	0.00212	2.6
Cu1000	1428	49	0.00210	3.0
Ag100	211	22	0.00569	1.2
Ag200	279	25	0.00430	1.2
Au200	376	14	0.00665	2.5
CuNb200	526	15	0.00418	2.2

From the discussion above, RLS is stopped when nucleation appears. As the input fluence increases, more thermal energy is put into the metal film, resulting in a slower effective quench rate. Therefore, the time required for the liquid temperature to reach the critical nucleation temperature is longer. Thus, the RLS proceeds further into the center of the pool. As a result, the RLS distance increases with the increasing energy. From the data provided, it can be concluded that the maximized RLS distances of Cu and Ag are similar given the same temperature history, which suggests there are similar kinetics governing the solidification processes of Ag and Cu.

Several conclusions can be made from the provided graphs and tables:

1. The maximized RLS distance increases with the increasing laser energy ratio and follows the function of $\chi \approx \chi_{\max}\{1-\exp[-\alpha(E-E_{CM})]\}$.
2. The maximized RLS distance increases with the increasing metal thickness at the same laser energy ratio.
3. Cu and Ag films appear to have similar kinetics in the maximized RLS process, while Au films may be different.
4. Cu-Nb has a shorter maximized RLS distance than Cu at the same laser energy ratio, suggesting that the alloying affects the formation of zone IV microstructure via nucleation.

3.4 EFFECT OF CLEANING PROCESS FOR THE COPPER FILM

The cleaning process before sputtering is very important for achieving the good RLS, especially for the copper film. In general, the silver and gold films are easy to prepare and process in RLS due to their low reactivity. The interface force between the metal films and the silica underlayer generally decreases with the oxygen activity. So although this decreased interface force may be favorable for producing the RLS microstructure, the poor adhesion may introduce problems in the etching and sample preparation. We have also found that additional impurities in the copper film strongly affect the solidification by attracting more dislocations, nucleation and so on, and can be the reason of the disappearance of RLS. Copper films exhibit a large zone III (fan zone) region, but this is absent in the silver and gold film, suggesting its formation is due to impurities.

In order to investigate the importance of the purity in RLS, the substrate (silicon substrate plus a silica layer) was cleaned with several different techniques. In the Cu200 and Cu1000 cleaning process, the substrate was washed by acetone, isopropyl and DI water, and then dipped into the HF solution ($HF:H_2O$ = 1:10) for 10 sec, finally rinsed with DI water for 5 min. In the Cu200-2 and Cu1000-2 cleaning process, the substrate was first dipped into the HF solution ($HF:H_2O$=1:10) for 10 sec, and then rinsed with DI water for 5 min, finally washed by acetone, isopropyl and DI water. The two processes are listed in Table 6.

Both substrates were put into the sputtering chamber immediately after the cleaning process. This was followed by using the same sputtering process, laser process and SEM sample preparation techniques detailed in Chapter 2.0.

The Cu200 (E/E_{CM}=2.3) and Cu1000 (E/E_{CM}=1.2 and 1.7) samples were able to achieve RLS in the laser treatment area as the previous discussion, while the Cu200-2 and Cu1000-2 samples show a totally different microstructure.

Table 6. The cleaning process for Cu100, Cu100-2, Cu1000 and Cu1000-2.

Sample	1st Step	2nd Step	3rd Step
Cu200 Cu1000	Acetone, isopropyl and DI water	HF solution ($HF:H_2O$ = 1:10) for 10 sec	DI water for 5 min
Cu200-2 Cu1000-2	HF solution ($HF:H_2O$ = 1:10) for 10 sec	Acetone, isopropyl and DI water	

The microstructure of Cu200-2 treated by the laser energy ratio of 2.3 is shown in Figure 30. Here the solidified microstructure consists of very fine grains which are much smaller than the as-deposited grains (shown in Figure 30(c) and (d)). However, the grains in zone III and IV are much larger and similar with Cu200. Cu200 treated by the different laser energy ratios showed the similar characteristics as described previously, and therefore will be not discussed here.

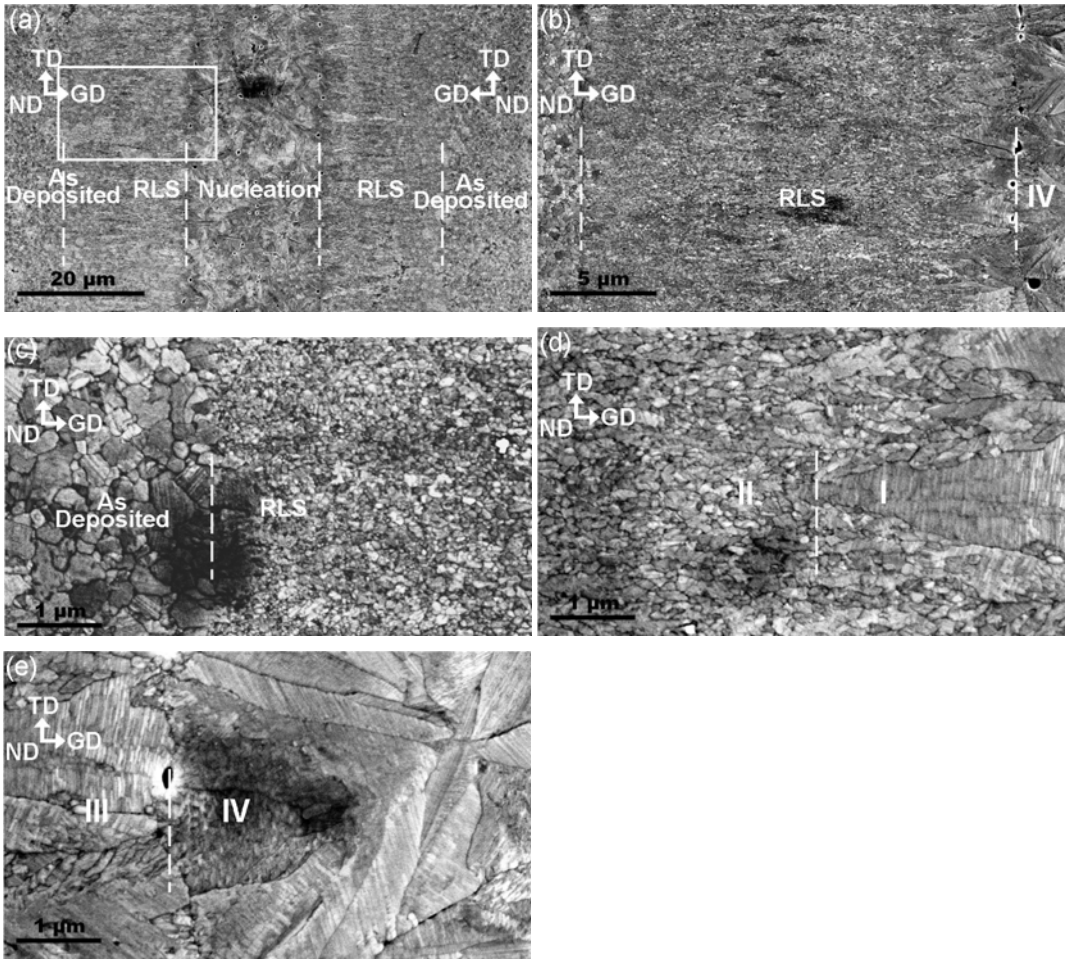

Figure 30. SEM microstructure of laser treated region in Cu200-2 (E/E_{CM}=2.3).

Shown in Figure 31, the Cu1000-2 treated by the energy ratio of 1.2 has similar structure with Cu200-2, where again very fine grains form in the laser treated region. But the zone III and zone IV are different with Cu200, where very fine grains are found as shown in Figure 31(c).

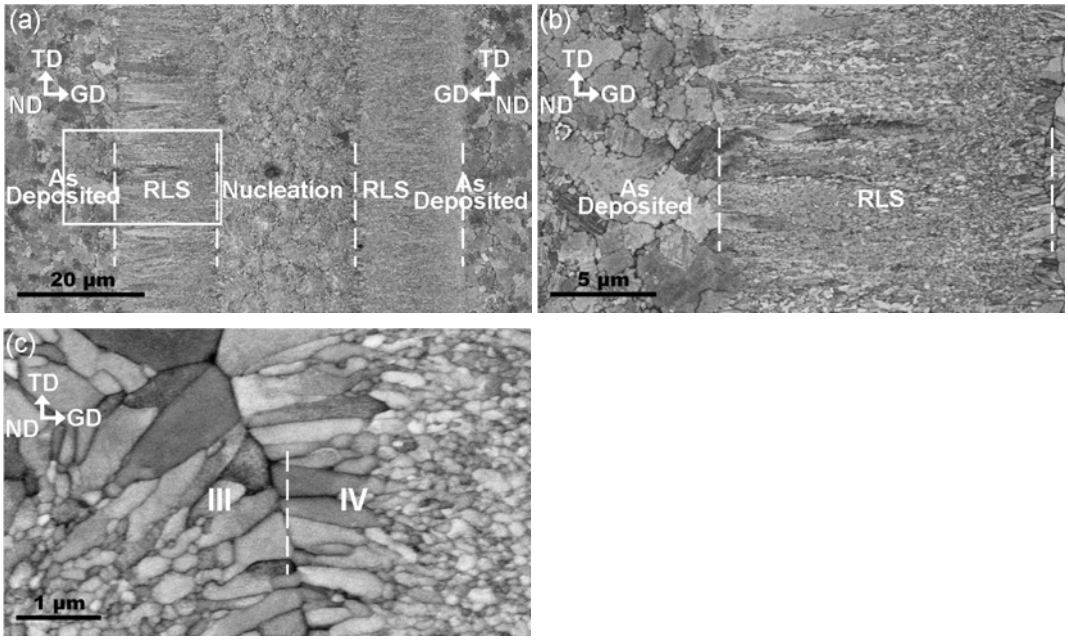

Figure 31. SEM microstructure of laser treated region in Cu1000-2 (E/E_{CM}=1.2).

But the microstructure of Cu1000-2 treated by the energy ratio of 1.7 is changed as shown in Figure 32, where zone I and zone II has the similar RLS characters with Cu1000 as shown in Figure 32(c), (d) and (e), and then fine grains forms at the end of RLS and the nucleation zone, i.e. zone III and zone IV.

This fine structure is similar to that seen in copper refinement [18], and is believed to be caused by minor impurities. The previous studies [18] found the grain refinement in the bulk copper with a very high the supercooling temperature. In this study, large grains form in at the beginning of the Cu1000-1 which has the lowest quenching rate, and very fine grains are found at the end of RLS of Cu1000-2 (E/E_{CM}=1.7) with reasonably high supercooling temperature, and also found in the samples with a much higher quenching rate, such as Cu1000-2 (E/E_{CM}=1.2) and Cu200 ($E/E_{CM}\leq$2.3). Therefore, the refinement in copper at the high supercooling temperature may caused by the impurity.

The relationship between the length of the laser treated area and the laser energy has been analyzed as before and shown in Figure 33. Both of Cu200-2 and Cu1000-2 have shorter RLS distance when compared with Cu200 and Cu1000, which shows the similar trend with Cu-Nb200. The fixed parameters are listed in Table 7.

In summary the different microstructure caused by the two cleaning process is believed to be related with the minor impurity, although the mechanism is not understood very well. From the above discussion, the minor impurity affects RLS very much and the quality of the film is very critical in this research.

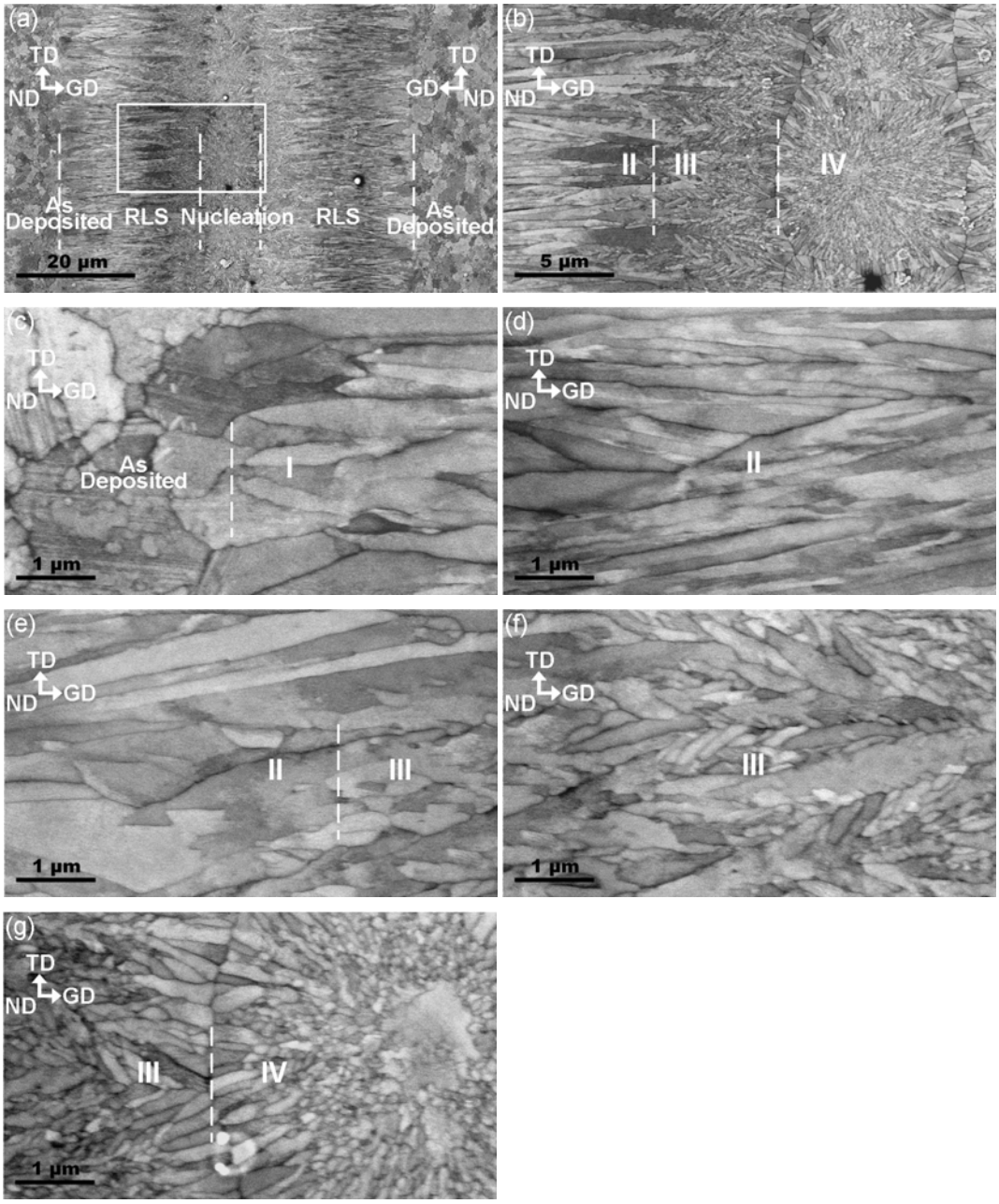

Figure 32. SEM microstructure of laser treated region in Cu1000-2 (E/E_{CM}=1.7).

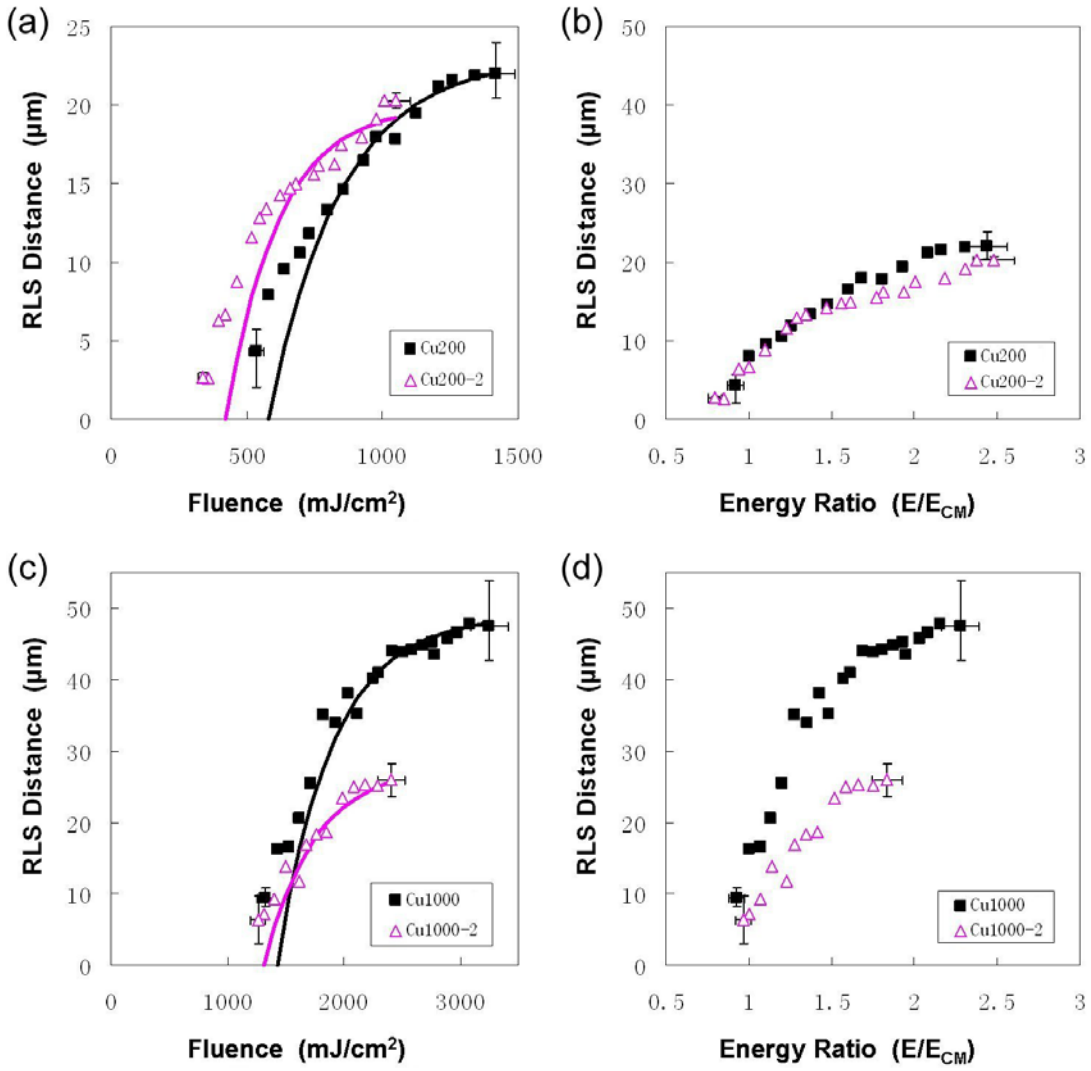

Figure 33. The RLS distance of metal films changes at the different fluence or energy ratio: (a) and (b) Cu200 and Cu200-2, (c) and (d) Cu1000 and Cu1000-2.

Table 7. The parameters are experimentally determined for Cu200, Cu200-2, Cu1000 and Cu1000-2 by Equation 2 and 3.

Metal	E_{CM} (mJ/cm²)	x_{max} (μm)	α (cm²/mJ)	β
Cu200	582	23	0.00378	2.2
Cu200-2	424	20	0.00519	2.2
Cu1000	1428	49	0.00210	3
Cu1000-2	1314	28	0.00228	3

3.5 CONCLUSION

In this chapter, the microstructure and geometric properties of RLS have been studied and discussed in detail. As a result, we found that:

1. RLS can be formed in the Cu, Ag, Au and Cu-Nb thin films. Cu and Ag films have similar RLS microstructures, owing to their similar structural and thermophysical properties.
2. RLS in Cu and Cu-Nb can be divided into zone I, II, III and IV by the variation in mean grain width. Zone III is absent in Ag and Au, with only zones I, II and IV present.
3. The splintering or subgrain formation process is the reason of zone II formation during RLS. It decreases with the increasing film thickness, and zone II becomes unstable in the thicker films. We hypothesize that this process is associated with stress during solidification.
4. The presence of impurities or oxide contamination in the liquid metal appears to disrupt the RLS process, and may be the reason for zone III formation in copper films.
5. Increasing the film thickness, the energy input and the impurity, the maximized RLS distance will be increased.
6. Increasing the film thickness, the mean grain width of RLS will be increased.

4.0 THEORIES OF TEXTURE FORMATION

Texture is defined as the similar orientation existing in polycrystalline materials, and is often quantified by analysis of the X-ray diffraction patterns [3]. Solidification of pure metals can result in a textured polycrystalline microstructure, and has been characterized by previous researchers as summarized in Table 8. It is thought that the <100> texture along GD is due to dendritic growth, while a <111> texture is believed to result from nucleation, and a random orientation is often associated with cellular growth. However, the <100> texture can be formed in either negative (heat is released to liquid) and positive (heat is released to solid) temperature gradients, which means the thermal dendritic growth is not the root reason of texture formation.

It is important to recognize that experimental data on solidification in pure metals is relatively rare, with the majority of work being conducted in alloys. In pure metals, segregation effects are absent, and dendritic morphology during solidification must be the result of heat-flow instabilities (thermal dendrites). Today there remains much confusion about the relationship between the growth mechanisms and microstructure in the solidification of pure metals. The data presented in Table 8 is a compilation of all experimental data that could be found in the literature.

4.1 KINETIC MODELS FOR TEXTURE SELECTION

As the S-L interface moves faster and faster, the kinetics of atoms near the interface becomes more and more important. In RLS, the quench rate can reach 10^7~10^{10} K/sec. Under these conditions, it is recognized that the interface velocity is kinetically limited by the interface response function [21] which can only be studied by simulations. Under these conditions of rapid solidification, MD models [**21**] predict that the <100> grains grow faster than grains with other orientations. Monte Carlo [**35**] modeling of the kinetic attachment of atoms at the interface, as compared with grains with other orientations, also predict the atoms prefer to attach to <100> grains other than the other grains.

Table 8. Summary of texture formation in previous researches. (* is the Authors conclusion)

No.	Author	Method	Method	Material	Purity (%)	$\Delta T_{supercooling}$ (K)	Temperature Gradient (dT/dx)	V_{int} (m/s) or ΔT (K/s)	Texture along GD	Microstructure	Information	
1	K.Grant [36]	Direct solidification casting	Constrained	Cu	\	\	+	\	<100>	*Dendritic		
2	D.A.West [37]	Direct solidification casting	Constrained	Ni Alloys	\	\	+	\	<100>	*Dendritic		
3	G.F.Bolling [38]	Direct solidification casting	Constrained	Pt	99.999	\	+	\	<111>	*Columnar		
4	D.Walton [8]	Direct solidification casting	Constrained	Al	\	(*Low)	+	(*Slow)	<100>	Columnar (*cellular)		
				Al-2%Ag	\	(*Low)	+	(*Slow)	<100>	Columnar (*cellular)		
		Mold casting	Constrained	Pb	99.999	(*Low)	+	(*Slow)	Random	Columnar (*cellular)		
				PbSn Alloys	Pb-99.999	(*Low)	+	(*Slow)	<100>	Columnar (*cellular)		
5	Ch.A.Gandin [47]	Mold casting	Constrained	INCONEL	X750	(*Low)	+	(*Slow)	<100>	*Dendritic		
6	G.Wassermann [47]	Mold casting	Constrained	Al Alloys	\	(*Low)	+	(*Slow)	<100>	Dendritic(*?)		
7	M.J.Tenwick [6]	Spinning	Constrained	Cu	\	(*High)	+	(*Rapid)	<100>	*Columnar	Spinning rate = 35 m/s, thickness = 50 μm	
8	T.Goto [11]	Spinning	Constrained	Cu	99.9	(*High)	+	(*Rapid)	<100>	Columnar (*fiber)	Spinning rate = 1.5~8 m/s, thickness = 2.5~7 μm	
9	M. van Rooyen [13]	Spinning	Constrained	Al	99.998	(*High)	+	>exp(6)	<100>	*Columnar	Top side	Spinning rate = 23.1~46.2 m/s
						(*Super-high)	+	>exp(6)	<110>	Equiaxed(*?)	Wheel side (*nucleation)	
				AlMg Alloys	Al-99.998, Mg-99.38	(*High)	+	>exp(6)	Random	Equiaxed	Top side	
						(*Super-high)	+	>exp(6)	<111>	*Equiaxed	Wheel side (*nucleation)	
				Al-2.4at%Si	Al-99.998, Si-99.99	(*High)	+	>exp(6)	<100>	Dendritic(*?)	Top side	
						(*Super-high)	+	>exp(6)	<100>,<110>	Equiaxed(*?)	Wheel side (*nucleation)	
				Al-7.2at%Si	Al-99.998, Si-99.99	(*High)	+	>exp(6)	Random	*Equiaxed	Top side	
						(*Super-high)	+	>exp(6)	<100>	*Columnar	Wheel side	
				Al-11.4at%Si	Al-99.998, Si-99.99	(*High)	+	>exp(6)	Random	Columnar(*?)	Top side	
						(*Super-high)	+	>exp(6)	Random	Columnar(*?)	Wheel side	

Table 8 (continued).

10	V.G.Shepelevich [30]	Spinning	Constrained	Al	99.99	(*High)	+	>exp(6)	<111>	Columnar(*?)	Thickness = 30~60 μm	
				Al Alloys	Al-99.99	(*High)	+	>exp(6)	<111>	Columnar(*?)		
				Pb	99.99	(*High)	+	>exp(6)	<111>	Columnar(*?)	Thickness = 30~60 μm	
				Pb Alloys	Pb-99.99	(*High)	+	>exp(6)	<111>	Columnar(*?)		
11	B.S.Mitin [48]	Spinning	Constrained	Al	\	(*High)	+	\	<100>	Dendritic(*?)	Top side	Thickness = 70 μm
						(*Super-high)	+	\	<111>	*Equiaxed	Wheel side (*nucleation)	
						(*High)	+	\	<100>	Equiaxed(*?)	Top side (*nucleation)	Thickness = 800 μm
						(*High)	+	\	<100>	Dendritic(*?)	Middle	
						(*Super-high)	+	\	<111>,<110>, <311>	Equiaxed(*?)	Wheel side (*nucleation)	
				Bi	\	\	+	\	<100>	Dendritic(*?)	Spinning rate = 5~15 m/s, thickness = 100~200 μm	
				Zn	\	\	+	\	<100>	Dendritic(*?)	Spinning rate = 5~15 m/s, thickness = 100~200 μm	
12	D.Y.Li [49]	Spinning	Constrained	Al-Alloys	\	\	+	\	Random	Columnar (*fiber)	Top side	Spinning rate = 0.123 m/s, thickness = 18 mm
						\	+	\	<111>	Equiaxed (*fiber)	Wheel side	
13	S.M.Copley [7]	Laser melting from bulk	Constrained	Ni Alloys	\	\	+	\	<100>	*Dendritic		
				Ag-6.6wt%Cu	\	\	+	\	<100>	*Dendritic		
14	K.I.Dragnevski [50]	Supercooled liquid	Free	Cu	99.9999	352	-	>97	Random	*Dendritic	Refinement	
15	K.F.Kobayashi [52]	Supercooled liquid	Free	Cu-O (<300ppm)	\	>100	-	\	<100>	*Dendritic		
16	S.E.Battersby [53]	ALAF, supercooled liquid	Free	Cu-O (600ppm)	Cu-99.9999	40~60	-	1~2	<100>	*Dendritic		
						70~100	-	2~5	Random	*Equiaxed		
						110~180	-	5~35	\	*Dendritic		
						180~250	-	35~60	Random	*Equiaxed	Refinement	
				Cu-3wt%Sn	\	43~73	-	1~2	<111>	*Dendritic	Not fully developed	
						73~193	-	2~30	\	*Dendritic	Well developed	
						193~208	-	30~40	Random	*Dendritic	Mostly	
17	B.L.Jones[3]	Ingot from supercooled liquid	Free	Cu	99.999	207	-	\	\	*Dendritic		
18	D.Y.Li [54]	Ingot from supercooled liquid	Free	Ge	99.999	<300	-	1~5	<110>	*Dendritic	Twin dendrites of <211> to form <110>	
						300~400	-	5~30	Random	*Dendritic	Random increases with the increasing V_{int}	
						400~426	-	30~40	Random	*Equiaxed	Refinement	
				Cu	99.999	207	-	70	<110>	*Dendritic	Twin dendrites (*of <211> to form <110>)	

4.1.1 Theoretical Growth Models for Pure Metal: Rough and Faceted

In the sharp interface model, it is assumed there are two types of S-L interfaces: atomically rough and atomically flat. The continuous/normal growth model and the faceted growth model are set up related to these interfaces, separately. The continuous/normal growth model is useful in explaining the movement of the rough interface presented in Figure 34 (a) where an interface (similar to high-angle grain boundary) can propagate continuously because a large amount of attachment sites.

The velocity near equilibrium for continuous/normal growth is given by [1,19]:

$$v(T) \approx v_c(T_m) \cdot \frac{L_m \Delta T_{undercooling}}{R T_m^2} = k_1 \Delta T_{undercooling} \qquad \textbf{Equation 4}$$

where $v_c(T_m)$ is the maximum growth velocity at infinite driving force, $\Delta T_{undercooling}$ is the undercooling temperature at the S-L interface, L_m is the latent heat, and k_1 is called linear interface kinetic coefficient and is similar to boundary mobility.

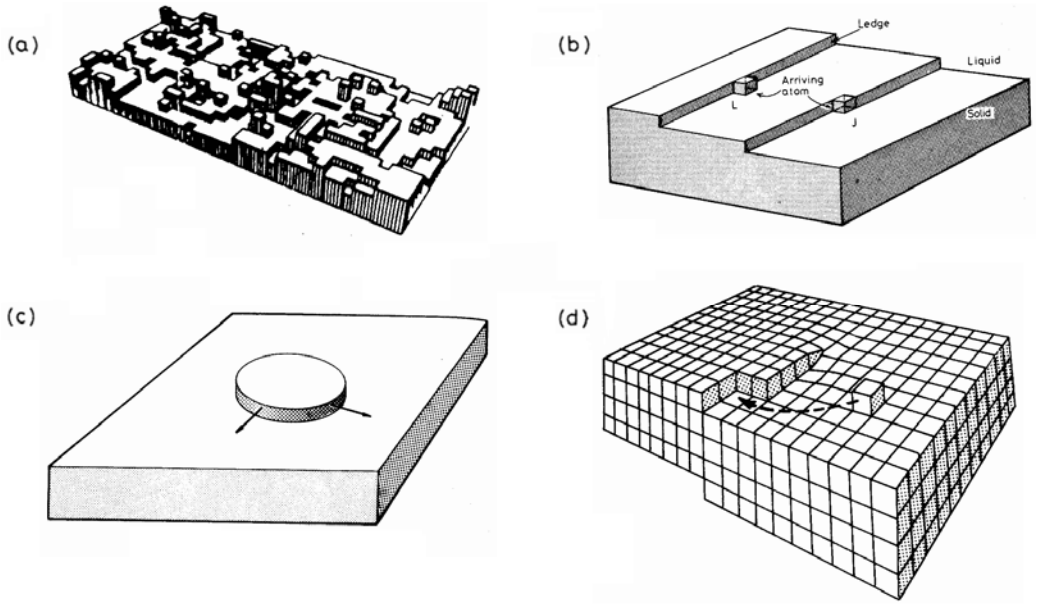

Figure 34. Growth models in pure metal. (a) Continuous/normal growth in the atomically rough S-L interface where there are many sites for atoms to attach; (b) Faceted growth in the atomically flat S-L interface, where ledges and jogs provide sites for surface advance; (c) A ledge is nucleated in the S-L interface; (d) A screw dislocation provides a jog site for spiral growth. [**1**,**19**]

In Figure 34(b)-(d), the faceted growth model are shown for a number of examples of atomically flat, close-packed interfaces. Atoms can only attach to the ledges or jogs existing in the otherwise smooth interface. If the creation of new ledges is caused by surface nucleation (Figure 34(c)) then the normal growth rate is [**1**,**19**]:

$$v \propto \exp\left\{\frac{-\pi\gamma_{ledge}^2 hT_m}{L_m k_B T \Delta T_{undercooling}}\right\} \propto \exp\left(-k_2 / \Delta T_{undercooling}\right) \qquad \textbf{Equation 5}$$

where γ_{ledge} is the ledge energy per unit area, h is the step height, and k_2 is roughly constant.

The dislocations intersecting with the S-L interface can also provide interfacial steps for growth. The spiral growth model in Figure 34(d) shows a jog site generated by a screw dislocation. For small undercooling temperature of the S-L interface, the growth rate is given by [**1**,**19**]:

$$v \propto k_3 \left(\Delta T_{undercooling}\right)^2 \qquad \textbf{Equation 6}$$

where k_3 is a materials constant.

In addition, the kinetic model of phase transformation shows a driving force (ΔG_{LS}) between the solid and the liquid as shown in Figure 35. This force increases as the undercooling temperature of the interface increases, and therefore determines the velocity of the S-L interface is [**36**]

$$v(T) = \frac{6D_L(T)}{a} \cdot \frac{\Delta G_{LS}}{k_b T} = \frac{6D_L(T)\Delta H_{LS}\Delta T_{undercooling}}{a k_b T_m T} \qquad \textbf{Equation 7}$$

where $D_L(T)$ is the diffusion coefficient, a is the lattice spacing, k_b is Boltzmann constant, ΔH_{LS} is the latent heat and T_m is the melting temperature.

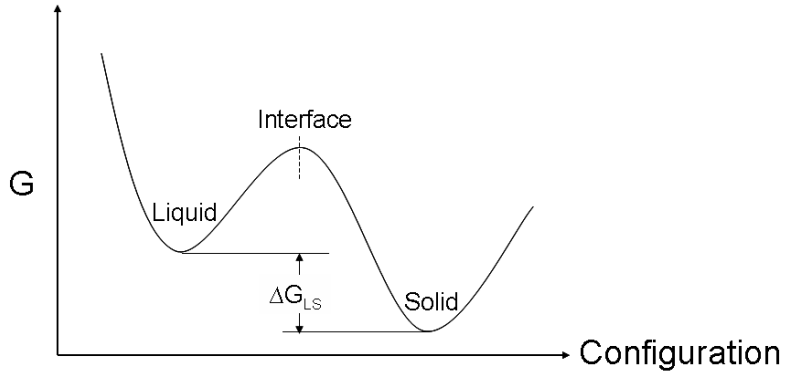

Figure 35. The Gibbs Energy of the liquid, the solid and the interface.

4.1.2 Experimental Relationship of Growth Velocity with Supercooling Temperature

Most pure metals form atomically rough interfaces during rapid solidification. In alloy studies, abrupt changes such as the solidification velocity, partition coefficient, tip solid concentration, and radius have been detected in dendritic growth when the supercooling temperature was increased to about 100 K [**55**]. It was found that the discontinuity is coincident with the onset of spontaneous grain refinement [**56**].

As shown in Figure 36, the solidification of pure Ni was measured as a function of the undercooling temperature ΔT. When ΔT was less than a critical limit, the measured velocities followed a power law $v \sim \Delta T^{\beta}$ [**56-58**], and a linear dependence was found for the undercooling temperature higher than the critical value [**58**].

The theoretical calculation of the solidification velocity for pure metal is shown as the solid line and the total undercooling temperature was derived by [**58**]

$$\Delta T = \Delta T_i + \Delta T_r = (T_i - T) + (T_m - T_i) \qquad \textbf{Equation 8}$$

where the thermal undercooling ΔT_i is the difference between the temperature of the dendrite tip, T_i, and the melt temperature T far away from the dendrite. ΔT_r is the undercooling due to the Gibbs-Thomson effect because of the curvature of the dendrite tip.

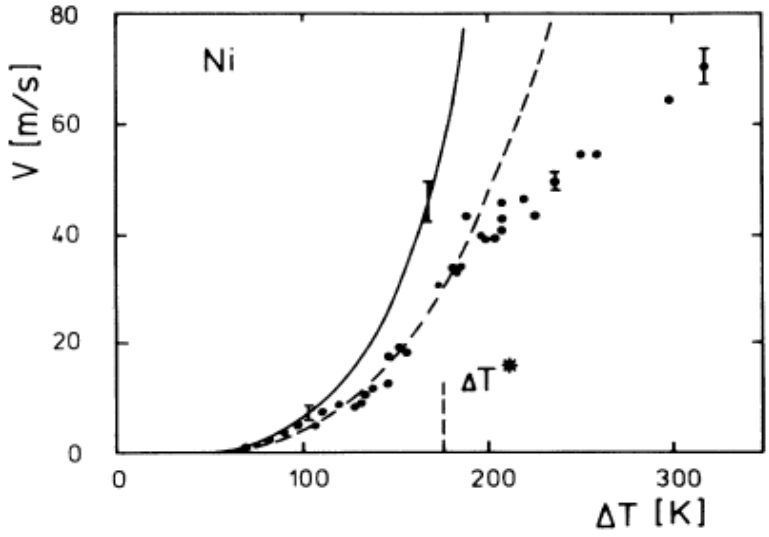

Figure 36. The growth velocity of Ni as a function of undercooling temperature: the solid line was theoretical prediction, and the dashed line was predicted by theory including nonequilibrium at the interface by introducing atomic attachment kinetics. [**58**]

The condition of local equilibrium at the interface was assumed to be relaxed by adding a kinetic term ΔT_k [**58**]:

$$\Delta T = \Delta T_i + \Delta T_r + \Delta T_k = (T_i - T) + (T_m - T_i) + V/\mu \qquad \textbf{Equation 9}$$

where V is the interface velocity and μ is fitted to the experimental results which is the coefficient describing the atomic attachment kinetics at the interface.

The experimental data shown in Figure 36 agrees with the theoretical prediction of an exponential law below a critical undercooling temperature. But above the critical undercooling temperature which was coincident with the onset of the grain refinement, the growth velocity was linear with the undercooling temperature.

However, the undercooling temperature is very hard to measure, especially driving rapid solidification. Most thermocouple or pyrometer technologies are limited by time resolutions of the order of microseconds (μs) and spatial resolutions of the order of microns (μm). Therefore, the experimental data are absent in rapid solidification with a quench rates of more than 10^3 K/s.

4.1.3 MD Simulation

The experimental results for the <100> texture formation during the dendritic growth of FCC metals indicate that the <100> orientation is the favored GD and might grow faster than the others. But it is very hard to measure the growth velocity directly by experiments at present. Therefore, molecular dynamics (MD) simulations have been set up to study the mechanism for solidification by using a Lennard-Jones (LJ) system in the liquid and solid [**21**].

The LJ potential can not only be applied in the noble gases, but also in all of the systems constructed by hard spheres [**21**], and it is considered to be representative of the metallic bonds associated with FCC solids and their melts. At the liquid-solid interface, the excess surface free energies of the {100}, {110} and {111} faces are approximately equal, as is the diffusion coefficient. The interface velocity is assumed to be a function of undercooling which is dependent on liquid diffusion near the interface [**30**].

By assuming that all of the S-L interface sites are potential growth lattices, the rate is given by Wilson-Frenkel function [**21**]

$$v = (Da/\Lambda^2)\left(e^{-\Delta S/k}\right) f\{1 - e^{-\Delta\mu/kT}\} \qquad \textbf{Equation 10}$$

where $D = D_0 \exp(-Q/kT)$ is the liquid diffusion coefficient depending on the energy barrier of Q, a is the atomic layer spacing, Λ is the mean free path in the liquid, ΔS and $\Delta\mu$ are the entropy change and chemical potential change when the atoms in the liquid attach to the solid, and f is the factor to represent the fraction of the effective collision which result in solidification.

However, the mismatch between the solid and liquid atomic space at the S-L interface is increased at low temperature due to the increasing viscous and at high growth velocity due to the preventing relaxation. The growth velocity is given by [**21**]

$$v = (a/\lambda)(3kT/m)^{1/2} f\{1 - e^{-\Delta\mu/kT}\} \qquad \textbf{Equation 11}$$

where the diffusion term is replaced by the ideal gas average thermal velocity of $(3kT/m)^{1/2}$, and λ is the travel distance of the atoms.

The solidification velocity determined by MD simulation is shown in Figure 37, where the solid line is Equation 10 which fits the MD data of <111> growth velocity, and the dashed line is Equation 11 which fits the MD data of <100> growth velocity.

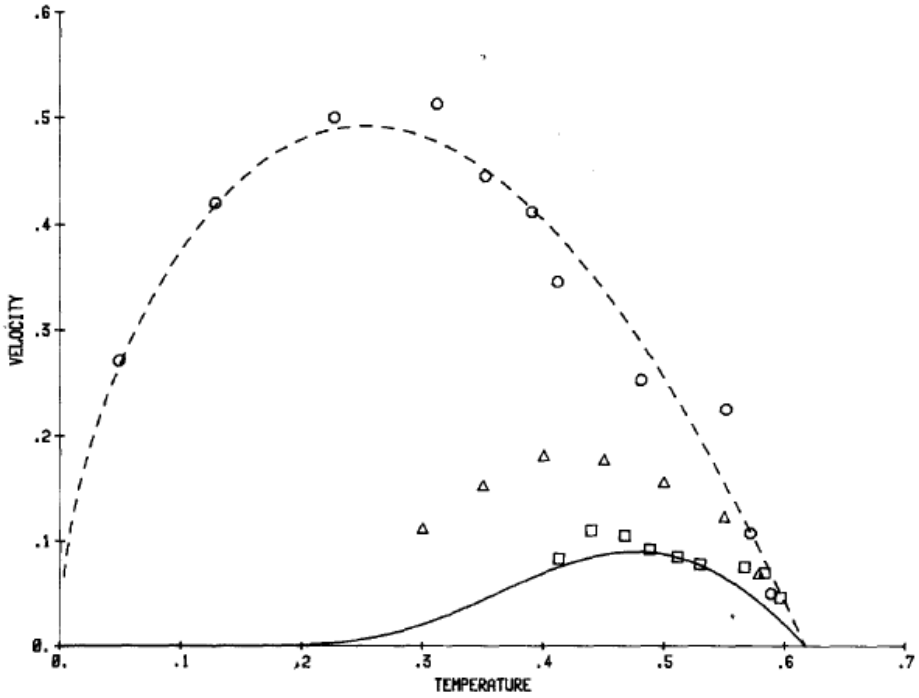

Figure 37. Growth velocity vs. undercooling: open circles are <100> growth velocity and squares are <111> growth velocity. [**21**]

The big difference of the simulated solidification velocities between the <100> and <111> GD at small undercooling is due to the different mechanisms responsible for solidification at the S-L interface. The <100> direction is independent of the S-L interface diffusion and exhibits a continuous growth without energy barriers for nucleation. In contract, the <111> growth is dependent on the S-L interface diffusion and follows the Wilson-Frenkel kinetics.

Thus, MD simulations predict <100> is growth faster than <111> in FCC metals. And this difference is much stronger at high undercooling than that in the equilibrium conditions. Therefore, the <100> texture in the GD appears to be favored by the attachment kinetics at the S-L interface in the rapid solidification of FCC metals.

4.2 THERMODYNAMIC MODELS FOR TEXTURE SELECTION

The energy of the S-L interface is found to be anisotropic according to the arrangement of atoms, where the S-L interface with lower energy can propagate easier than those with higher energy due to the smaller energy barrier. Therefore, the texture formed is the one that minimizes system energy during solidification. This effect is expected to play a role in texture formation under slow solidification where near-equilibrium conditions prevail.

4.2.1 The Minimum Surface Energy Criteria

Some simulations show that the S-L interfacial energy for <111> is lower than that of <100> in pure FCC metals [**20**]. From the minimum system energy criteria, the S-L interface should be the crystalline plane with the lowest surface energy, i.e. {111}. Although the <111> texture formation under the planar growth conditions can be explained very well by choosing the lowest surface energy, the <100> texture formed during the dendritic growth conditions is hard to understand from this aspect.

One opinion [**29**] points out that during the dendritic growth, the <100> dendrite tips can be formed with four {111} planes (shown in Figure 38) but the grains with <111> normal to the surface cannot form the tips. Therefore, the dendritic growth is always pointing to the <100> orientation.

This model is not so convincing when considering the probability of the formation of the <100> dendrites but not the <111> dendrites. As shown in Figure 39, considering the neighbors of grains with the {111} and {100} at the beginning of the solidification, both of concave and convex features can be

formed with {111} planes and grow in the <100> orientation in order to minimize the surface energy. Due to the theory of the thermal instability of the interface, the <100> concave features formed in Figure 39(b) will disappear, while the <100> convex features formed in Figure 39(c) will propagate.

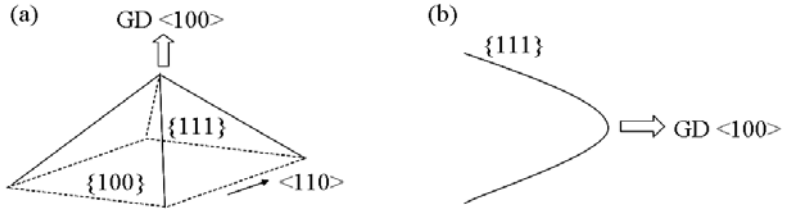

Figure 38. Dendritic tip growth in <100> orientation with four {111} surfaces: (a) schematic representation of the crystalline structure; (b) schematic representation of the dendrites.

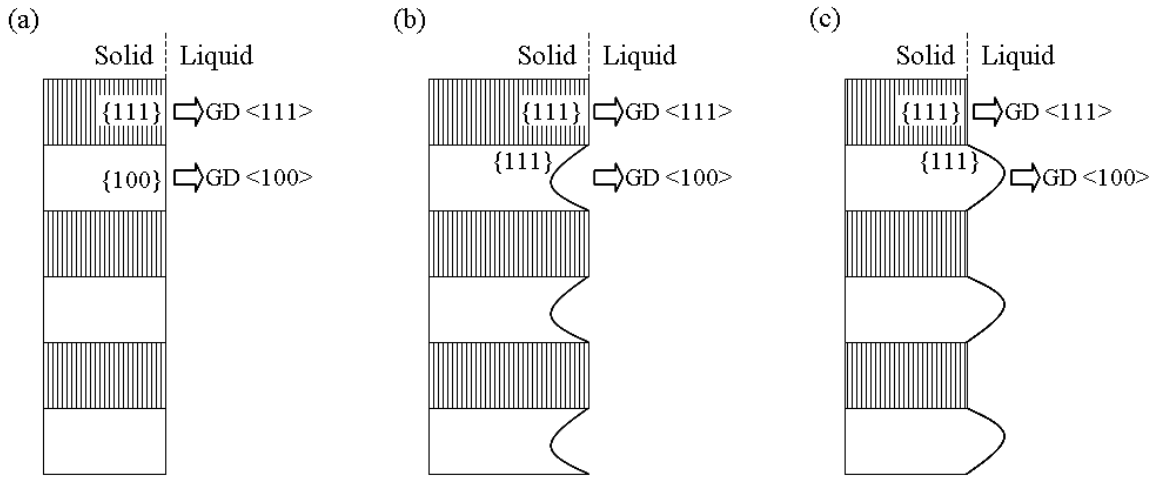

Figure 39. The interface generation with the neighbors of <100> and <111> orientated grains: (a) the beginning planar surface; (b) the concaves formed in the <100> grains; (c) the convexes formed in the <100> grains.

Additionally, as shown in Figure 40, in the grains oriented with <111>, sharper tips can be formed with three {111} planes.

The theory of the minimum surface energy criteria tried to point out the dendritic growth orientation by discussing the structure of the dendritic tips. However, it cannot explain why the <100> bumps but not <100> concaves form during the solidification. And the inability to form <111> tips is not explained either.

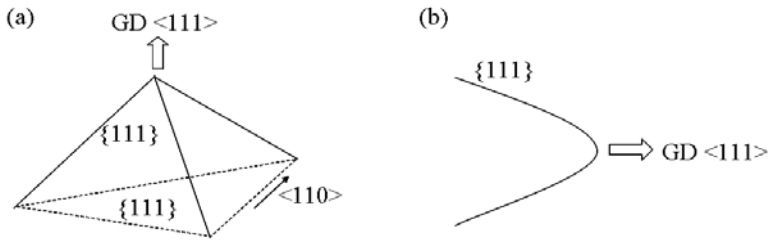

Figure 40. Dendritic tip growth in <111> orientation with three {111} surfaces: (a) schematic representation of the crystalline structure; (b) schematic representation of the dendrites.

Other simulations show that the surface energy of {100} plane are lower than that of {111} plane ($\gamma_{100} < \gamma_{111}$) [**54**]. The S-L interface energy is calculated from the Gibbs driving surface and the potential energy profile by using the number density profile. Due to the lower S-L interface energy, the {100} plane build up faster than {111} plane and therefore <100> texture is formed as the solidification proceeds.

4.2.2 The Minimum Diffusion Energy Criteria

In rapid solidification, the different stacking density between the solid and liquid may affect the texture formation due to the energy barriers of vacancy diffusion.

On the basis of $\gamma_{100} < \gamma_{111}$ [**54**], the preferred orientation is <100> during the solidification. D. Y. Li et. al. [**54**] have studied the role of the packing density in the formation of texture in FCC metals to explain why {111} texture formed instead of {100}. They pointed out that if the surface-packing density of the liquid, ψ^L, was higher than that of the solid, ψ^S, a forward vacancy diffusion was required for the solidification process, where the driving force was given by

$$\Delta G = \frac{\Delta T L_v}{T_m}\left[1 - \frac{kT\sqrt{\frac{2}{3}}\Delta\psi}{L_v v_{atom}} \ln\left(\frac{\sqrt{\frac{2}{3}}\Delta\psi}{v_{atom}}\right)\right] = \Delta G^*(1+D) \qquad \textbf{Equation 12}$$

where $\Delta G^* = (\Delta T L_v)/T_m$ was the traditional defined driving force, and D was the factor of the additional energy which was required to create active vacancies to make ψ^L lower than ψ^S in the condition of higher density liquid.

In order to calculate the D factor for the closed-packed liquid, the surface-packing density of the closed-packed liquid was assumed to be 0.8 and that of the loose-packed liquid was 0.735, and the {111} and {100} planes were 0.907 and 0.785, respectively [**54**]. The calculations points out that only {111} surface does not ask for the additionally diffused energy during the solidification of the closed-packed liquid. [**54**]

The density of the liquid in front of the S-L interface is hard to measure and therefore cannot be experimentally examined. And the equation requires zero diffusion energy for both {111} and {100} interface with the loose-packed liquid. So, this theory is limited to the closed-packed liquid solidification. This mechanism is not accepted widely.

4.2.3 The Minimum Solid-Liquid Surface Energy Criteria

The special grain boundary (GB) with lowest energy (twins and low angle GB), is formed during solidification, deformation, annealing and so on [**1**]. D. Y. Li et. al. [**54**] derived the system energy change by assuming that the addition of new solid in the presence of a GB during solidification was determined by the minimum energy criteria.

Under the planar interface growth conditions as shown in Figure 41, the change of the system energy was given by [**54**]:

$$\Delta E = Wt(\gamma_{100} - \gamma_{111})\cot\varphi + W\gamma_{GB}\frac{t}{\sin\varphi} \qquad \textbf{Equation 13}$$

where φ was the angle between the surface of the grain and the grain boundary which was smaller than 90 degrees by assuming the interfacial energies are $\gamma_{100} < \gamma_{111}$ [**54**]. So, in this model a {100} texture was favored.

For the solidification with a closed-packed liquid, the additional energy for {100} plane growth was given by [**54**]

$$\Delta G_{add} = \left(\frac{1}{2}\frac{Wt^2}{\tan\varphi} + xWt\right)\Delta G^* D_{100} \qquad \textbf{Equation 14}$$

Because both of the S-L interface energy and the additional energy affected the texture growth, the ratio of $\frac{|\Delta\gamma_{SL}|}{\Delta G_{add}}$ would determine which one was more important during the growth selection which is given by [**54**]:

$$\frac{|\Delta\gamma_{SL}|}{\Delta G_{add}} = \frac{2\left(\gamma_{SL}^{111} - \gamma_{SL}^{100}\right)}{(t + 2x\tan\varphi)\Delta G^{*} D}$$ **Equation 15**

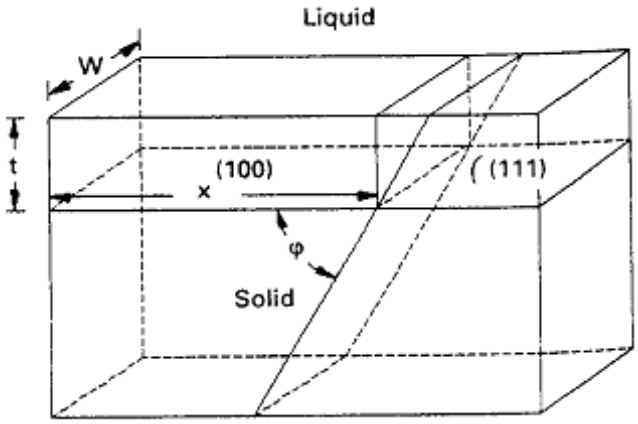

Figure 41. Growth of a bicrystal with {100} and {111} planes parallel to the S-L interface. [**54**]

4.2.4 Interfacial Instability Model - Thermal Dendrite Formation

There are two types of S-L interface movements in pure metals caused by the effect of heat flow on the S-L interface: stable and unstable. [**1**]

As shown in Figure 42(a), when the temperature of the liquid is higher than that of the solid there is a positive temperature gradient extending into the liquid. In this case, heat will transfer from the liquid to the solid [**1**]. Any perturbations in the planar interface will disappear because heat flux in the vicinity of the perturbation is reduced. Therefore, the S-L interface moves into the liquid as a planar surface (stable), which can be defined as the locally constrained solidification. Under conditions of planar growth, cells associated with grain boundaries, collections of defects, or composition variations in the case of alloys, can be formed and is called cellular growth [**1**,**19**]. Since there is no growth anisotropy, there can be no texture formation in the solidification of planar growth or cellular growth.

However, if there is a supercooling in the liquid with a negative temperature gradient (shown in (b)), the heat transfer is reversed. Here, any perturbations will increase the heat transfer, and magnify the perturbation (unstable) [**1**]. At the same time, the latent heat is released to the surrounding liquid and can slow the growth of the neighboring grains near these bumps. This instability produces undulations in the interface, which can grow, and are known as thermal dendrites.

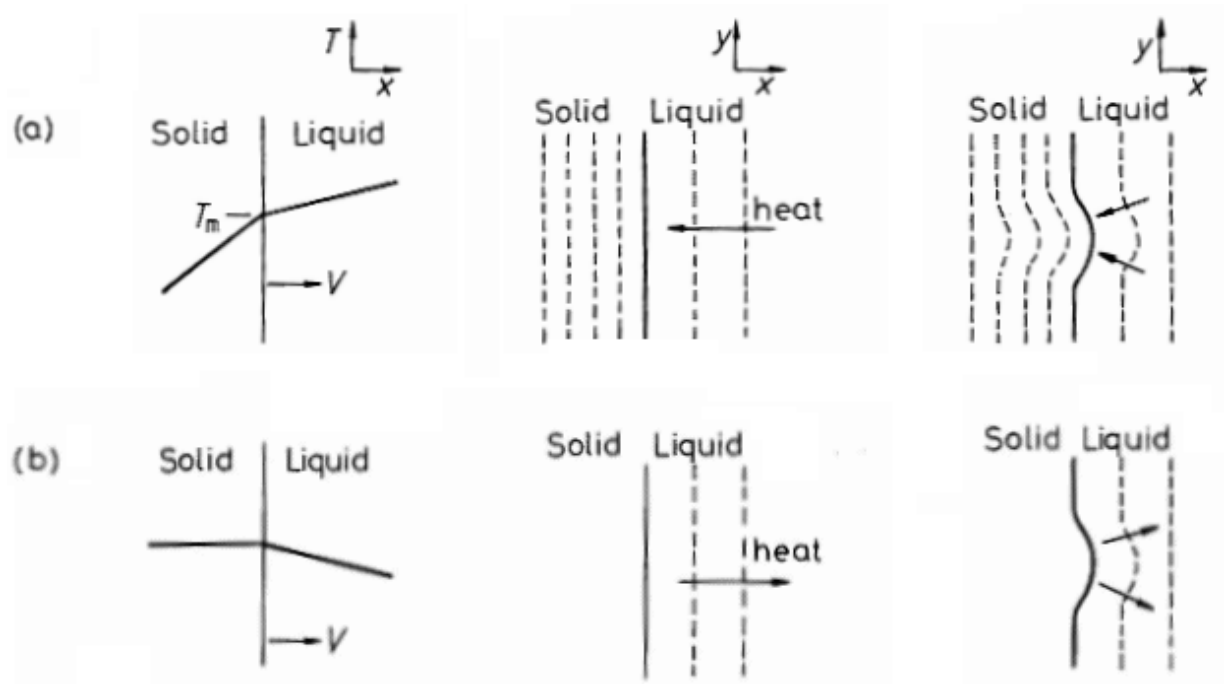

Figure 42. Effects of heat flow on the S-L interface stability. (a) Heat transfer from liquid to solid which prohibits the formation of protrusion in the S-L interface and produces a planar growth of solid; (b) Heat transfer from solid to liquid where the perturbations in the S-L interface are supported and the dendrites are favored. [**1**]

Although texture formation is not necessarily related with dendritic growth in the theory, the dendritic growth can amplify any protrusions in the S-L interface. So, whenever there is an anisotropic growth existing in the system, this anisotropy will be amplified by the dendritic growth and much stronger texture will be formed during solidification.

In a number of previous experiments, dendritic growth is commonly associated with texture formation [**29**,**8**]. In these papers it is concluded that during dendritic growth, the texture of favored orientation (<100> in FCC and BCC) is formed at the early stage of the columnar zone in casting by eliminating the unfavored orientation [**2**]. These results support our discussion of dendritic amplification in texture formation.

In rapid solidification of alloys, the microstructure for a given alloy composition changes with the increase of solidification rate in the sequence: planar, cellular, dendritic, cellular and planar. As shown in Figure 43, the dendritic growth is found in a special range of solidification velocity relatively with the supercooling temperature [**2**], where the transition between cellular growth and dendritic growth is not well understood. The dendritic growth of pure metal is thermal dendrites is due only to the instability of S-L interface, and no such sequence has been reported.

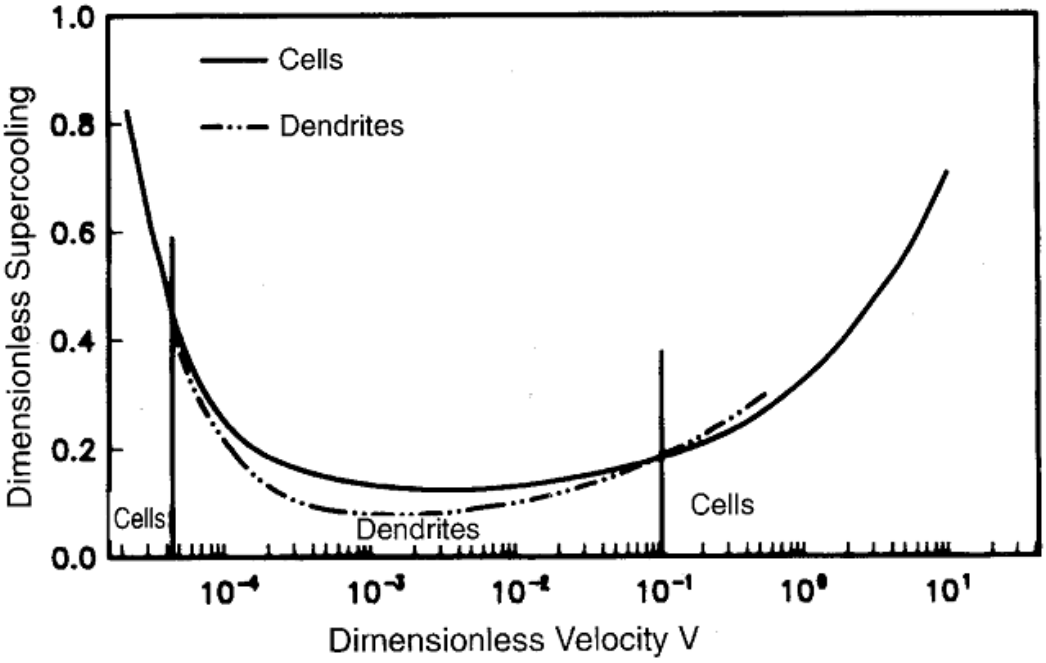

Figure 43. The conditions of supercooling temperature and velocity for cell or dendrite formation in alloy. [**19**]

4.3 SUMMARY – CURRENT MODELS FOR TEXTURE FORMATION

As discussed previously, the proposed mechanisms for the texture formation can be divided into three types.

4.3.1 Kinetic Anisotropy: <100> Grows Faster than Other Orientation in FCC Metals

In this model, as shown in Figure 44, grains with <100> poles aligned closely with GD grow faster and occlude the <111> grains during the solidification. And in those grains with <100> GD, the grains with a <010> orientation in TD will expand faster than the other orientation, such as <012>. Then the competition in GD and TD will result in the <100> texture in both GD and TD. As found in the previous work, both super liquid solidification and melt spinning of pure FCC metals [**11**,**48**] will form <100> texture during the solidification although the previous solidification has a negative temperature gradient and the latter one a positive temperature gradient. This supports the model that anisotropic growth is not necessarily caused by the different temperature gradient but instead is due the anisotropic crystalline growth rate.

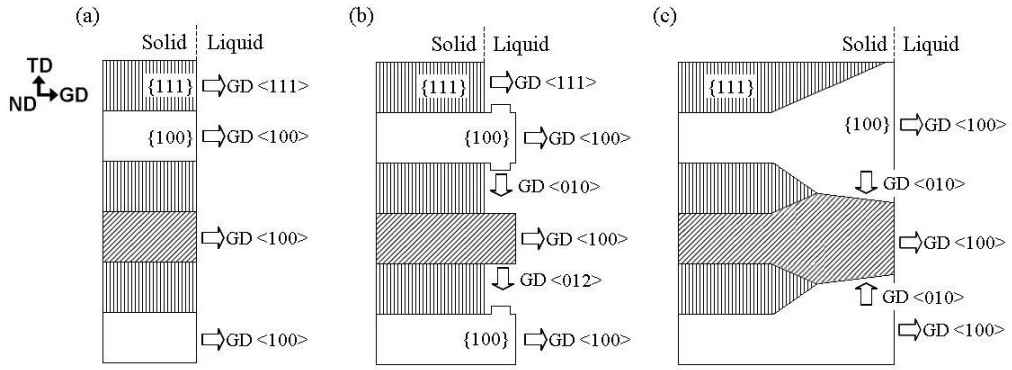

Figure 44. <100> grows faster than <111> during solidification: (a) beginning of the solidification; (b) <100> grows faster and make bumps at the interface; (c) <100> expands and replaces <111>.

4.3.2 Thermodynamic Anisotropy: Atoms Prefer {100} to Eliminate the Total Energy.

In this model, the GB directions determine the microstructure and texture formed during solidification. If the atoms can attach to <100> grains easier than the other grains and form a GB with lowest energy as shown in Figure 45, the <100> texture may be formed during solidification even in the planar growth and without dendrite formation. In fact, the GB with lowest energy, such as twins and low angle GB, has been found in solidification and annealing. In this way the lowest system energy can be achieved during solidification. This model can be supported by minimum GB energy, minimum interface energy and dendritic growth.

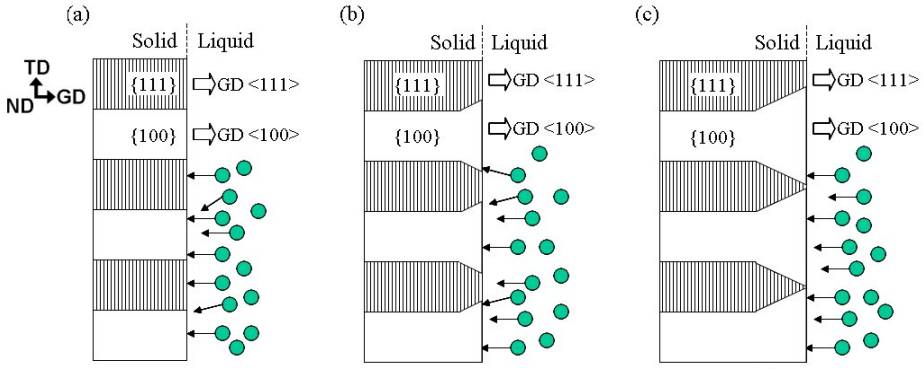

Figure 45. Atoms attach on the <100> easier than <111> at the GB: (a) beginning of the solidification; (b) the direction of GB inclines to <111> and expands <100>; (c) propagation of <100>.

4.3.3 Dendritic Instability Amplification: Amplifies Kinetic or Thermodynamic Anisotropy

In this model, the thermal dendritic tips can be formed when the solid grows into the supercooled liquid with a negative temperature gradient. During this process, the dendritic tips advance into the supercooled liquid, warming the surrounding liquid and eliminating the neighbors.

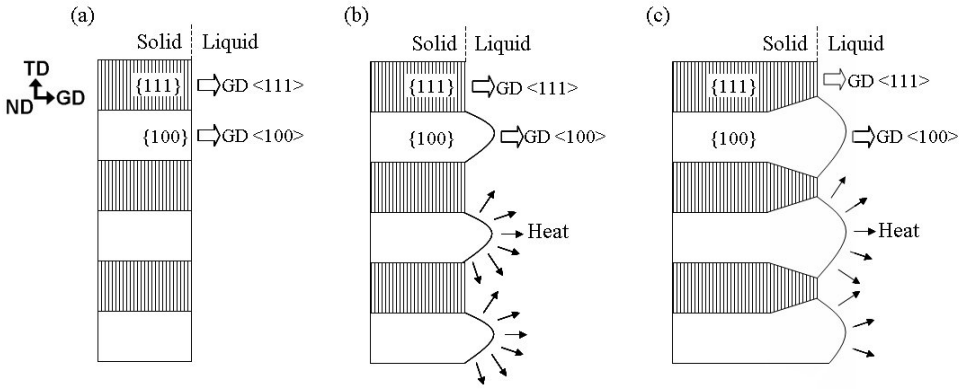

Figure 46. {100} moves a little faster than {111} during solidification: (a) beginning of the solidification; (b) {100} forms dendrite tips into the liquid; (c) the heat flow magnifies the <100> texture and eliminates the growth of <111> grains.

In fact, the <100> grains grow more quickly into the liquid than others at the beginning, and then these <100> dendrite tips are magnified by the heat flow instability. Therefore, the <100> texture becomes stronger and stronger as the solidification proceeds (shown in Figure 46). This agrees with the previous model of anisotropic growth, but here adds the magnification of this anisotropy by the effects of thermal dendritic growth.

Alloy dendritic tips have the same amplification on the anisotropic growth.

In summary, the dendritic instability is not the reason of the anisotropic growth, but only amplifies the anisotropic growth during solidification.

4.4 MODELS FOR TEXTURE FORMATION IN RLS

Although a lot of mechanisms have been proposed by previous researchers to explain the texture formation, it is not yet well understood specifically in the followed basic questions:

1. Which model for texture formation is correct under the conditions of RLS, kinetics or thermodynamics?
2. How does the interface move with the different undercooling temperature, and what are the kinetic limitations governing the S-L interface velocity?
3. What affects the texture along the growth direction GD? Is it solidification velocity, undercooling temperature, material or other factor?

In the preliminary work with RLS, the Cu film showed a strong <100> preferred orientation in GD and <001> and <011> texture in ND by both Kikuchi pattern in TEM and OIM analysis in SEM, which is consistent with most of the previous research in the literature. But in the Ag film a different <112> texture in GD was found. At present, we cannot point out the mechanism of this difference between Cu and Ag films.

However, it was expected that changing the laser energy, thickness of the thin film, annealing and so on would enable the study of the texture formation under the different conditions. In addition, if the texture formation changed with the different solidification conditions, we can possibly control or engineer special textures by adopting RLS conditions to achieve optimally electronic properties.

Based on the information in Table 8 and the existing models, we attempted to develop a universal model for the formation of preferred texture in pure metals. This model considers the effects of interface anisotropy, kinetic anisotropy, thermodynamic anisotropy and dendritic amplification to the occlusion process in an advancing solidification front. As shown in Figure 47, if solidification originates from a randomly oriented polycrystalline solid, as in the case of RLS, the initial stages of growth will produce a columnar structure. It is commonly accepted that a columnar structure can grow by the advance of a planar interface, as in the case of constrained solidification. For pure metals in free solidification, the interface can be unstable due to heat flow and dendritic tips can extend forward into the melt. In the absence of secondary arms, the dendrite tips can form a cusped interface but lead to a columnar grain structure that is virtually indistinguishable from planar solidification. In RLS, we observe a columnar morphology in zone II, which can be the result of either planar or dendritic solidification. As solidification proceeds and columnar grains are produced, a texture can form only in the case of

anisotropic growth that allows grains with preferred orientations to occlude neighboring grains. Such an anisotropy can be kinetic or thermodynamic in origin as described below.

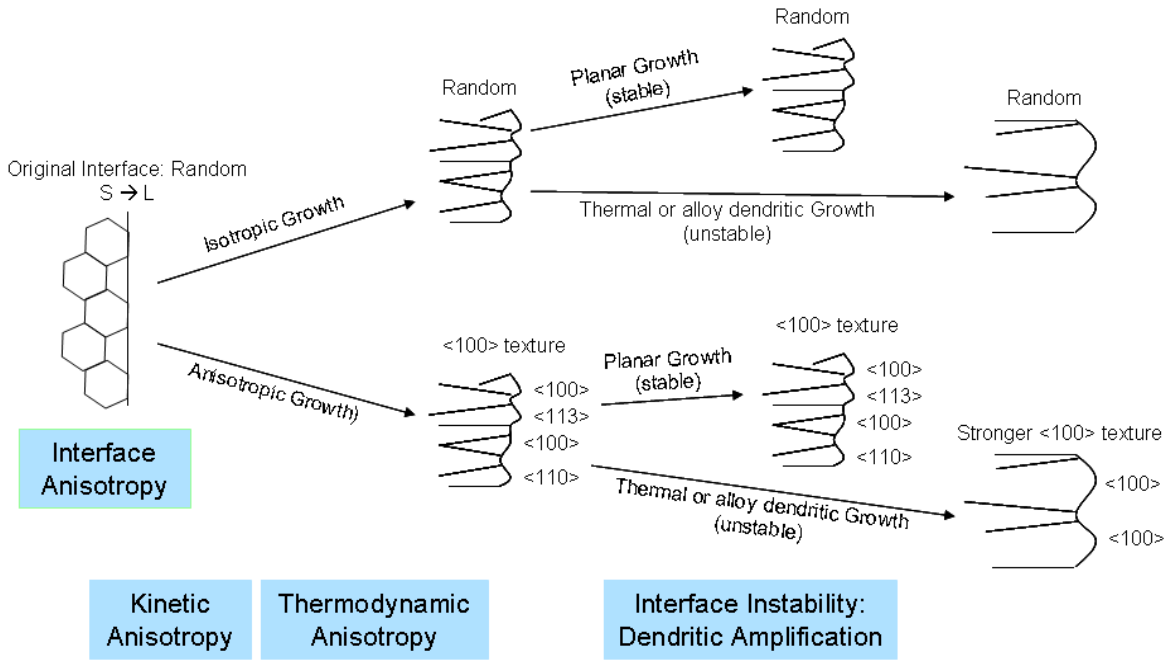

Figure 47. Universal map for texture formation in pure metals.

In the case of rapid solidification of pure FCC metals, the interface is expected to be atomically rough, without facets [1,19]. Although this would suggest that all orientations of the S-L interface would appear identically rough at an atomic scale, it is still possible that growth anisotropy can exist and provide a small kinetic or thermodynamic bias toward growth of preferred orientations. For example, the solidification of Cu likely grows with an atomistically rough surface but with a strong <100> texture in our RLS experiments. Although there are a number of fundamental thermodynamic and kinetic models for anisotropic growth, including simulation, the exact nature of this is anisotropy is currently unknown.

Dendritic growth is often associated with texture formation in polycrystalline solid formation, and arises from interfacial instabilities that allow local regions of the S-L interface to advance more quickly into the liquid. In RLS of pure Cu, we propose that a dendritic instability, if it exists must be associated with heat flow (thermal dendritic instability). Nonetheless, it is important to recognize that in pure metals, dendritic growth can only amplify the underlying isotropic or anisotropic growth mechanism. We have

called this effect as dendritic amplification in Figure 47, where the isotropic growth would continue even as dendritic structures, while anisotropic growth causes stronger anisotropy during the dendritic growth.

We propose that the observed <100> texture is the result of a yet-unknown growth anisotropy at the S-L interface, kinetic or thermodynamic in nature. In this model, the anisotropy may only provide a slight enhancement to growth of a rough surface with a large scale orientation along preferred directions. Furthermore, we believe this anisotropy is amplified by dendritic growth, of solid into the supercooled liquid pool. By changes to the process parameters of RLS, such as substrate, laser fluence, film thickness, and material (Cu vs. Ag), it should be possible to change the solidification temperature and solidification velocity, thereby affecting the kinetic and/or thermodynamic anisotropy. In the sections here, all of the available models of texture formation available in the literature are classified as above, though the exact ones in RLS are still unknown.

5.0 EXPERIMENTAL RESULTS – TEXTURE FORMATION

For the purpose of a systematic discussion, the relationship between the geometric orientations of the metal films and the atomic lattice is established in Figure 48. The normal direction of the film is specified as (ND), and the direction of resolidification is called the growth direction (GD), which indicates the S-L interface movement. The perpendicular direction or transverse in-plane (TD) is defined by ND×GD. The orientation of the atomic lattice inside the grain is specified by $\hat{i}$, $\hat{j}$, and $\hat{k}$. Here <100> directions are adopted. The mis-orientation (or miscut) of this growth direction (GD) relative to <100> is specified as angle θ_g, and the angle between ND and $\hat{k}$ as θ_n.

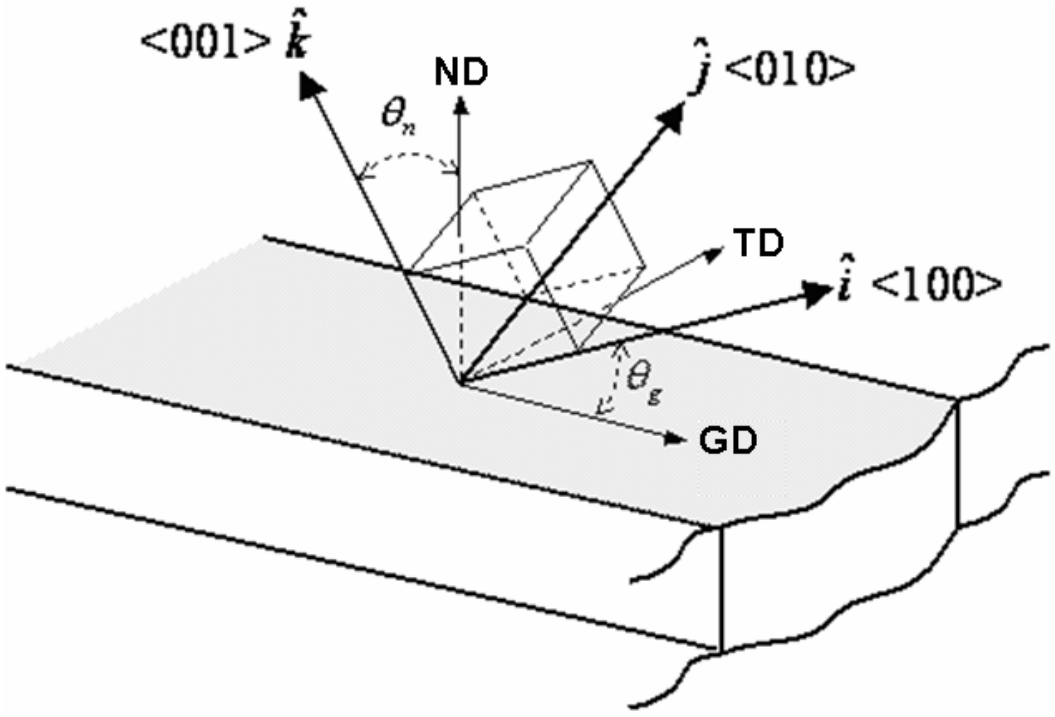

Figure 48. Coordinate systems of sample versus orientation of crystalline lattice.

5.1 TEXTURE FORMATION IN METAL FILMS

5.1.1 TEM Study of Preferred Orientation in Cu Films

Copper films processed by RLS were characterized and found to have a <100> texture in the growth direction (GD). The texture information was collected from Kikuchi patterns by TEM one by one. In the analysis, 35 points of zone I and II were selected for crystal orientation analysis by Kikuchi patterns. The detailed analytic information is given in Appendix A. In Figure 49(a), the points marked 1 to 14 are located in the stable growth zone II, while those marked 15 to 17 are located in the occlusion zone I. The orientations of these 35 grains are plotted in the defined GD, TD and ND system (Figure 50). A strong texture of <100> is shown in this pole figure, where 22 of 35 have <100> poles in the range of $\theta_g \leq 12^\circ$ (the angle between $\hat{i}$ and GD).

Furthermore, nearly 2/3 of the crystal lattice directions of $\hat{k}$ <001> cluster near the normal direction of film (ND). As well, most of the other crystals analyzed cluster approximately 45 degrees from ND, with <011> direction approximately aligned with ND.

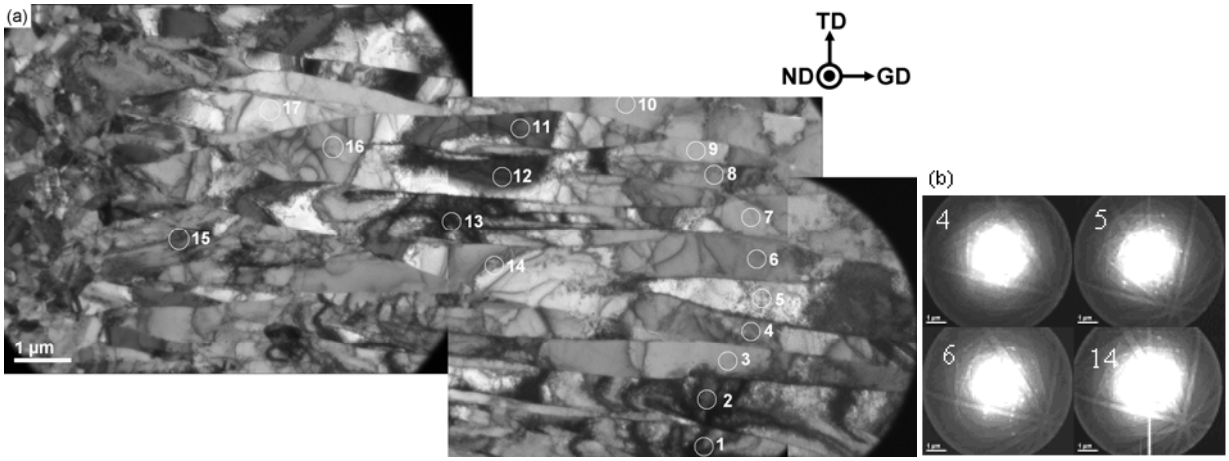

Figure 49. (a) TEM image of laterally solidified microstructure with 17 spots being analyzed by Kikuchi pattern for texture study; (b) Kikuchi patterns of grains belong to a family.

In order to understand the propagation of sub-grains in the stable growth zone (II), all the sub-grains originating from the same grain are defined to be a family. Here detailed analysis of grains belonging to a

single family is chosen for study, with Kikuchi patterns represented in Figure 49(b). Grain 14 (θ_g =6˚) is obviously a successful one which splits to grain 4 (θ_g =10°) and 6 (θ_g =8.6°), while 5 (θ_g =6.4˚) seems to be a new grain generated from 14. During the formation of these sub-grains, grain 4 shrinks to a narrow one and 6 has no change in width, but 5 grows wider. So, for these sub-grains, the larger θ_g appears to result in less ability to grow. All of the grain orientations given in the pole figures are listed in Appendix A and B.

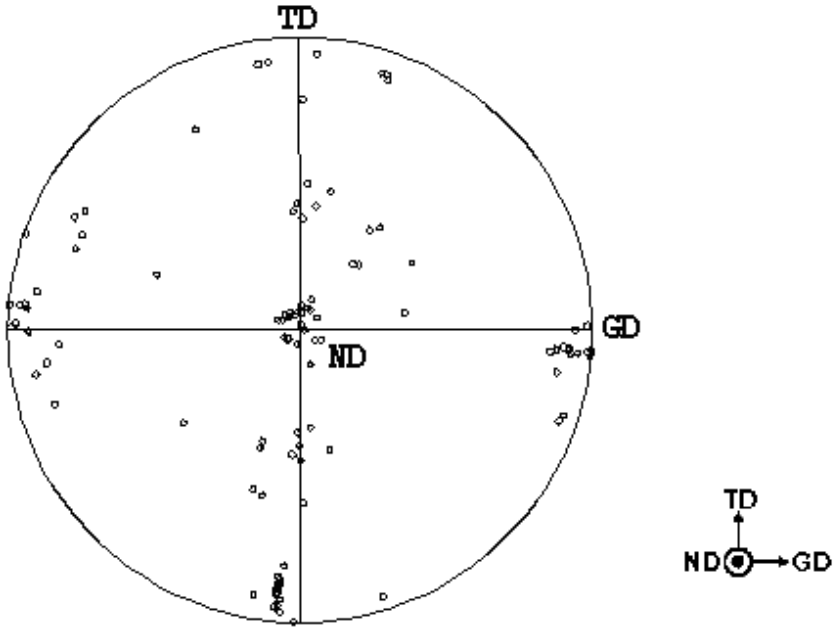

Figure 50. <100> pole Figure obtained from Kikuchi patterns in TEM for 35 Cu grains.

In summary, this TEM data indicates a strong texture in the copper RLS, i.e. <100> is the favored orientation in GD, and ND is mainly dominated by <100> and <110>. Due to the limited number of grains studied, the TEM data describe the number ratio of the grains, with which the most grains are believed to be solidified in the preferred orientation. Although TEM characterization can provide precise determination of the crystalline lattice and identify defects in the RLS microstructure, it is currently possible to analyze only a small number of grains. For this reason it lacks the statistical information necessary to properly quantify texture. To overcome this, we selected SEM analysis as an alternative, primarily for its easier setup, sample preparation, and statistical analysis tools.

5.1.2 SEM-EBSD Characterization of Texture in Cu Films

It is believed that the grains with the favored orientation will grow by eliminating the neighbors during RLS, i.e. there is a complicated relationship between the number ratio and the area ratio of the preferred orientation. The TEM data describe the number ratio of the grains, with which the most grains are believed to be solidified in the preferred orientation. In contrast, EBSD data describe the area ratio of the grains, in which the measured texture is dominated by the large grains Therefore, we assert that either TEM or EBSD can represent the RLS texture, and the data should show a similar trend.

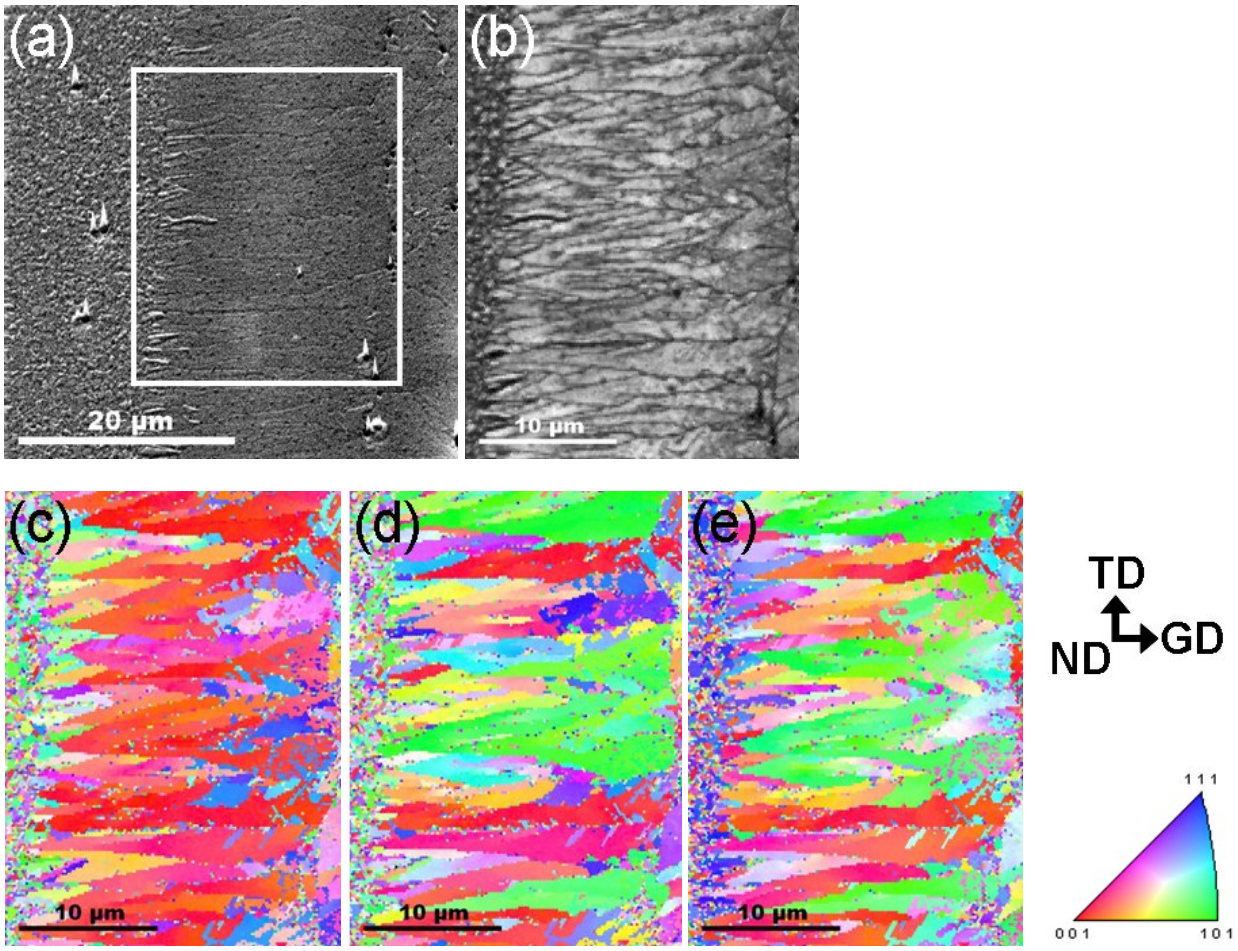

Figure 51. Example of EBSD dataset collected from RLS microstructure for Cu200 with E/E_{CM}=2.3. (a) Plan view image, (b) IQ image, (c) Orientation map along film growth direction (GD), (d) Orientation map along transverse direction (TD) and (e) Orientation map along normal direction (ND).

In order to find out the formation and change of the texture/orientation throughout the full solidification distance, the copper/gold/silver films are imaged by the SEM in the EBSD mode, and the orientation image map (OIM) is collected for over more than 200 grains in each film.

Figure 51(a) shows the microstructure of the copper film, where the denoted square is one of the scanned areas for the OIM. Figure 51(b) is the Image Quality (IQ) image for the scanned area, showing the grain boundaries and defects. Figure 51(c), (d) and (e) are the OIM at the same area, indicating the GD, TD and ND textures. <100> (red) is found to dominate the GD, where the red grains are heavily coarsening during the RLS, and might eliminate the neighbored grains. But both <100> (red) and <110> (green) dominate the ND in the RLS area.

As discussed before [41], the as-deposited copper film has a weak <111>-fiber texture in the normal direction (ND) by X-ray diffraction analysis. The RLS of the copper film is not affected by the as-deposited grains and obviously changed to a new texture. This texture formation is studied by comparing the pole figures at the different RLS distance.

As denoted in the images (Figure 52), the "RLS distance" is defined as the perpendicular distance between the measured point and the edge line. Every pole figure is generated according to the collected OIM data on 6 randomly selected columns (1 μm wide and 35 μm long) at the denoted RLS distance. Since the average grain width in zone I is less than 1 μm, the growth competition of more than 200 grains in the RLS are analyzed in each sample.

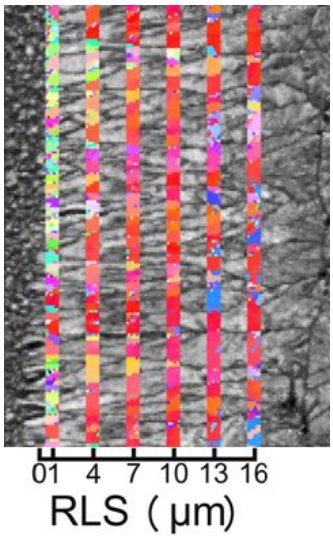

Figure 52. OIM data of copper films are collected at the denoted RLS distance, where each picked area is 1 μm wide and 35 μm long.

The GD, TD and ND pole figures of the copper films are generated at the RLS distance from 1 μm to 34 μm. Figure 53 to Figure 64 show the pole figures of Cu100, Cu200, Cu500 and Cu1000 at the different energy ratio of 1.2, 1.7, 2.3 and 3.0.

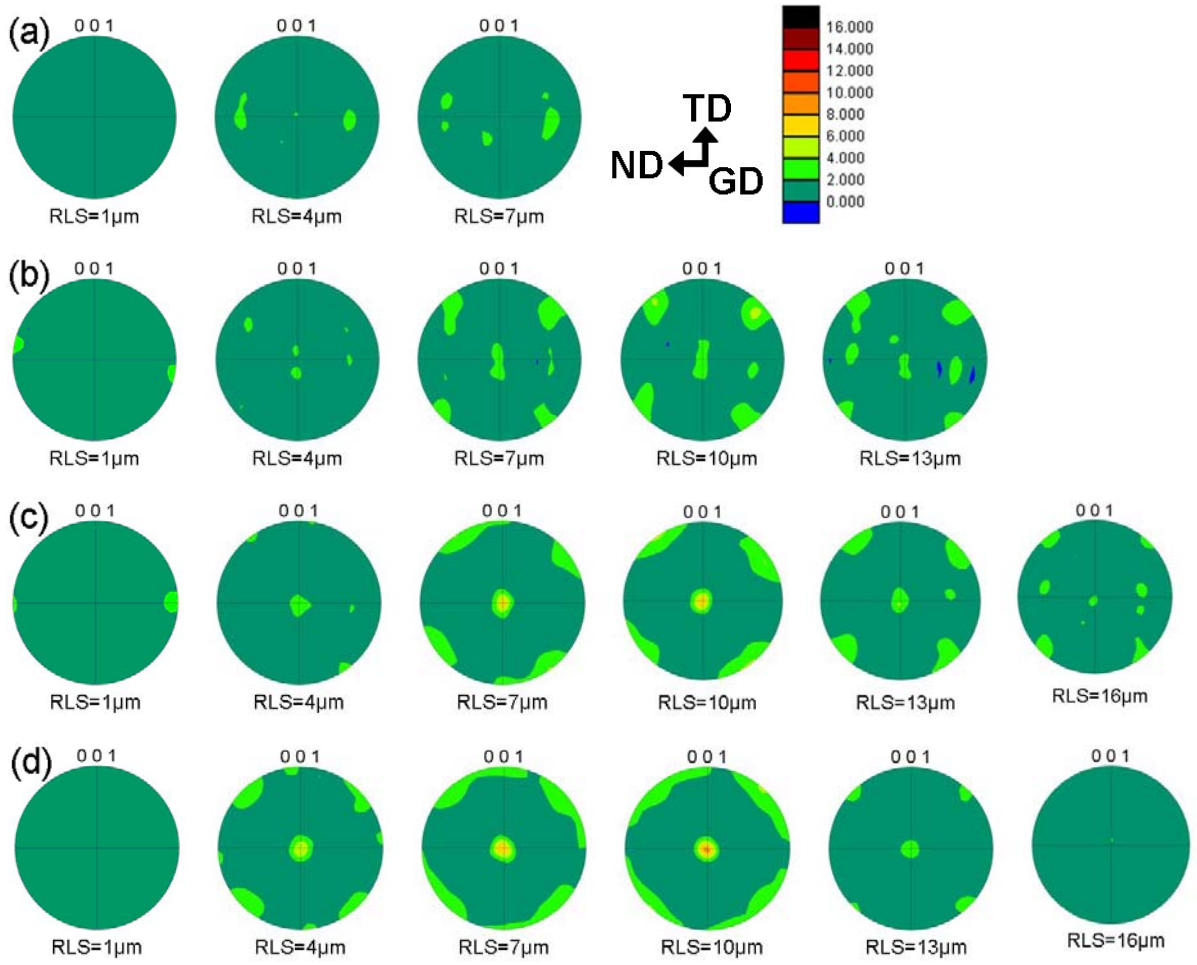

Figure 53. GD pole figures of Cu100 at RLS=1 μm to 16 μm: (a) E/E_{CM}=1.2, (b) E/E_{CM}=1.7, (c) E/E_{CM}=2.3 and (d) E/E_{CM}=3.0.

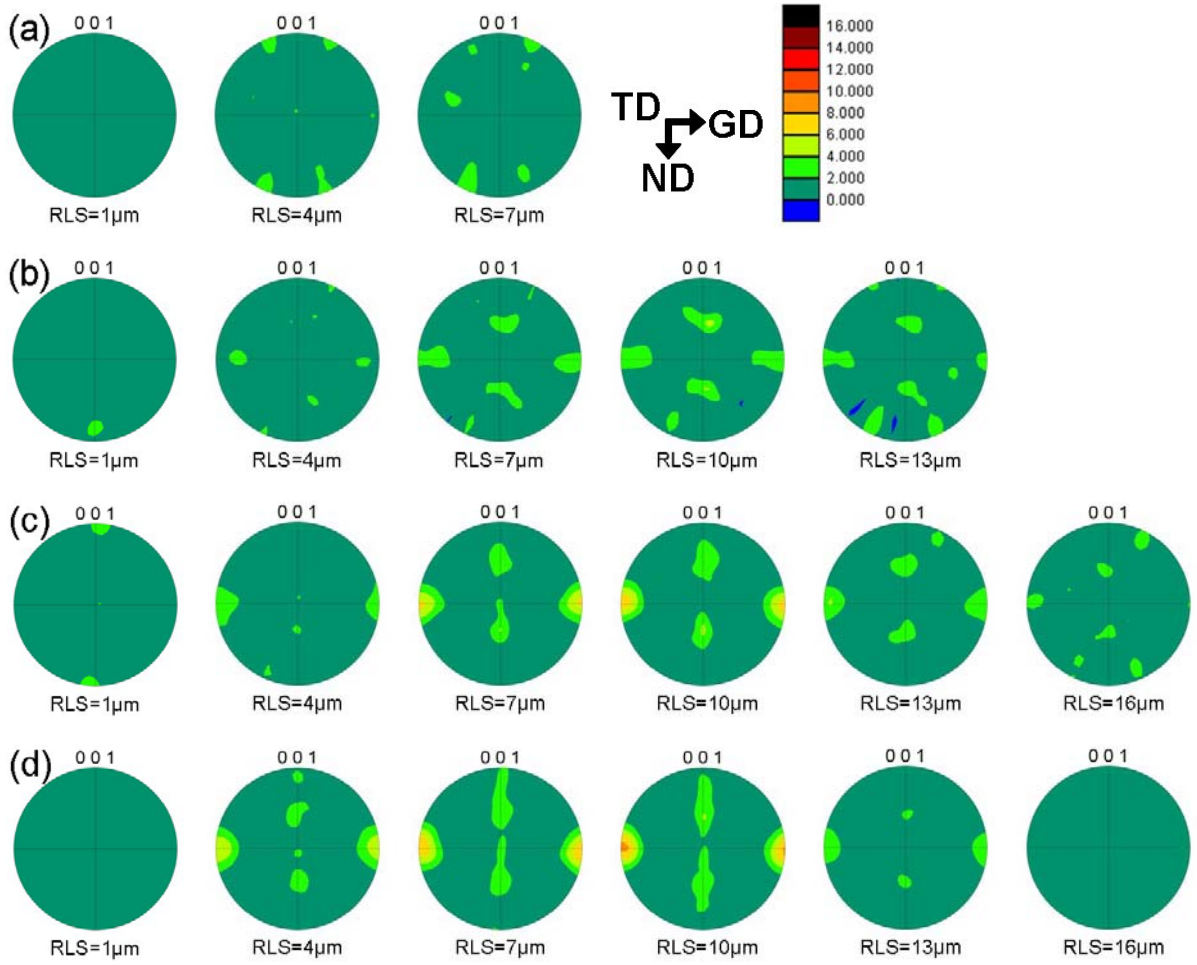

Figure 54. TD pole figures of Cu100 at RLS=1 μm to 16 μm: (a) E/E_{CM}=1.2, (b) E/E_{CM}=1.7, (c) E/E_{CM}=2.3 and (d) E/E_{CM}=3.0.

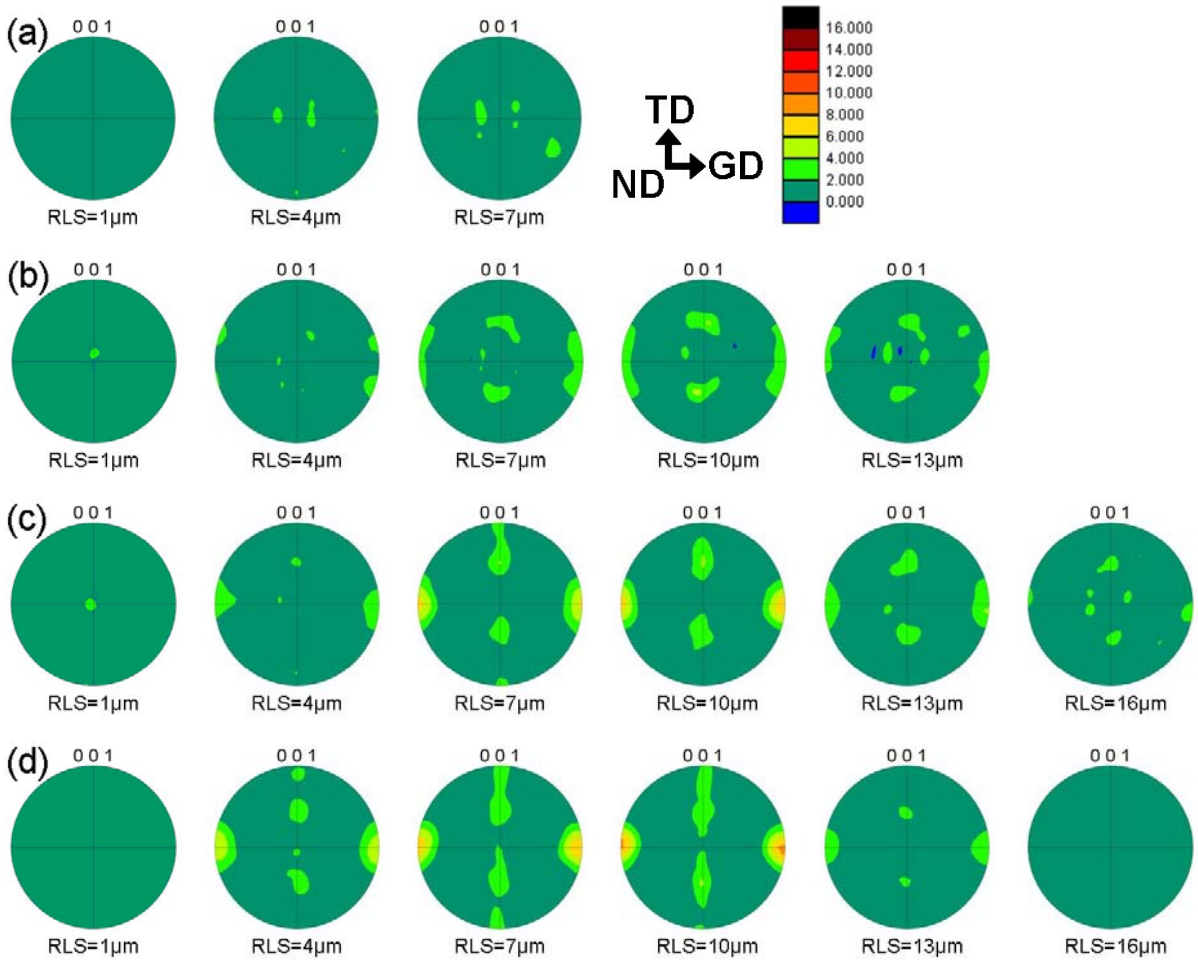

Figure 55. ND pole figures of Cu100 at RLS=1 μm to 16 μm: (a) E/E_{CM}=1.2, (b) E/E_{CM}=1.7, (c) E/E_{CM}=2.3 and (d) E/E_{CM}=3.0.

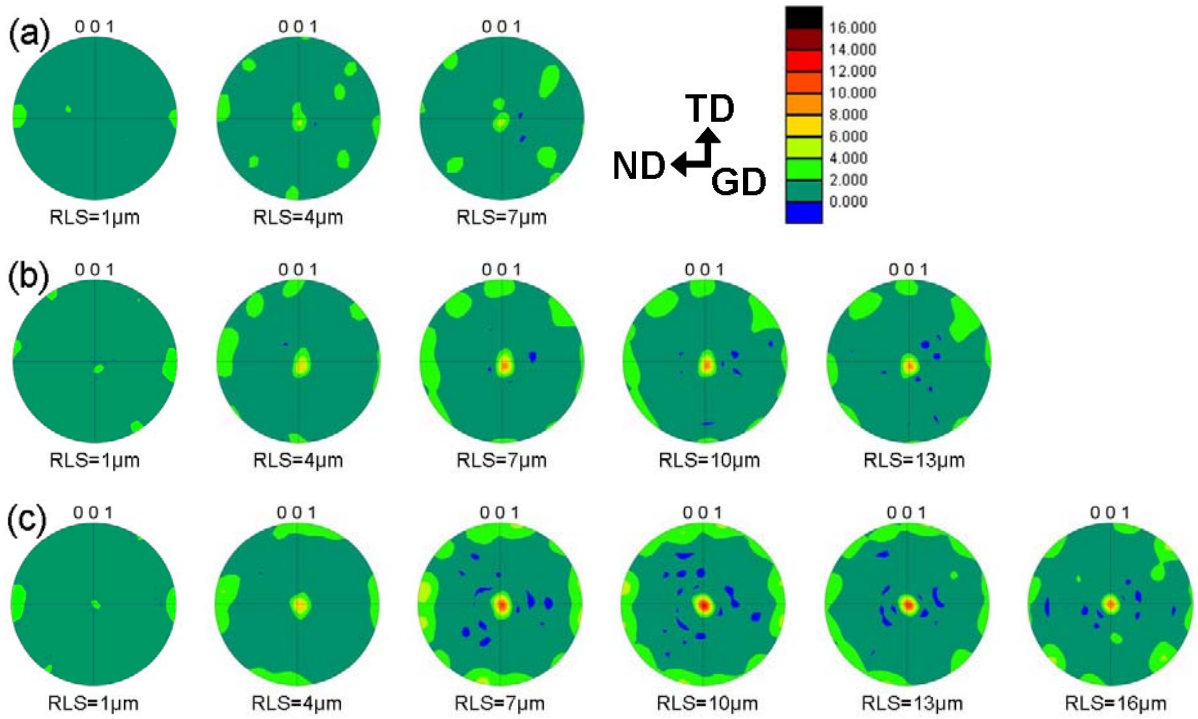

Figure 56. GD pole figures of Cu200 at RLS=1 μm to 16 μm: (a) E/E_{CM}=1.2, (b) E/E_{CM}=1.7 and (c) E/E_{CM}=2.3.

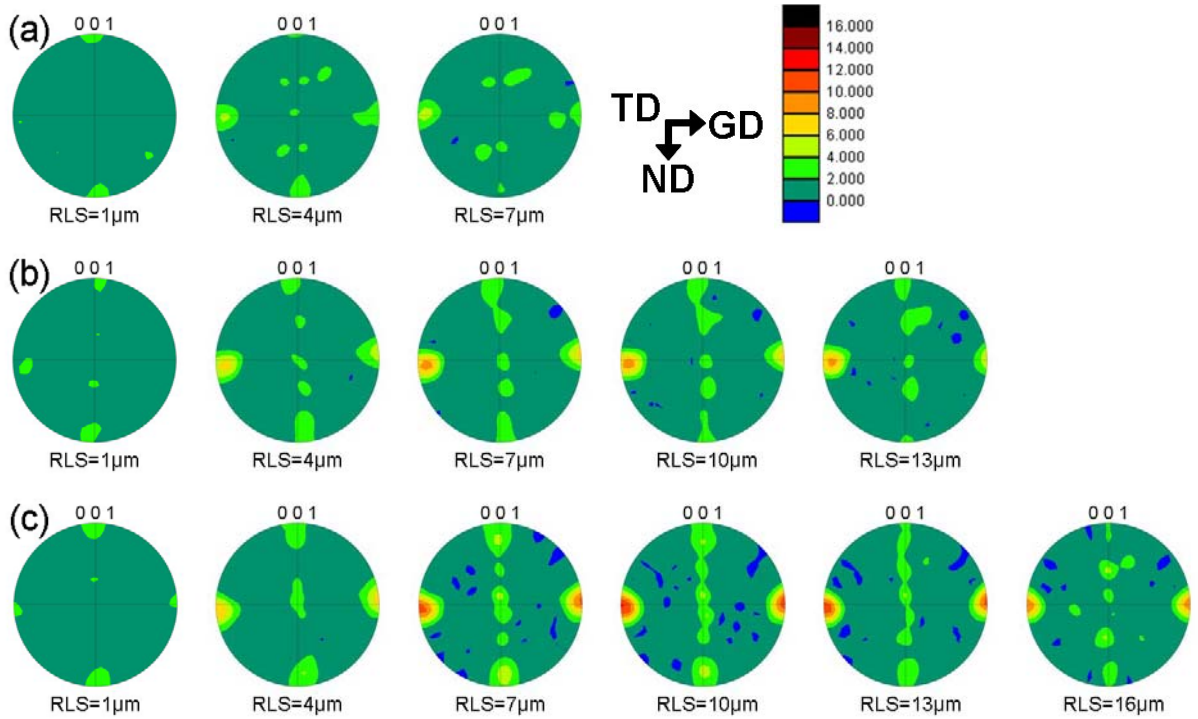

Figure 57. TD pole figures of Cu200 at RLS=1 μm to 16 μm: (a) E/E_{CM}=1.2, (b) E/E_{CM}=1.7 and (c) E/E_{CM}=2.3.

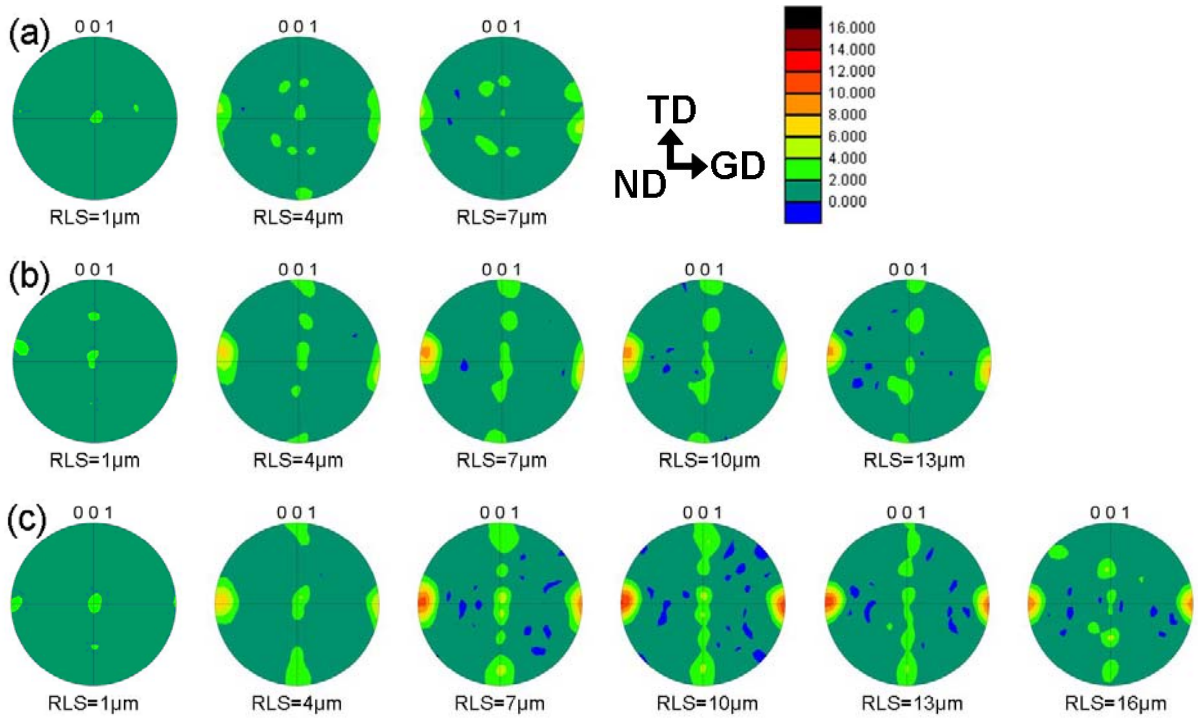

Figure 58. ND pole figures of Cu200 at RLS=1 μm to 16 μm: (a) E/E_{CM}=1.2, (b) E/E_{CM}=1.7 and (c) E/E_{CM}=2.3.

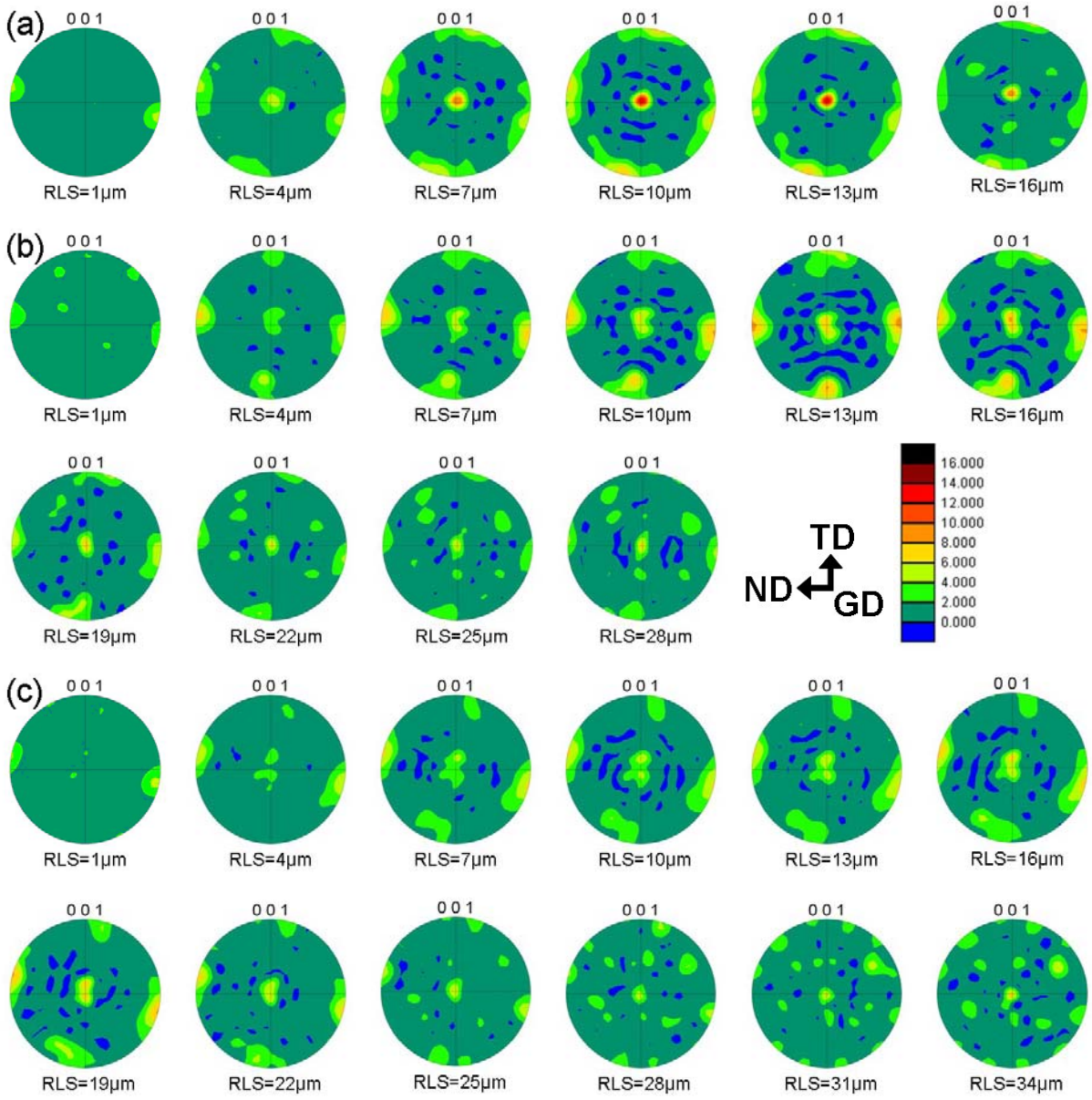

Figure 59. GD pole figures of Cu500 at RLS=1 μm to 34 μm: (a) E/E_{CM}=1.2, (b) E/E_{CM}=1.7 and (c) E/E_{CM}=2.3.

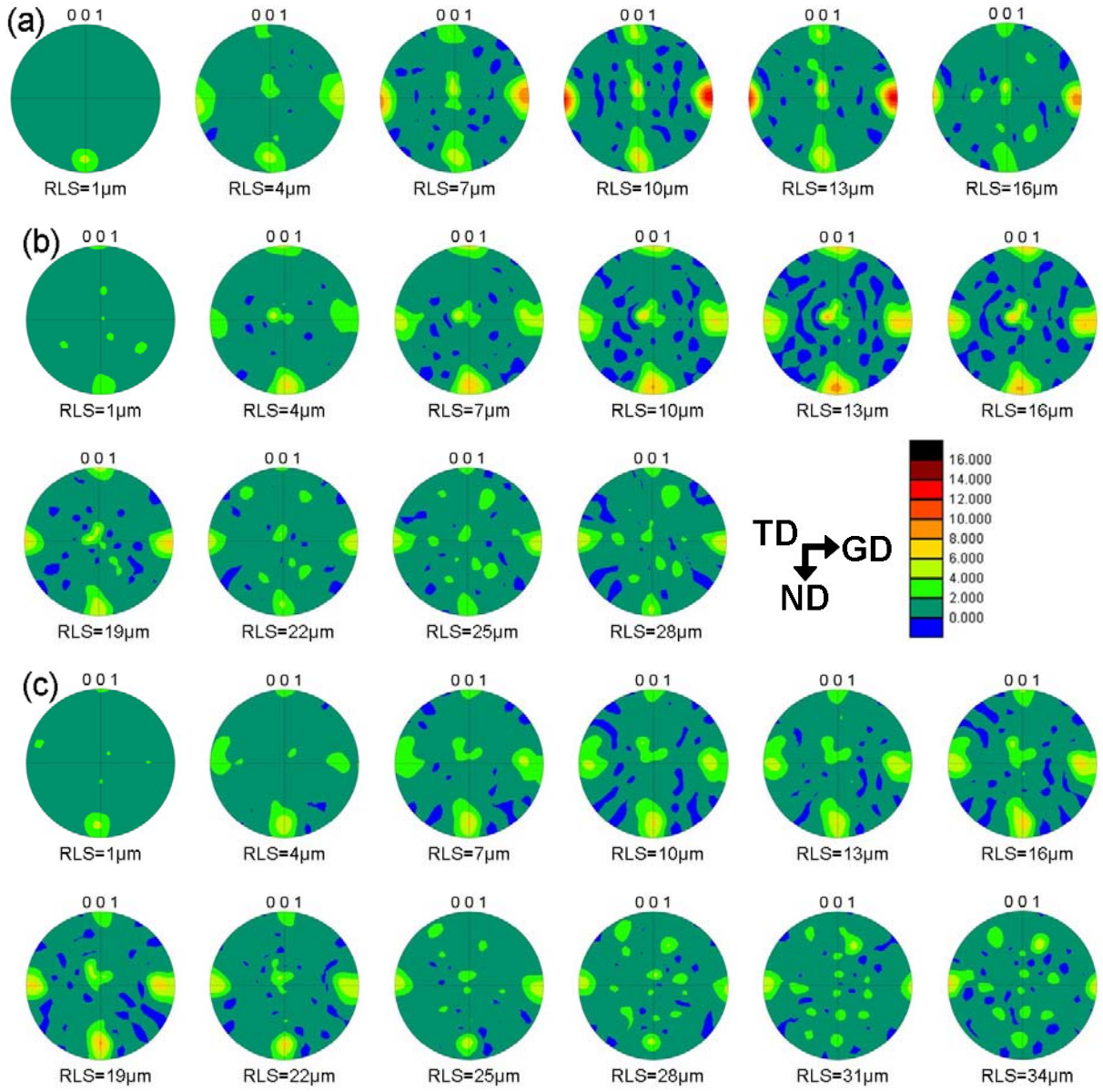

Figure 60. TD pole figures of Cu500 at RLS=1 μm to 34 μm: (a) E/E_{CM}=1.2, (b) E/E_{CM}=1.7 and (c) E/E_{CM}=2.3.

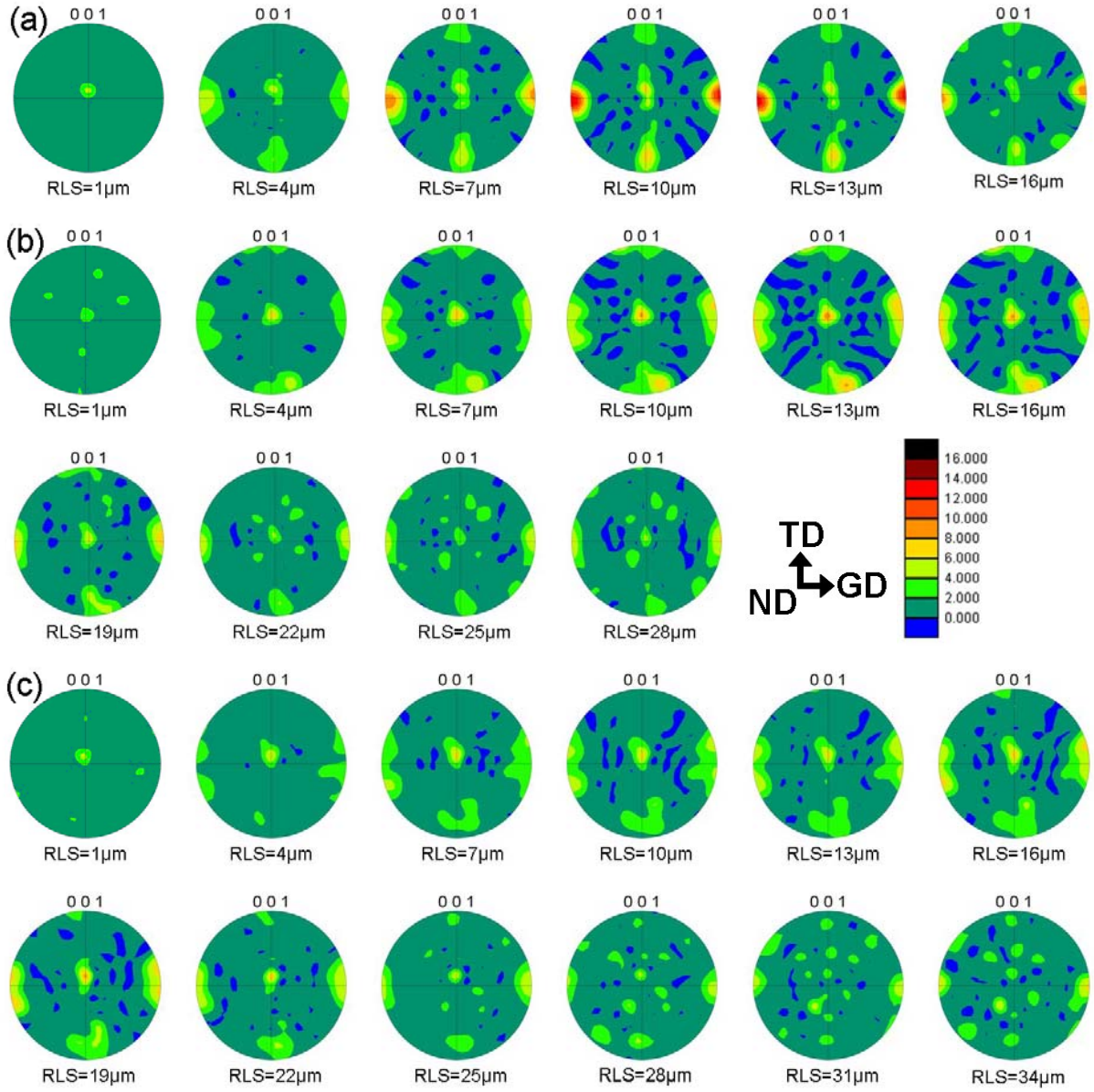

Figure 61. ND pole figures of Cu500 at RLS=1 μm to 34 μm: (a) E/E_{CM}=1.2, (b) E/E_{CM}=1.7 and (c) E/E_{CM}=2.3.

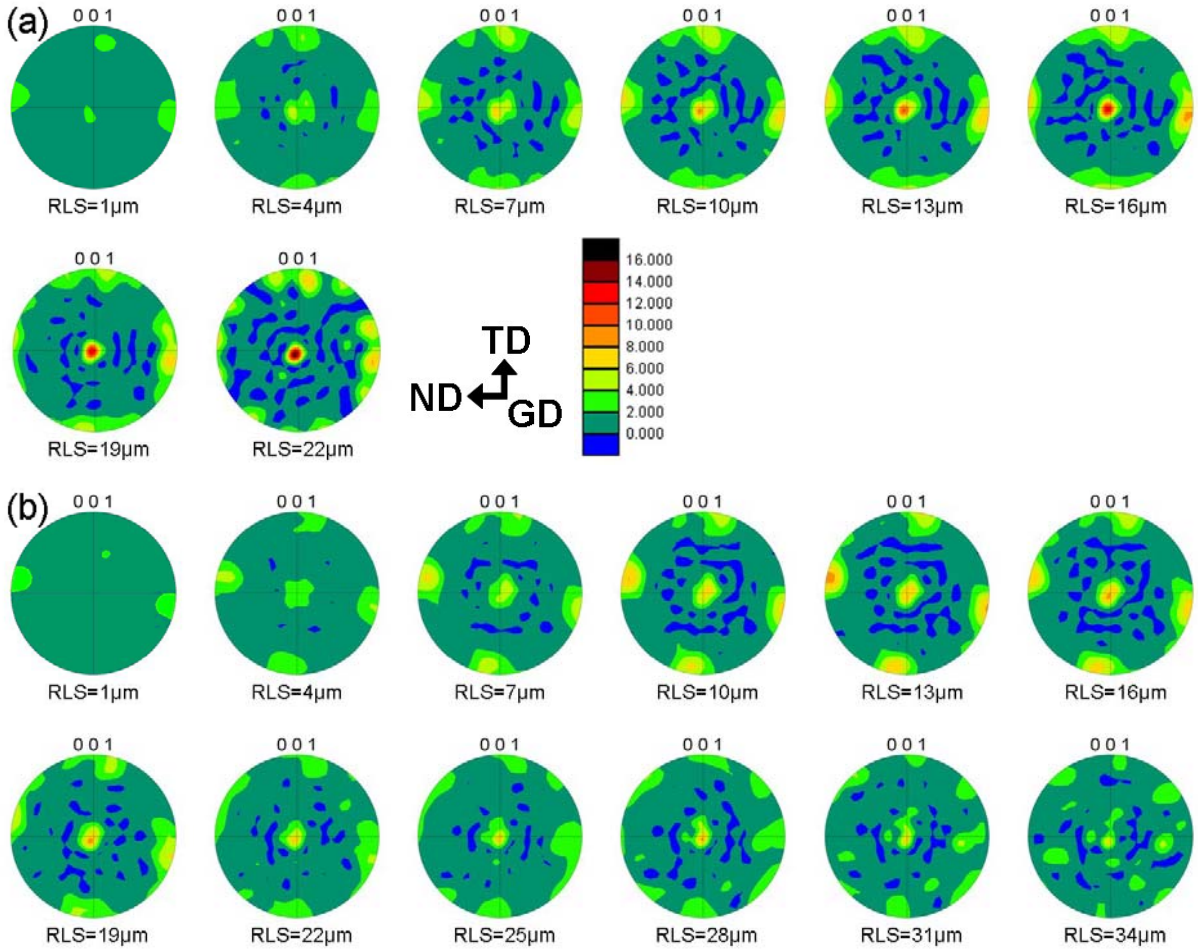

Figure 62. GD pole figures of Cu1000 at RLS=1 μm to 34 μm: (a) E/E_{CM}=1.2 and (b) E/E_{CM}=1.7.

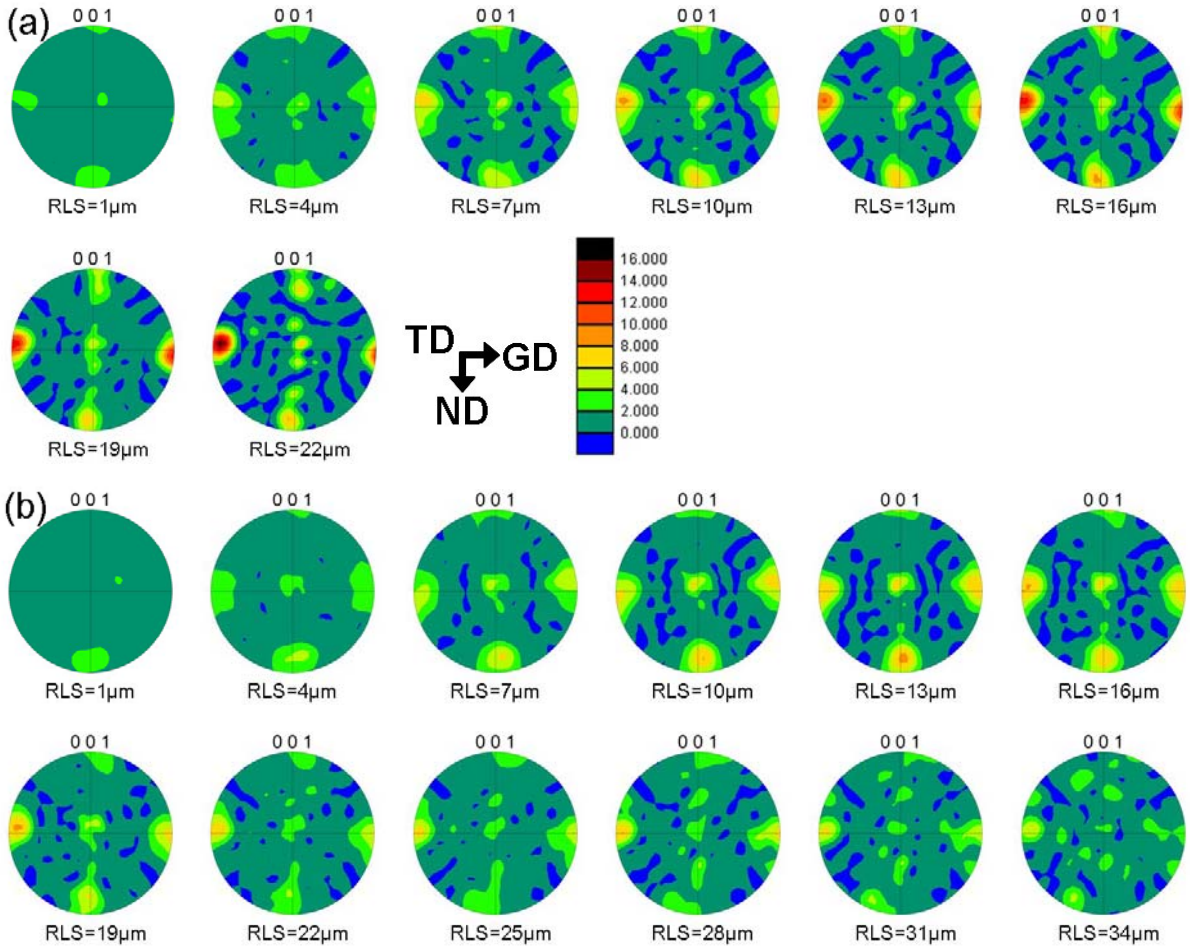

Figure 63. TD pole figures of Cu1000 at RLS=1 μm to 34 μm: (a) E/E_{CM}=1.2 and (b) E/E_{CM}=1.7.

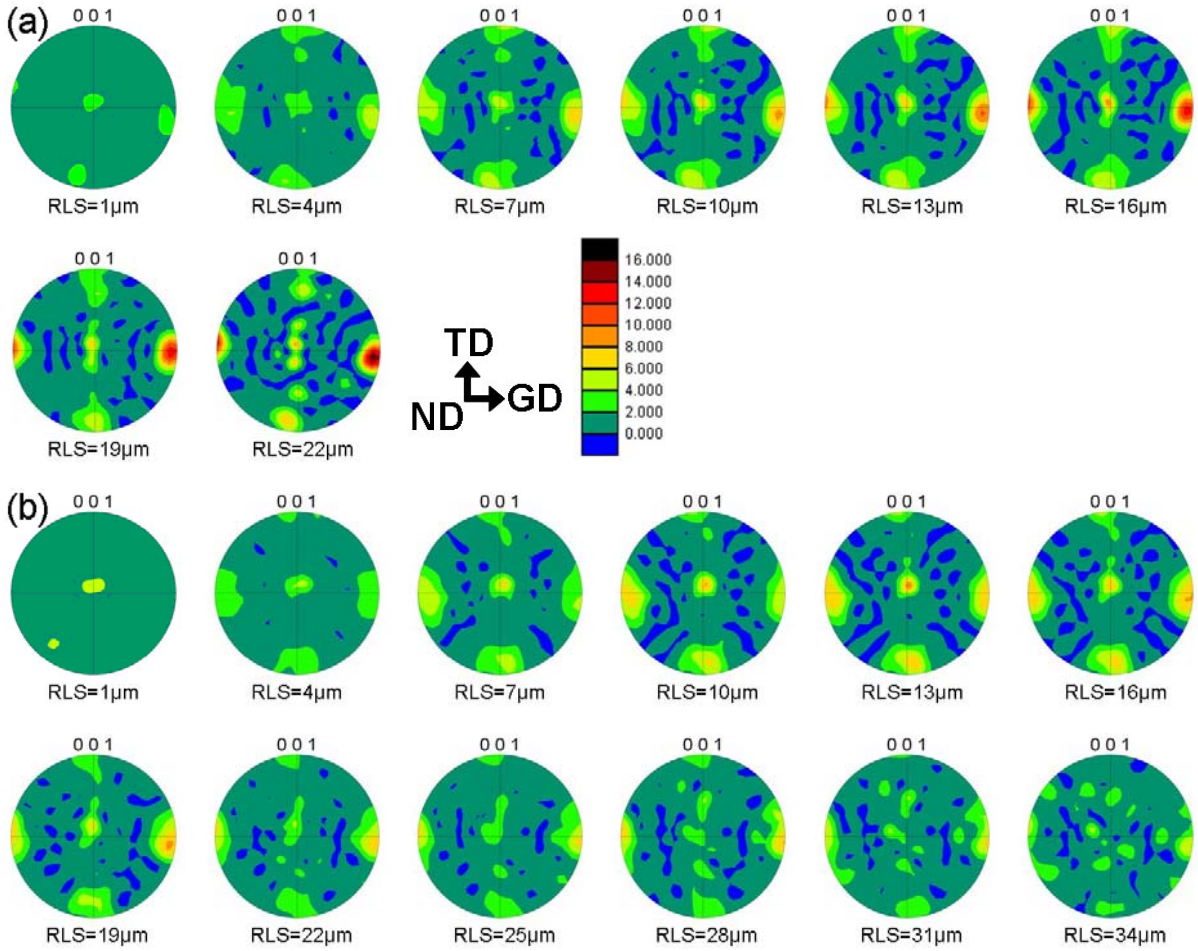

Figure 64. ND pole figures of Cu1000 at RLS=1 μm to 34 μm: (a) E/E_{CM}=1.2 and (b) E/E_{CM}=1.7.

5.1.3 Texture Formation in Ag Film

The texture data in Ag100 and Ag200 was collected and analyzed by EBSD in the same way as the Cu films.

In Figure 65 the microstructure of the scanned area is shown in the Ag200 film, together with the OIM in GD, TD and ND. The distortion in the images is induced by the imperfect geometric alignment, wand the orientation has been corrected by the standard Si wafer and therefore is not affected by this distortion. The silver textures in all of GD, TD and ND are found to be different than is the copper film. Here the favored GD is changed from <100> to approximately <114>. Also, the TD and ND are both very close to <221> and <104>.

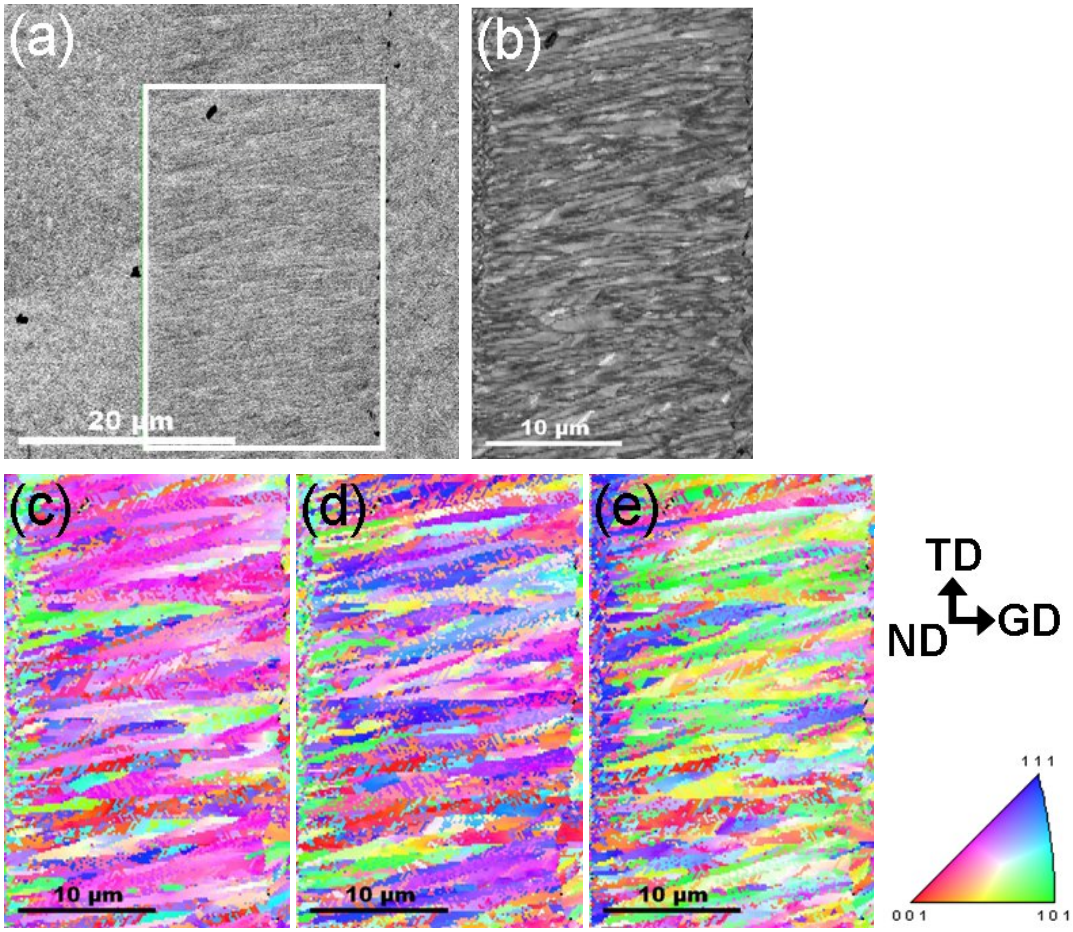

Figure 65. Example of EBSD dataset collected from RLS microstructure for Ag200 with E/E_{CM}=2.3. (a) Plan view image, (b) IQ image, (c) Orientation map along film growth direction (GD), (d) Orientation map along transverse direction (TD) and (e) Orientation map along normal direction (ND).

As with the copper films, OIM data of Ag100 and Ag200 were randomly collected from 6 columnar (1 μm width and 35 μm length) at the denoted RLS distance, i.e. 1 μm to 22 μm. The examples of microstructure, IQ, OIM in GD, TD and ND are generated as shown in Figure 66, where the analyzed grains are more than 200.

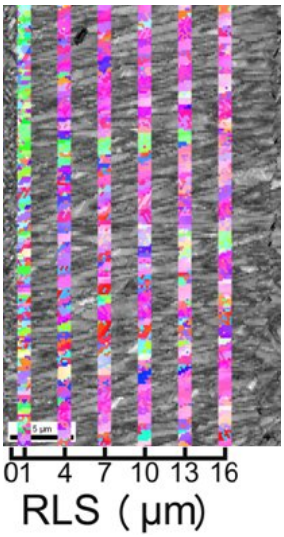

Figure 66. OIM data of silver films are collected at the denoted RLS distance, where each picked area is 1 μm wide and 35 μm long.

100 pole figures from 1 μm to 22 μm are generated in each RLS distance. The GD, TD and ND pole figures of Ag100 and Ag200 are shown in Figure 67 to Figure 72.

As seen in the pole figures, the formed texture in Ag films is different than is Cu films. This favored growth orientation was determined to be <114> in GD. And in TD the texture changed from <221> to <104> as the RLS distance increased.

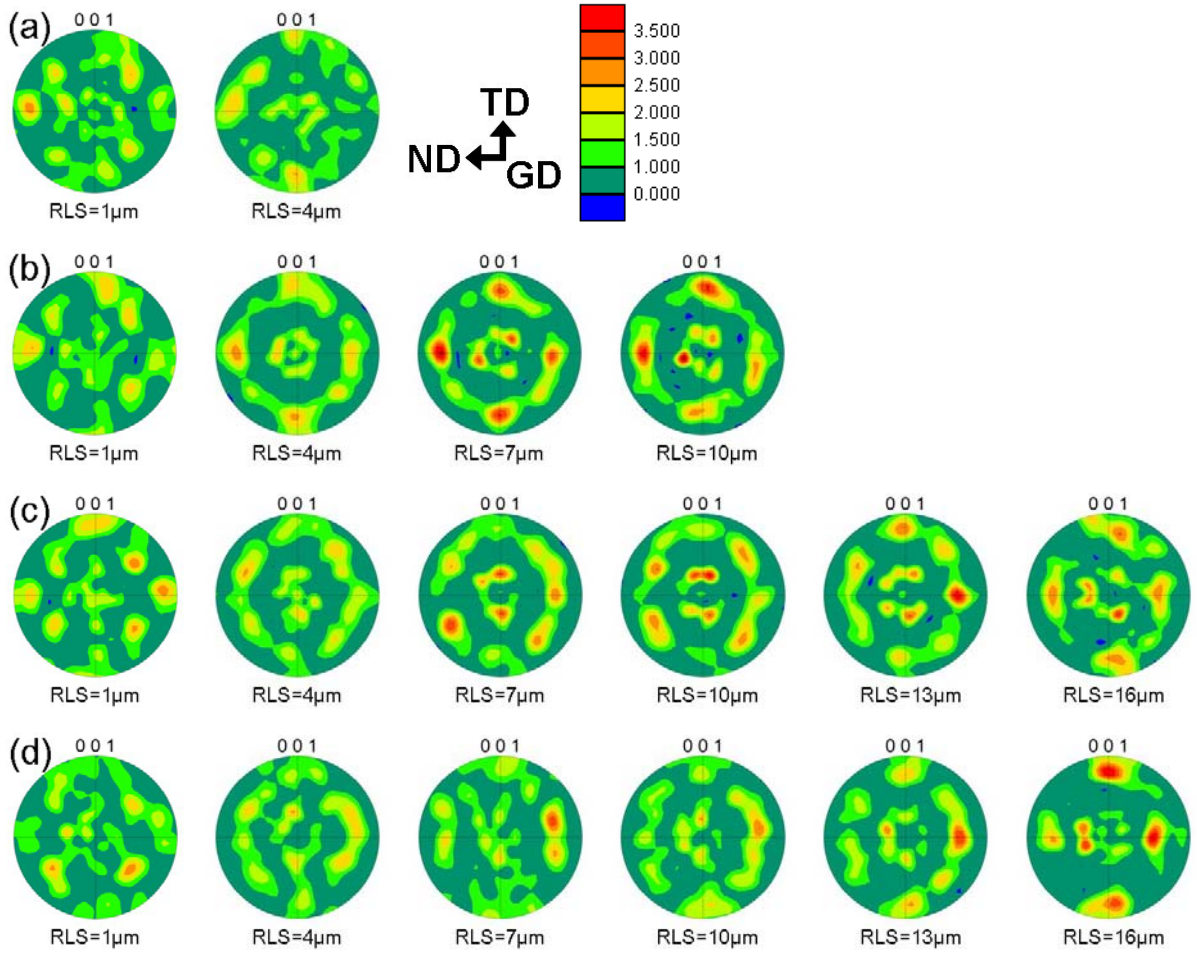

Figure 67. GD pole figures of Ag100 at RLS=1 μm to 16 μm: (a) E/E_{CM}=1.2, (b) E/E_{CM}=1.7, (c) E/E_{CM}=2.3 and (d) E/E_{CM}=3.0.

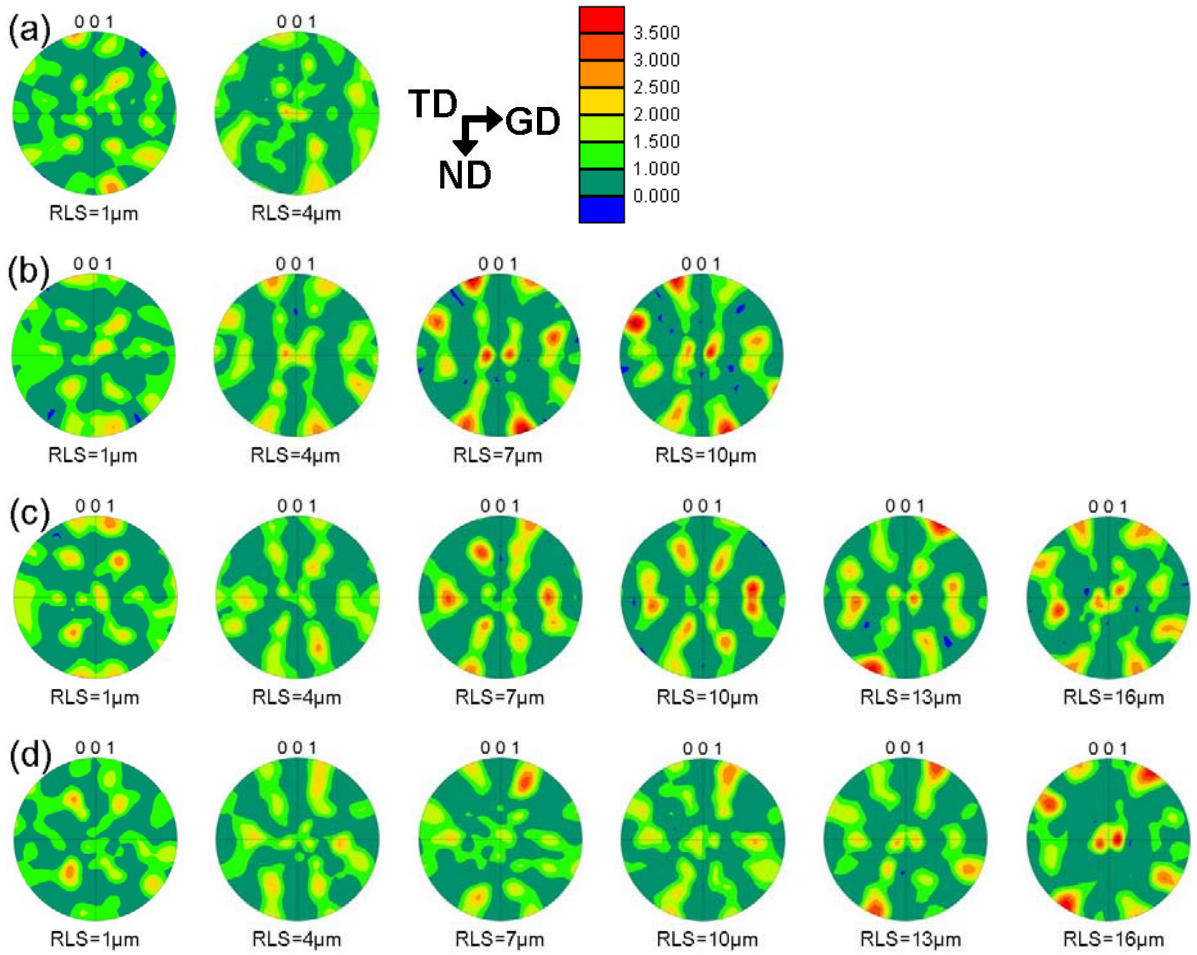

Figure 68. TD pole figures of Ag100 at RLS=1 μm to 16 μm: (a) E/E_{CM}=1.2, (b) E/E_{CM}=1.7, (c) E/E_{CM}=2.3 and (d) E/E_{CM}=3.0.

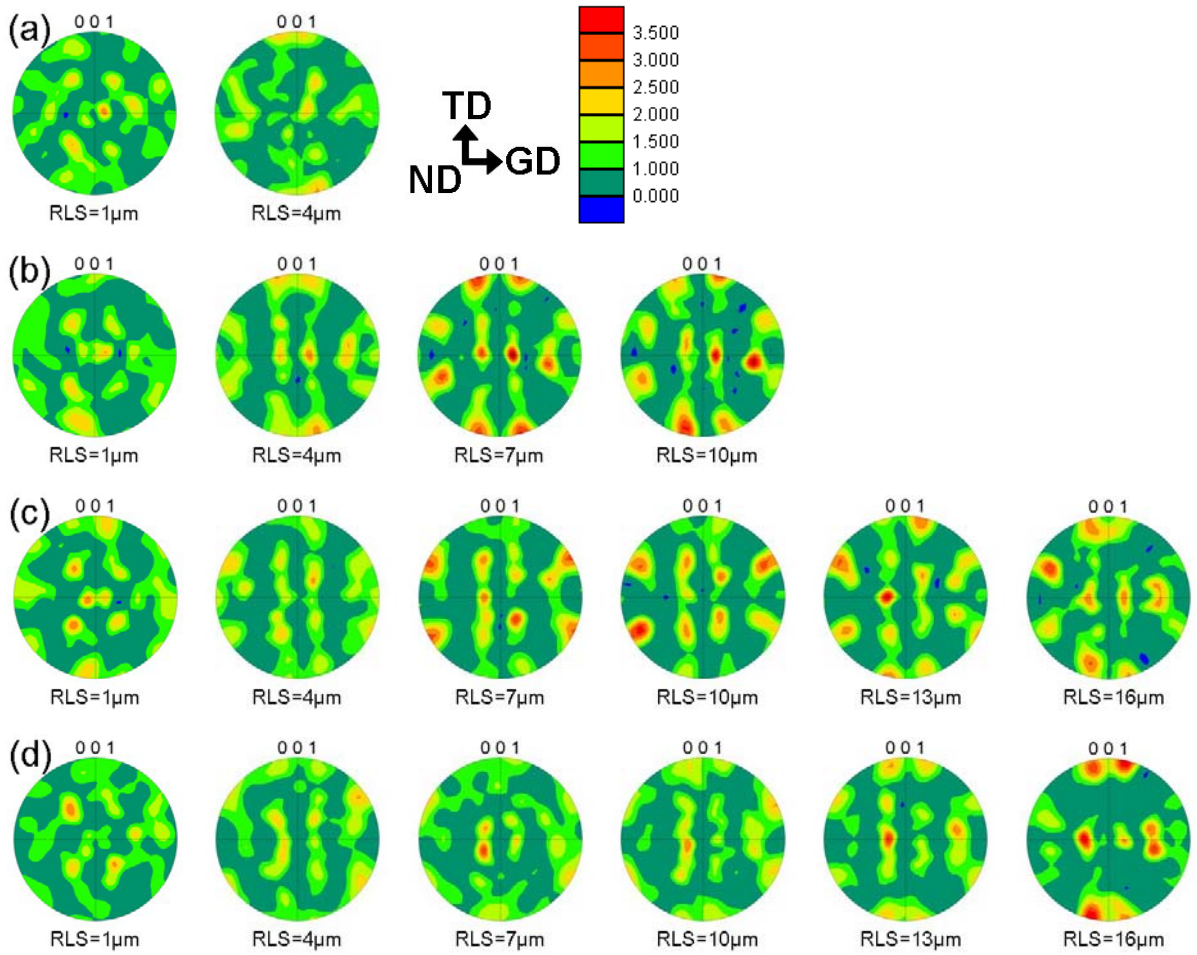

Figure 69. ND pole figures of Ag100 at RLS=1 μm to 16 μm: (a) E/E_{CM}=1.2, (b) E/E_{CM}=1.7, (c) E/E_{CM}=2.3 and (d) E/E_{CM}=3.0.

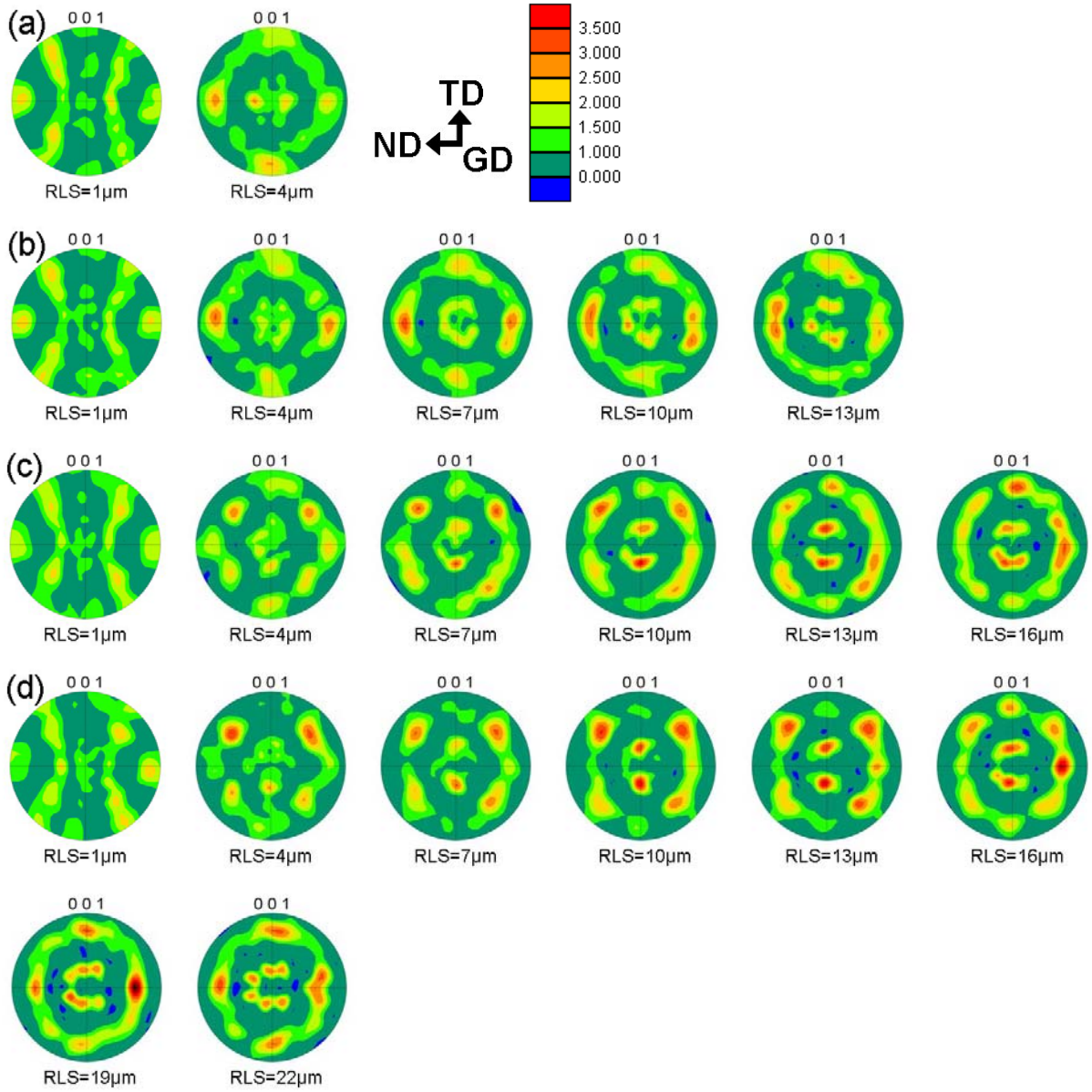

Figure 70. GD pole figures of Ag200 at RLS=1 μm to 22 μm: (a) E/E_{CM}=1.2, (b) E/E_{CM}=1.7, (c) E/E_{CM}=2.3 and (d) E/E_{CM}=3.0.

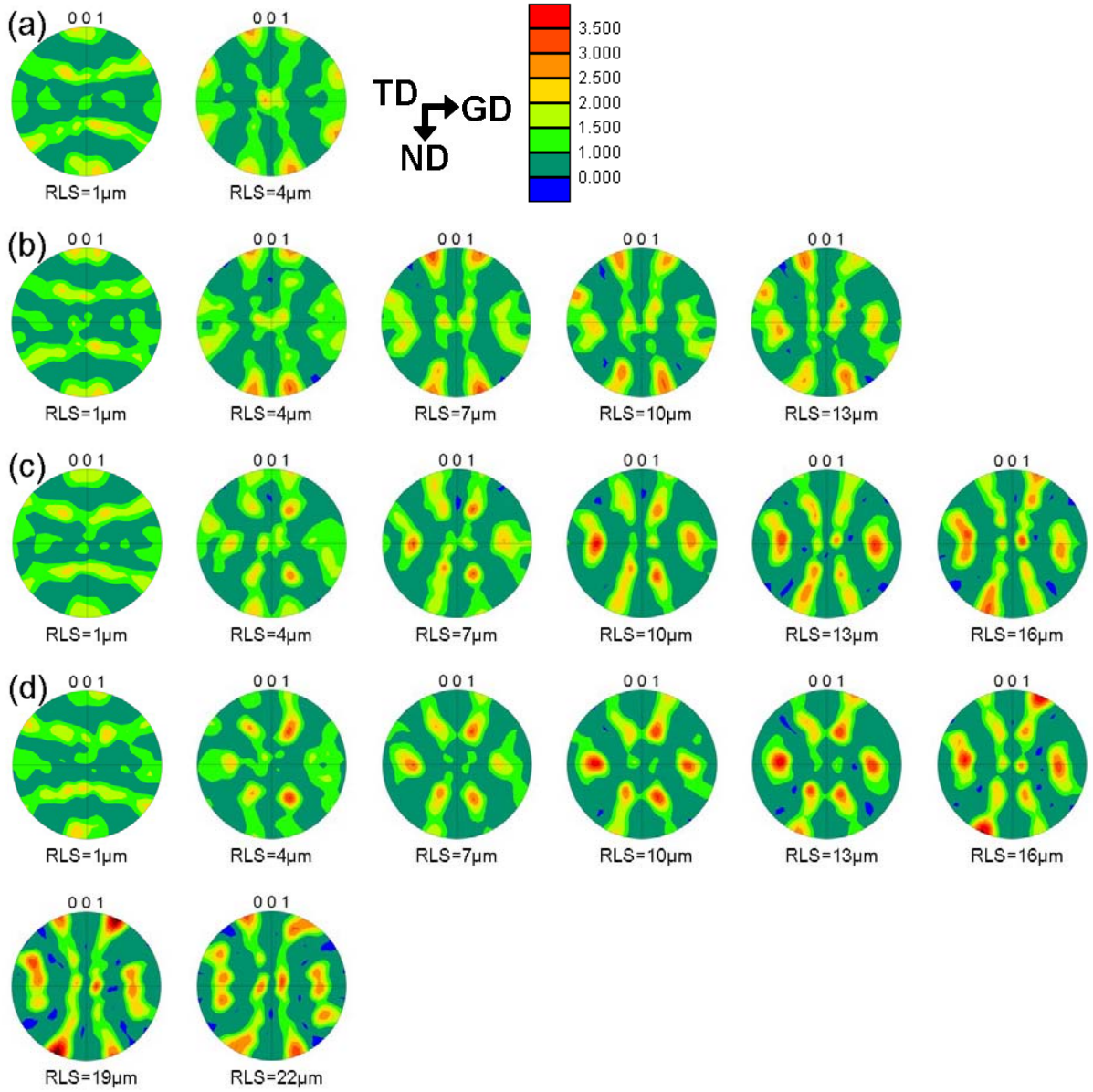

Figure 71. TD pole figures of Ag200 at RLS=1 μm to 22 μm: (a) E/E_{CM}=1.2, (b) E/E_{CM}=1.7, (c) E/E_{CM}=2.3 and (d) E/E_{CM}=3.0.

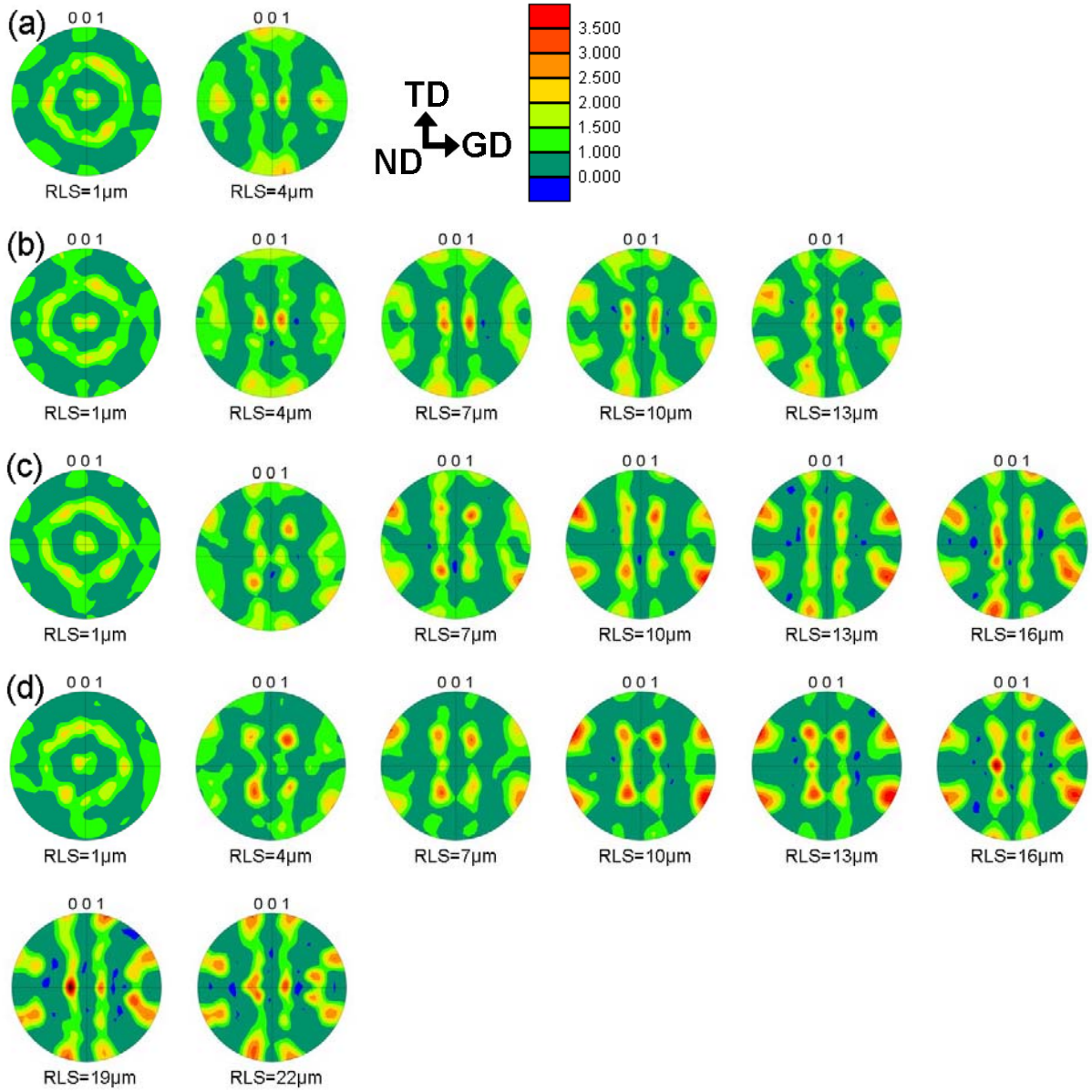

Figure 72. ND pole figures of Ag200 at RLS=1 μm to 22 μm: (a) E/E_{CM}=1.2, (b) E/E_{CM}=1.7, (c) E/E_{CM}=2.3 and (d) E/E_{CM}=3.0.

5.1.4 Texture Formation in Au Film

The texture data in Au200 were collected and analyzed by EBSD in the same way of Cu and Ag films.

Figure 73 shows the microstructure of the scanned area in the Au200 film, and the OIM in GD, TD and ND. The gold textures in both of GD and ND are similar with that found in the copper film. Here <100> is very strong in GD, TD and ND. Bubbles and wrinkles were easily formed in the gold film; this caused problems in analysis of the gold film with SEM and TEM.

Using the same method as for copper and silver films, OIM data of Au200 were randomly collected from 6 columnar (1 μm width and 35 μm length) at the denoted RLS distance, i.e., 1 μm to 10 μm (Figure 74). All the GD, TD and ND pole figures are shown in Figure 75 to Figure 77.

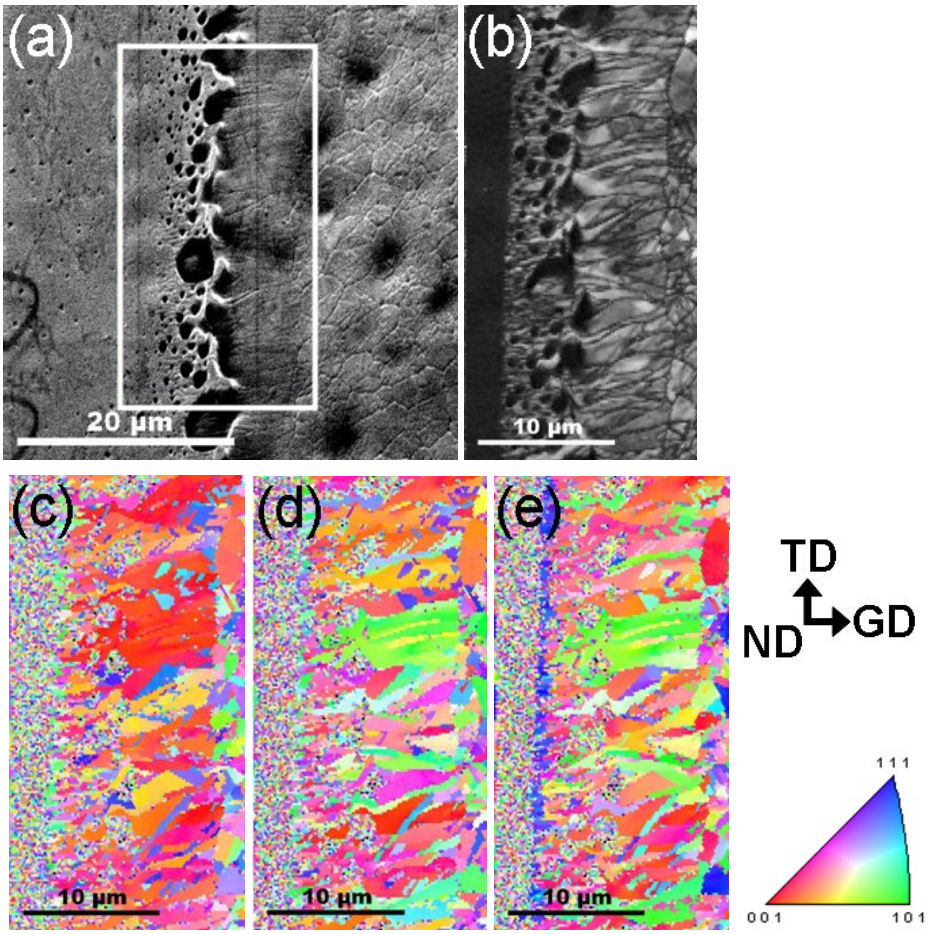

Figure 73. Example of EBSD dataset collected from RLS microstructure for Au200 with E/E_{CM}=2.3. (a) Plan view image, (b) IQ image, (c) Orientation map along film growth direction (GD), (d) Orientation map along transverse direction (TD) and (e) Orientation map along normal direction (ND).

Shown in the <100> pole figures of each condition of Au200 where the energy ratio was 1.2, 1.7 or 2.3, <100> is the favored growth orientation in RLS. The <100> texture is very weak at 1 μm RLS distance, and increases with RLS distance reaching a peak in the end of RLS. This trend suggests no zone III in Au200.

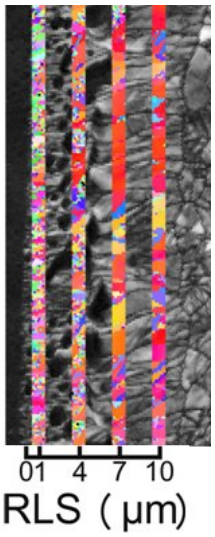

Figure 74. OIM data of gold films are collected at the denoted RLS distance, where each picked area is 1 μm wide and 35 μm long.

Comparing the pole figures of Au200 with the different energy ratio at the same RLS distance (shown in Figure 75), the <100> texture in GD gets stronger with the increasing laser energy ratio. This trend is similar with that found in Cu100 and Cu200.

5.1.5 Simulation Result of S-L Interface

In order to figure out the mechanism for texture formation during RLS, the S-L interface has been determined of temperature profile, velocity and temperature gradient by simulation.

As shown in Figure 78(a), the temperature profile in the cross section is calculated by 3DNS simulation, where the S-L interface moves from left to right, i.e. from solid to liquid. The temperature is the highest in Cu film and decreases a lot in both silica layers. Figure 78(b) shows the liquid temperature profile in the cross section at different time after the laser processing. Obviously the temperature of liquid decreases very quick after the laser processing. From both Figure 78(a) and (b), simulations suggest that

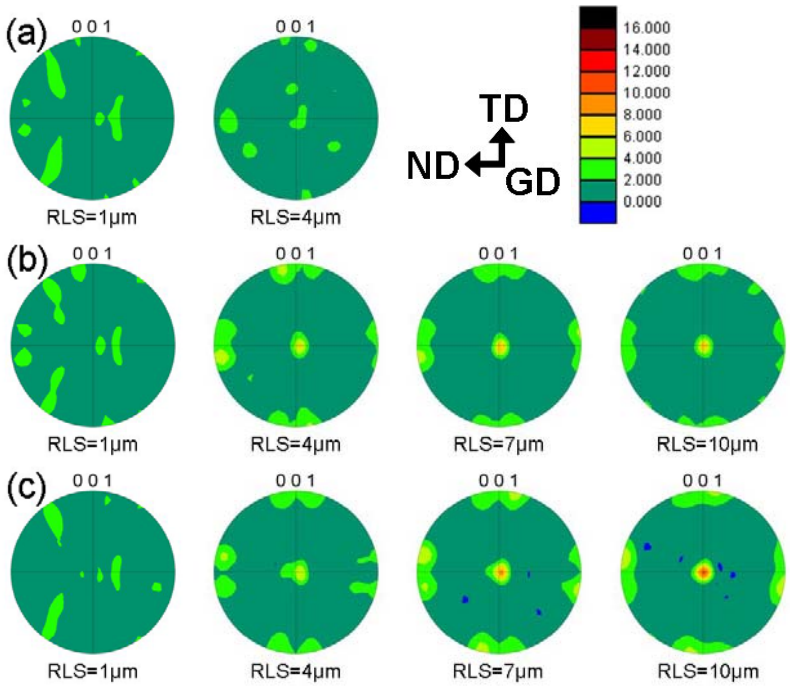

Figure 75. GD pole figures of Au200 at RLS=1 μm to 10 μm: (a) E/E_{CM}=1.2, (b) E/E_{CM}=1.7, (c) E/E_{CM}=2.3 and (d) E/E_{CM}=3.0.

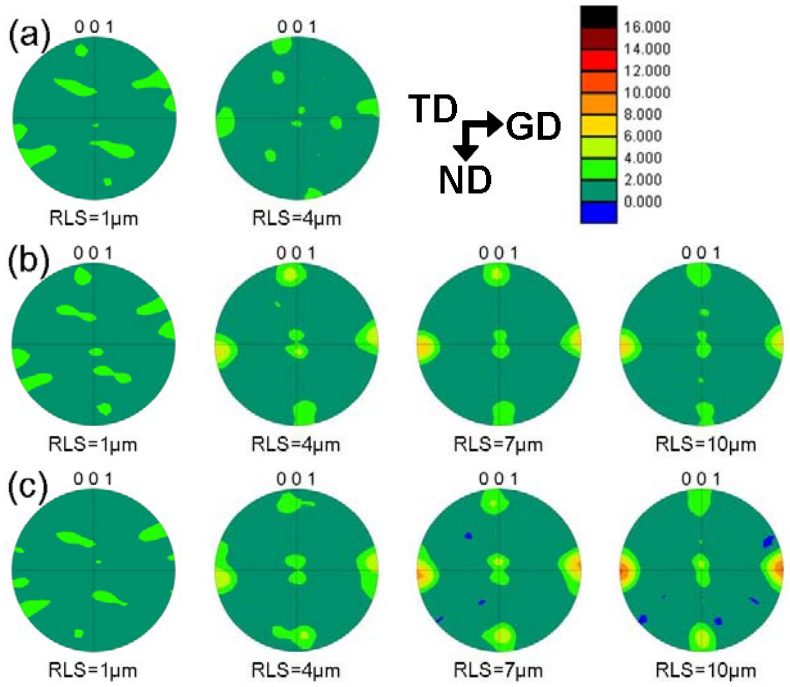

Figure 76. TD pole figures of Au200 at RLS=1 μm to 10 μm: (a) E/E_{CM}=1.2, (b) E/E_{CM}=1.7, (c) E/E_{CM}=2.3 and (d) E/E_{CM}=3.0.

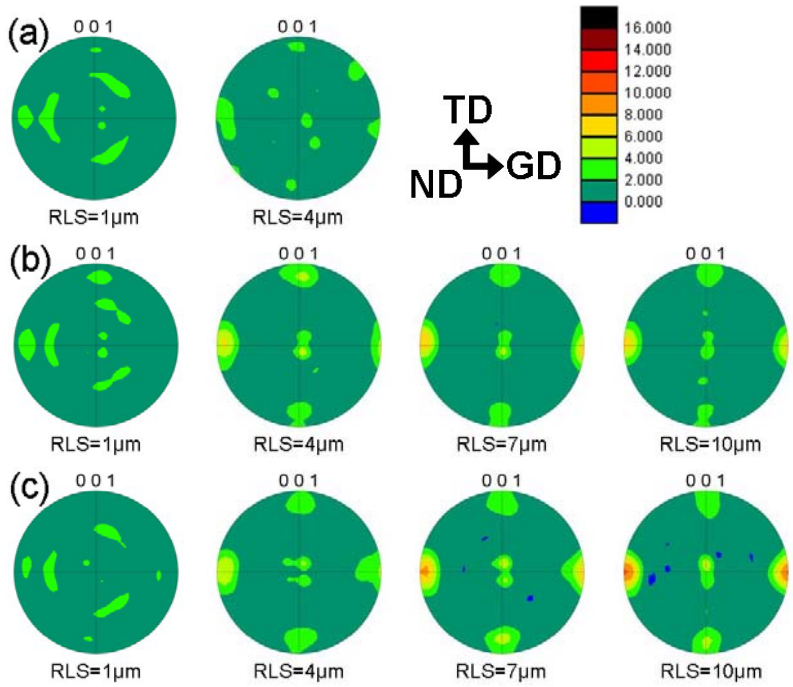

Figure 77. ND pole figures of Au200 at RLS=1 μm to 10 μm: (a) E/E_{CM}=1.2, (b) E/E_{CM}=1.7, (c) E/E_{CM}=2.3 and (d) E/E_{CM}=3.0.

the heat flux is mainly conducted rapidly from the metal film to the substrate where the temperature is much lower than the metal film. Therefore, the heat is transferred perpendicularly to the S-L interface in micrometer scale.

However, the temperature profile in GD (shown in Figure 78(c)) suggests that the temperature is highest in the S-L interface and decreases rapidly in both solid and liquid side. Although the S-L interface temperature is decreasing during RLS, it is always the temperature peak and therefore the latent heat generated in S-L interface is conducted to both solid and liquid sides. As a result, the local heat flux is still parallel with GD in nanometer scale. In addition, the temperature gradient in solid side is steeper at the first 100 ns than what in liquid side. Then, the temperature gradient in the liquid side becomes steeper as RLS going on. This induces the interface instability where dendritic growth will amplify the anisotropy during RLS.

The S-L interface temperature and velocity can be adjusted by changing the input energy or by adopting different film thickness. As shown in Figure 79, the interface temperature increases with the increasing energy ratio, and the interface velocity decreases with the increasing energy ratio. Therefore, RLS is slow down by putting more energy and by decreasing the quenching rate.

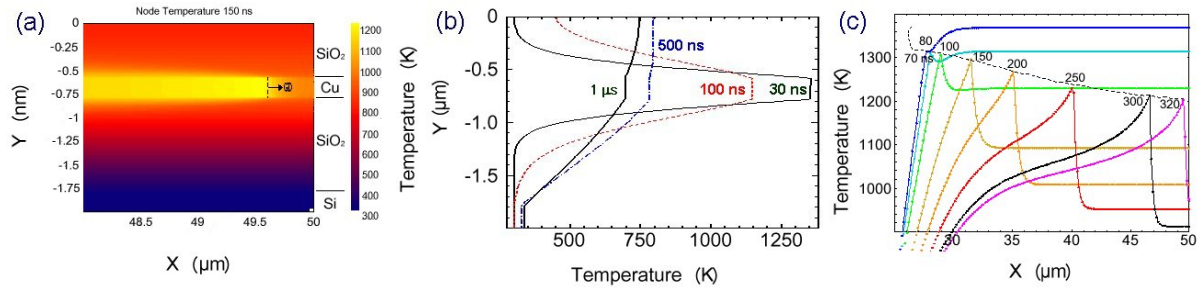

Figure 78. 3DNS simulation for Cu 200 film: (a) Temperature field calculated for RLS of Cu thin film, (b) liquid temperature profile in the cross section at the different time after laser processing, (c) the temperature profile in GD at different time after laser processing.

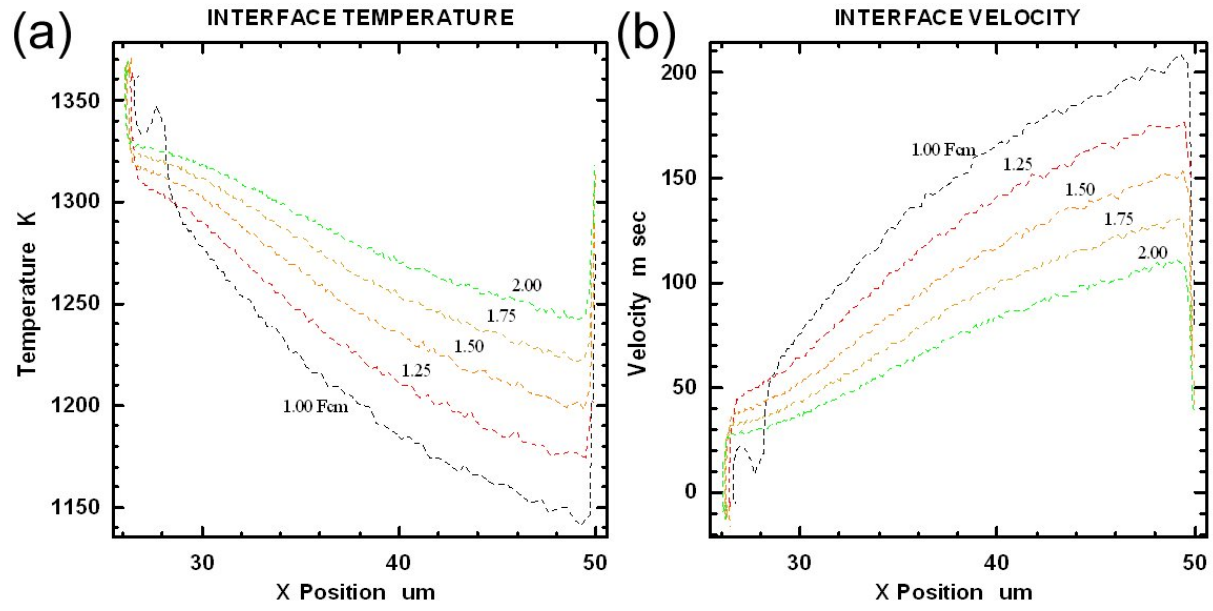

Figure 79. 3DNS simulation for Cu 200 film at different energy ratio: (a) S-L interface temperature versus x position far away from the edge of RLS region; (b) S-L interface velocity versus x position far away from the edge of RLS region.

Simulation results of S-L interface temperature and velocity with different thickness are shown in Figure 80. The interface temperature increases with the increasing thickness, and the interface velocity decreases with the increasing thickness. As a result, RLS is slow down in thick films.

Thus, it is suggested that RLS is thermodynamically favored in thick film or when being treated by high energy, and kinetically favored in thin film or when being treated by low energy.

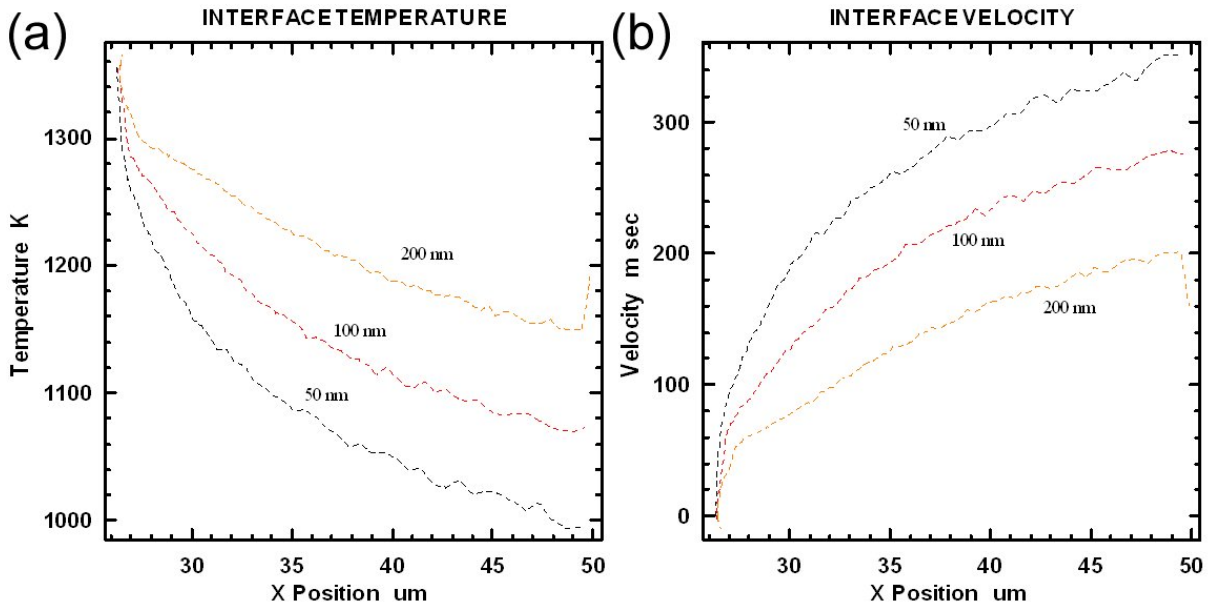

Figure 80. 3DNS simulation for Cu film with different thickness: (a) S-L interface temperature versus x position far away from the edge of RLS region; (b) S-L interface velocity versus x position far away from the edge of RLS region.

5.1.6 Discussion of Texture Formation

5.1.6.1 The Texture Formation Process with the Changed RLS Distance

Shown in the pole figures in Figure 53 to Figure 64, in each condition of the copper films where the energy ratio is set up to be about 1.2, 1.7, 2.3 or 3.0 and the metal thickness is 100 nm, 200 nm, 500 nm or 1000 nm, the <100> texture is very weak at 1 μm RLS distance, and increases with the RLS distance. It is obvious that <100> is the favored growth orientation during RLS under these conditions. A small decrease in the texture intensity in the end of RLS suggests that the texture formation process breaks down in zone III. This is likely due to impurities and dislocations.

To show this texture formation process, the Cu100 treated with the energy ratio of 3.0 is a very clear example and is analyzed in Figure 81, where the texture increases in zone I, and reaches the peak (RLS=10 μm) in the middle of zone II, and finally goes back to random in zone III.

Similar trends have been found in both Ag and Au films, shown in Figure 82 and Figure 83. During RLS, the texture increases in zone I, and reaches the peak (RLS=10 μm) in zone II. No obvious zone III has been detected by texture formation, which is consistent with the previous conclusion in microstructural determination.

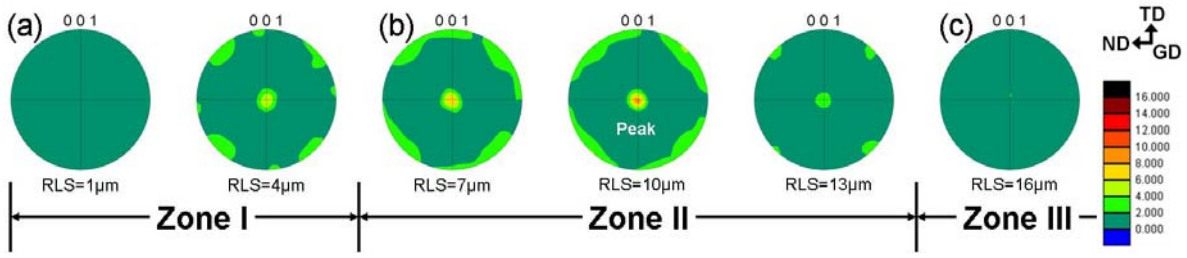

Figure 81. GD pole figures of Cu100 (E/E_{CM}=3.0) at RLS=1 μm to 16 μm, where zone I (a), II (b) and III (c) are figured out to show the texture formation.

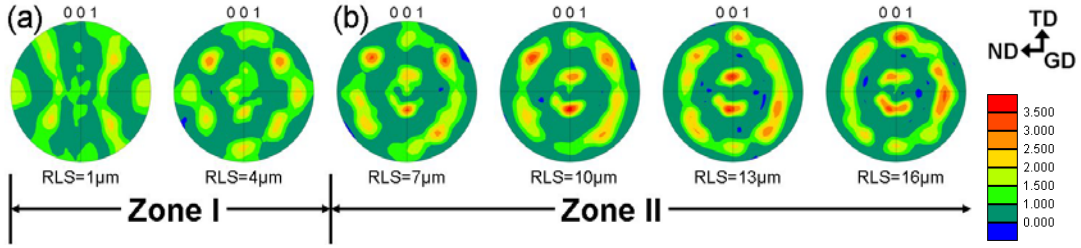

Figure 82. GD pole figures of Ag200 (E/E_{CM}=2.3) at RLS=1 μm to 16 μm, where zone I (a) and II (b) are figured out to show the texture formation.

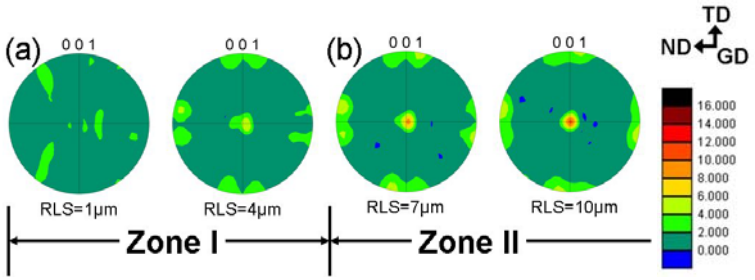

Figure 83. GD pole figures of Au200 (E/E_{CM}=2.3) at RLS=1 μm to 10 μm, where zone I (a) and II (b) are figured out to show the texture formation.

5.1.6.2 The Texture Formation with the Changed Input Energy or Film Thickness

Compared the pole figures of Cu100 and Cu200 with the different energy ratio at the same RLS distance, where RLS=10 μm is picked and shown in Figure 84, the <100> texture in GD gets stronger and stronger with the increasing laser energy ratio and thickness. Because the kinetic effect will be weaker with the higher energy ratio where the quenching rate is decreased, this trend of stronger <100> texture in

the higher laser energy ratio is in the opposite way of kinetic anisotropy. Thus, the texture formation appears to be caused by thermodynamic anisotropy.

However, if compared the pole figures of Cu500 and Cu1000 in the same method shown in Figure 85, the <100> texture in GD gets weaker with the increasing laser energy ratio which follows the principal of kinetic anisotropy but not thermodynamic anisotropy. Also, the texture has been found to increase with the decreasing film thickness, which also follows the kinetic anisotropy.

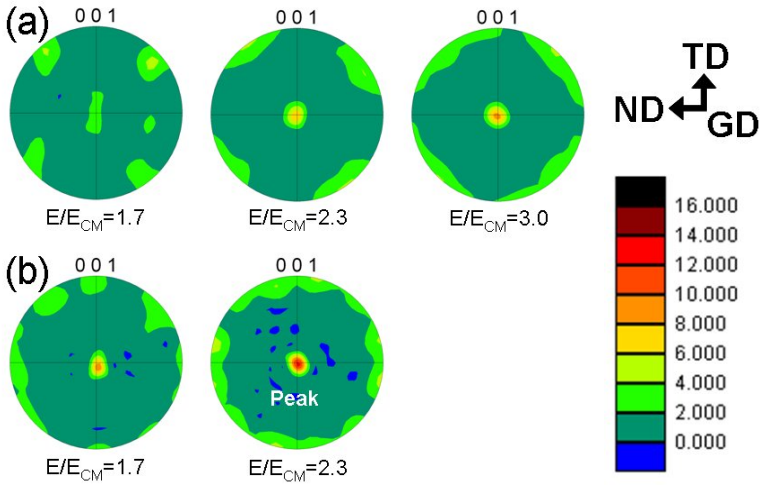

Figure 84. GD pole figures of Cu films with E/E$_{CM}$=1.2, 2.3 and 3.0 at RLS=10 μm: (a) Cu100 and (b) Cu200.

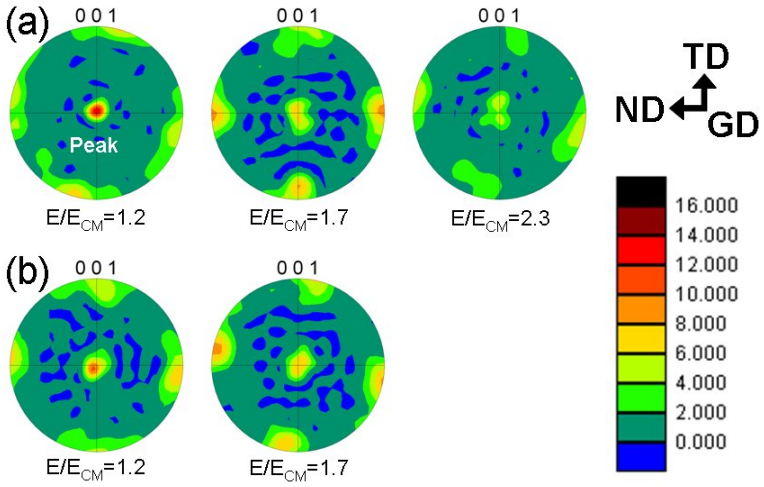

Figure 85. GD pole figures of Cu films with E/E$_{CM}$=1.2, 1.7 and 2.3 at RLS=13 μm: (a) Cu500 and (b) Cu1000.

The texture formation trend in Cu films is summarized in Figure 86, where the texture intensity is compared to the input laser energy ratio.

There are two hypothesis that can explain this disagreement:

1) Texture formation is generated by thermodynamic anisotropy in Cu films but also amplified by dendritic growth.

Although the film thickness is different, the texture formation in a metal film is assumed to be always induced by one anisotropic: kinetic or thermodynamic anisotropy. However, by 3DNS simulations which have been discussed previously, the temperature gradient in liquid side is greater than what is in solid side. Therefore the thermal dendrite growth amplifies the kinetic or thermodynamic anisotropy during RLS.

The relationship between the texture intensity and the quenching rate (dT/dt) or S-L interface (V_{S-L}) velocity under the effect of thermodynamic anisotropy, kinetic anisotropy and dendritic amplification is shown in Figure 87. The texture intensity decreases with the increasing quenching rate or S-L interface velocity when thermodynamic anisotropy dominates RLS, while the texture intensity increases with the increasing quenching rate or S-L interface velocity when either kinetic anisotropy or dendritic amplification dominates RLS. Therefore, if thermodynamic anisotropy dominates RLS and is amplified by dendritic growth, the texture intensity will reach the pick at the medium quenching rate or S-L interface velocity, where can be called as texture band. If kinetic anisotropy dominates RLS and is amplified by dendritic growth, the texture intensity will still increase with the quenching rate or S-L interface velocity.

Comparing RLS texture formation with Figure 87, Cu100 and Cu200 fall into the right side of the texture band, where the texture intensity increases with the decreasing quenching rate. Cu500 and Cu1000 fall into the left side of the texture band, where the texture intensity increases with the increasing quenching rate.

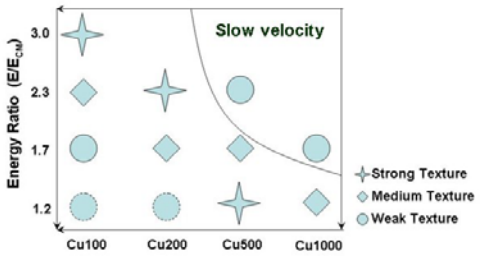

Figure 86. The texture formation ability changes with the input laser energy ratio in different thickness Cu films.

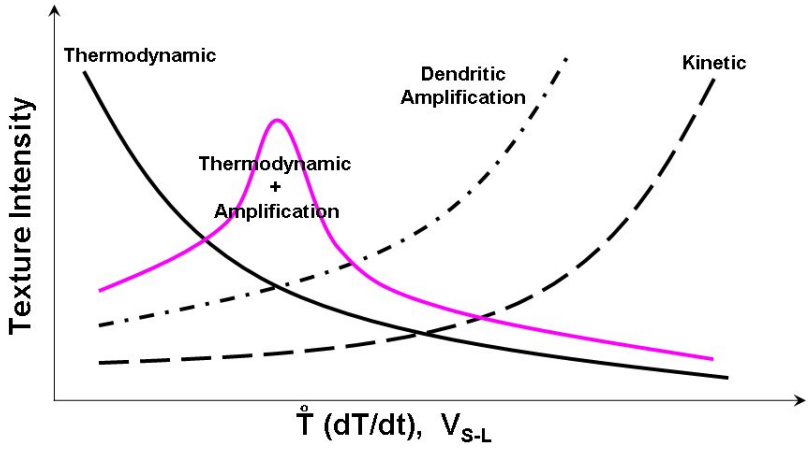

Figure 87. The texture intensity changes with the quenching rate or S-L interface velocity under thermodynamic anisotropy, kinetic anisotropy or dendritic amplification, where thermodynamic anisotropy together with dendritic amplification results a strong texture band in the medium quenching rate or S-L interface velocity.

The previous 3DNS simulations show that the quenching rate and the S-L interface velocity increases with the decreasing of film thickness or the decreasing of energy ratio. If the texture is induced by thermodynamic anisotropy and amplified by dendritic growth, the strong texture band will be formed as shown in Figure 88(a). This is similar with the RLS experimental data, where the strong texture is found in the high energy ratio together with the thin film thickness or in the low energy ratio together with the thick film thickness (shown in Figure 88(b)). Therefore, the texture formed in Cu films is caused by thermodynamic anisotropy but still amplified by dendritic growth at the same time.

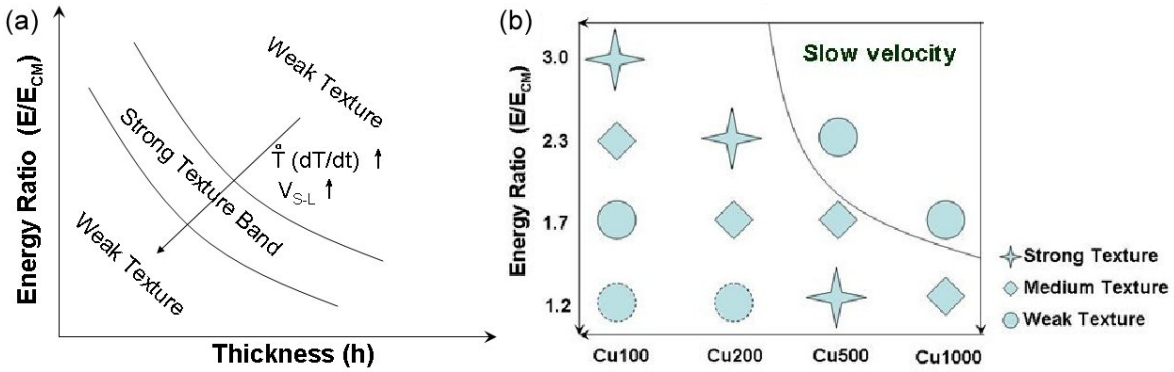

Figure 88. (a) The strong texture band formed by thermodynamic anisotropy and dendritic amplification; (b) the strong texture band formed in RLS experimental data.

2) Texture formation is caused by kinetic anisotropy in thick films but by thermodynamic anisotropy in thin films.

However, this assumption is not consisted with exiting knowledge and hard to experimentally verify. The transition of anisotropic mechanism from kinetic to thermodynamic due to change in solidification velocity is not recommended here to explain our research.

The film thickness can affect RLS by changing the quenching rate. In fact RLS in all of the Cu films is very fast, but Cu100 and Cu200 can reach the higher quenching rate and therefore be able to achieve much faster RLS than what in Cu500 and Cu1000. By assuming the mechanism of texture formation is kinetic anisotropy in rapid solidification but turns to thermodynamic anisotropy in extremely rapid solidification, <100> texture formation in Cu100 and Cu200 is caused by thermodynamic anisotropy and by kinetic anisotropy in Cu500 and Cu1000. There is no evidence supporting this hypothesis.

5.1.6.3 The GD Texture Formation in the Different Metal

The three metal films are compared with their texture formation and the pole figures are listed in Figure 89 and Figure 90, where Cu200 has strong <100> in GD but not in TD, Au200 has a very clear <100> in all GD, TD and ND, and Ag200 has a <114> texture in GD which is far away from Cu200 and Au200.

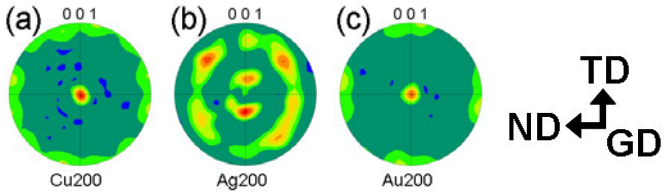

Figure 89. The GD texture formation at RLS=10 μm and with E/E_{CM}=2.3, which is different in different metal films: (a) Cu200 <100>, (b) Ag200 with <114> and (c) Au200 with <100>.

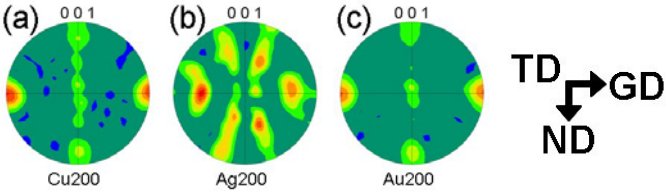

Figure 90. The TD texture formation at RLS=10 μm and with E/E_{CM}=2.3, which is different in different metal films: (a) Cu200 <100>, (b) Ag200 with <221> and <104>, and (c) Au200 with <100>.

As discussed before, the data is consistent with the texture formation in Cu200 and Au200 forming due to thermodynamic anisotropy. During the texture formation process, the grains with <100> texture in GD grow faster than other orientation. At the same time, the grains with <100> texture in TD will expand wider and wider and therefore eliminating the neighbors who have other orientation in TD. As a result, only those grains with <100> in both GD and TD grow faster and are able to expand to much wider than others during RLS.

However, the texture in Ag200 is much more complicated. There are several hypothesis for this special texture formation:

1) The thermodynamic anisotropic orientation is not <100> in Ag films but some other else, such as <114> and so on.
2) Ag films have <100> favored direction but with a huge deviation due to the formation of the super high stacking fault density.

The microstructure of Ag films shows a very high density of stacking faults. It is very possible that the <100> texture is originally formed in Ag films, and then is distorted by the upcoming stacking fault. However, no enough evidences to make any conclusion for the favored GD in Ag films during RLS. In conclusion, the resulted texture in Ag films after RLS is close to <114> GD, being different with Cu and Au.

5.1.6.4 The TD Texture Formation with the Changed Film Thickness

In additional, more characters of RLS can be found comparing the texture formation of TD.

Shown in Figure 91(a) and (b), the strong <110> TD texture is formed in Cu100, and <110> together with <100> textures in TD has been found in Cu200. And the TD texture in Cu500 and Cu1000 (Figure 91(c) and (d)) is dominated by <100> orientation. The increasing intensity of <100> texture in TD with the increasing thickness, again, suggests that thermodynamic anisotropy dominates RLS. And <110> TD appears in thin films, which can not be explained by theories at present.

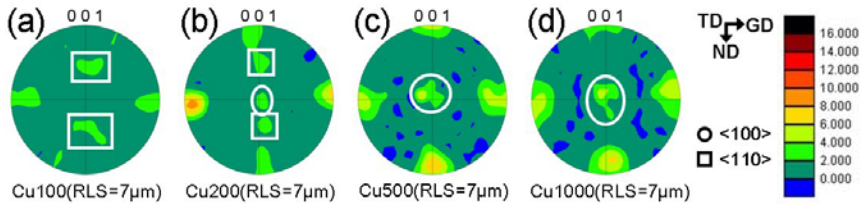

Figure 91. The TD texture formation changes with the different thickness at E/E_{CM}=1.7 in the copper films: (a) Cu100 with <110>, (b) Cu200 with <100> and <110>, (c) Cu500 with <100> and (d) Cu1000 with <100>.

Here it is important that the <100> texture is formed in TD due to the competition of expansion or elimination between the neighbored grains. The grain what has <100> in TD can expand itself by eliminating the neighbors who have other direction in TD. The combination of <100> texture in both GD and TD finally induces <100> texture in ND.

From the texture analysis of GD, TD and ND, the grains with a <100> GD texture grow faster than the other orientation. At the same time, the grains with <100> TD texture will expand wider and wider and therefore eliminate the neighbors who have other orientation in TD. As a result, only those grains with <100> texture in both GD and TD grow fastest and widest than others during RLS, which causes <100> in GD, TD and ND.

5.2 SUMMARY FOR THE MECHANISM OF TEXTURE FORMATION

The mechanism for texture formation in metal films during RLS is summarized below:

1. Thermodynamic anisotropy is amplified by dendritic growth, inducing <100> texture of pure FCC metals during RLS. The grains with <100> in GD can grow fastest, which causes <100> texture in GD. Meanwhile, the grains with <100> in TD can grow widest and eliminate the neighbors, which causes <100> texture in TD. As a result, only those grains with <100> in GD, TD and ND can succeed during RLS competition.
2. Impurity and dislocation formation can affect texture formation and drive the growth direction from <100> to random.
3. Cu500 and Cu1000 have strong <100> in GD, TD and ND where kinetic anisotropy dominates the texture formation and there is little distortion by stress.
4. Cu100 and Cu200 have strong <100> in GD but with <100> and <110> in TD and ND, while Cu500 and Cu1000 have strong <100> in all GD, TD and ND.
5. Au200 follows the same mechanism with copper films during RLS.
6. Ag films have a totally different texture, where GD is close to <114> orientation, and TD and ND are close to <221> and <104> orientations.

6.0 DEFECT FORMATION

6.1 FUNDERMENTALS OF DEFECT FORMATION

The metals formed by rapid solidification are believed to contain many more defects, such as voids, dislocations and stacking faults, than metals formed under equilibrium conditions [59]. These defects, defined as a lattice irregularity having one or more of its dimensions on the order of an atomic diameter [59], typically degrade the electronic properties but sometimes the dislocations can improve the mechanical behavior.

6.1.1 Vacancies (loops) and Dislocations

A vacancy or vacant lattice site, is one where an atom is missing from the lattice (shown in Figure 92), and is the simplest of the point defects [59]. It is impossible to detect such vacancies directly by TEM. After the diffusion process, though, the vacancies prefer to concentrate and form vacant discs, i.e. loops that can be found in TEM analysis, in order to decrease the surface energy of voids.

Due to the lower density of the liquid than that of the solid, the shrinkage of the volume during the solidification requires the diffusion of the vacancies from the solid to the liquid. It is known that the liquid contains free space which will convert to vacancies in the solid. In the rapid solidification, the interface moves faster and traps much more free space of the liquid than those take place in equilibrium. Therefore the number of vacancies formed during solidification can be much greater than the equilibrium number of vacancies N_v, which is given by [59]

$$N_v = N \exp\left(-\frac{Q_v}{k_B T}\right) \qquad \textbf{Equation 16}$$

where V is the total number of atomic sites, Q_v is the energy required for the formation of a vacancy, T is the absolute temperature in Kelvin and $k_B = 1.38\times10^{-23}\, J/atom\cdot K = 8.62\times10^{-5}\, eV/atom\cdot K$ is the gas or Boltzmann's constant.

Dislocations, linear or one-dimensional defects around which some of the atoms are misaligned [59], are another important defect in materials. In general, dislocations can be separated into two categories: edge dislocations where an extra half-plane of atoms terminates within the crystal (shown in Figure 93(a))

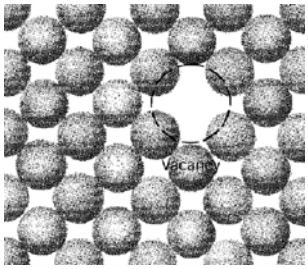

Figure 92. Two-dimensional representation of a vacancy. [59]

and screw dislocations where a half region is shifted one atomic distance relative to the other part (shown in Figure 93(b)) [59].

An important question is whether dislocations are generated at the S-L interface during RLS due to the high movement rate or in the solid after RLS due to the high stress induced by the large contraction of the volume. It is impossible to separate these two causes of the formation of the dislocations only by examination of RLS processed microstructure.

If the dislocations are mainly formed by the attachment mistakes, higher solidification velocities should increase the dislocation density. We can change the laser energy for melting or the thickness of the metal film to change the quenching rate, and thus change the solidification velocity. If the dislocations are mainly formed due to the high stress caused by the thermal expansion mismatch between the metal film and the substrate during cooling, an annealing step can be used to remove the stress, or the substrate can be changed to decrease the mismatch between the metal and substrate materials.

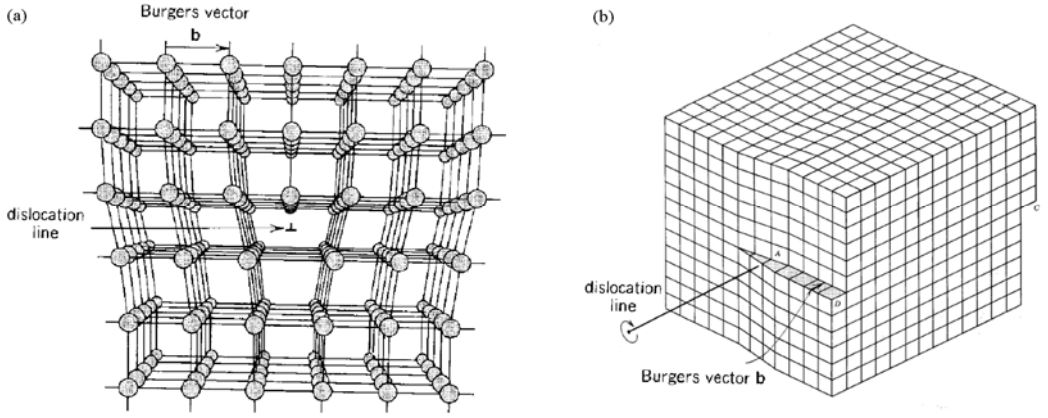

Figure 93. Three-dimensional representation of dislocations: (a) edge dislocation; (b) screw dislocation. [59]

6.1.2 Stacking Faults (SF)

In metals, the atoms are arranged repeated in the lattice position to form crystalline materials. In FCC, there are three kinds of positions (A, B and C) in the {111} plane, called the close-packed plane. The atoms are arranged in the sequence of ABCABC…. (shown in Figure 94(a)) [59]. However, the stacking sequence is not always perfect and sometimes suffers a discontinuity by adding an additional plane, such as ABC |**B**| ABC, or by missing a plane, such as CAB | ABC. As shown in Figure 94(b), this discontinuity in the stacking order of the {111} plane is called stacking fault (SF), and it requires an additional amount of energy (called SF energy). [59]

SF formation is understood very well in solidification processes with low solidification velocity. It is interesting to observe the behavior of SF in rapid solidification processes.

One important question is if SF are generated at the S-L interface during RLS due to the attachment mistakes or in the solid after RLS due to the thermal stress caused by solidification and cooling. Similar to dislocations, if SF are mainly formed by attachment mistakes, higher velocities will increase the SF density. We can change the laser energy for melting or the thickness of the metal film to change the quenching rate, therefore changing the solidification velocity. If SF are mainly formed due to the high stress caused by the different volume change during cooling between the metal film and the substrate, an annealing step can be used to remove the stress, or the substrate can be changed to decrease the difference of the volume contraction between the metal and substrate materials. Some clues have been found by TEM analysis to suggest that most SF in these films appear to have been generated by the latter mechanism.

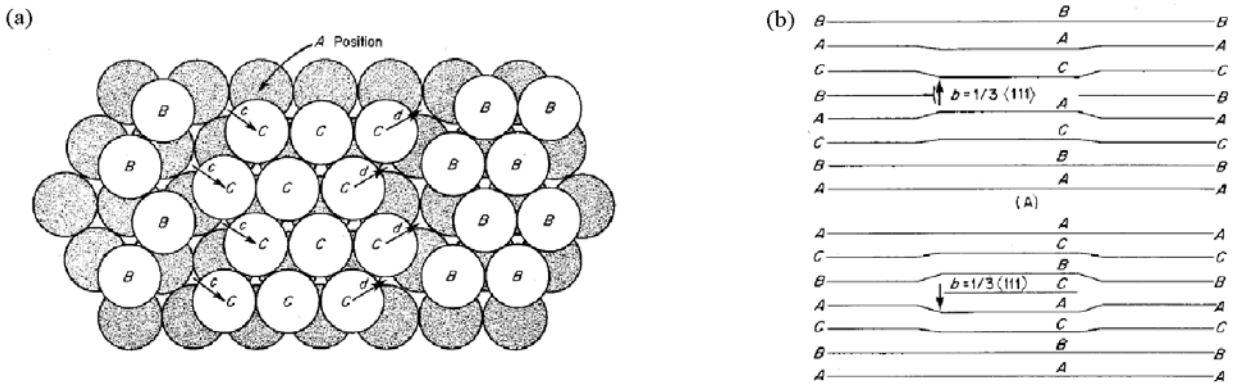

Figure 94. (a) Three kinds of positions (A, B and C) in {111} planes in FCC; (b) SF: discontinuity in the stacking order of {111} planes in FCC. [59]

6.1.3 Grain Boundaries

The grain boundary (GB) is the concentration of dislocations separating two grains or crystals having different crystallographic orientations (orientation mismatch) in polycrystalline materials [59]. GB (shown in Figure 95) are classified as either low-angle grain boundary (LAGB) and high-angle grain boundary (HAGB). LAGB are GB where the orientation mismatch is smaller than 15º and are often associated with dislocation networks, HAGB correspond to the orientation mismatch larger than 15º and can also include twins where the neighboring grains form a special misorientation with the lowest interface energy. [59] The energy of random (not twinned) HAGB is found to be higher than that of LAGB because of the higher density of dislocations.

In RLS, families of grains, the subgrains originating from the same parent grain, were identified and found to be separated by random HAGB. This is likely due to the fact they were generated from differently oriented seeds. But within a family structure, grains separate into several sub-grains during RLS, all of them with similar orientations. These are typically found to be mostly LAGB. By this view, RLS can be looked as a process of decreasing HAGB and increasing LAGB.

The existence of GB will increase the resistivity and eletromigration of metals. However, the effect of single GB is often difficult to measure, given small grain sizes and low electrical resistivity of Ag and Cu. But due to the unique alignment of the formed grains in this research, the resistance of the single GB can be measured by patterning by using E-beam lithography.

In this research, we studied the different effects of HAGB and LAGB on electrical resistance and the mechanism of family formation in RLS.

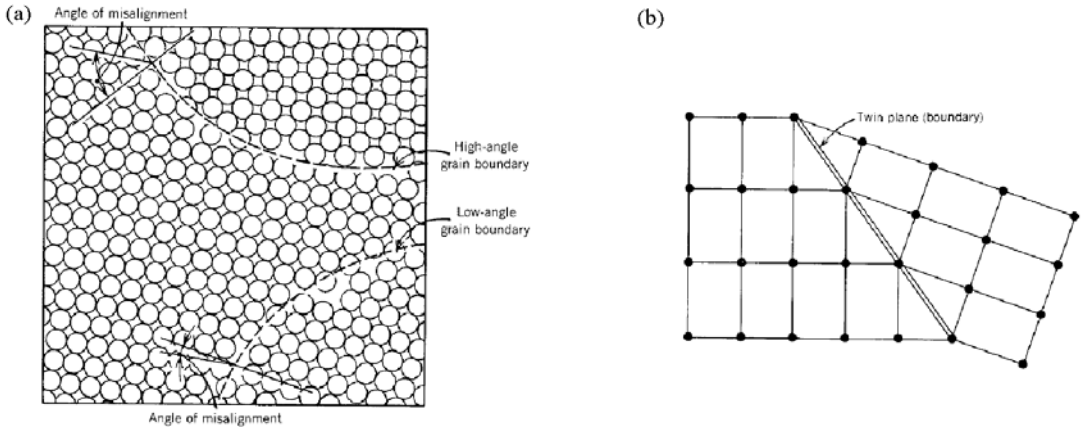

Figure 95. Two-dimensional representation of GB: (a) HAGB and LABG; (b) twin boundary. [59]

6.2 DEFECTS IN RLS GRAINS

It is commonly recognized [43] that large grains with low defect populations have minimum electromigration and low electrical resistance, making this a desirable microstructure for application in electronic devices. It is expected that many defects are formed in RLS processed Cu, Ag and Au films because of the high velocity of solidification and the high stress caused by the shrinkage of the solid metals. Given the need for improved crystallization in applications, a detailed study was completed on the defect density in RLS microstructures to give insights into their formation and suggest ways to lower defect density in the future. And the splintering process involving grain boundary evolution during RLS is discussed, too.

6.2.1 SF Characterized by TEM and SEM

TEM is a powerful tool to study defects, including dislocation lines, loops, stacking faults (SF) and grain boundaries. Examples of these defects are shown in Figure 96 and Figure 97.

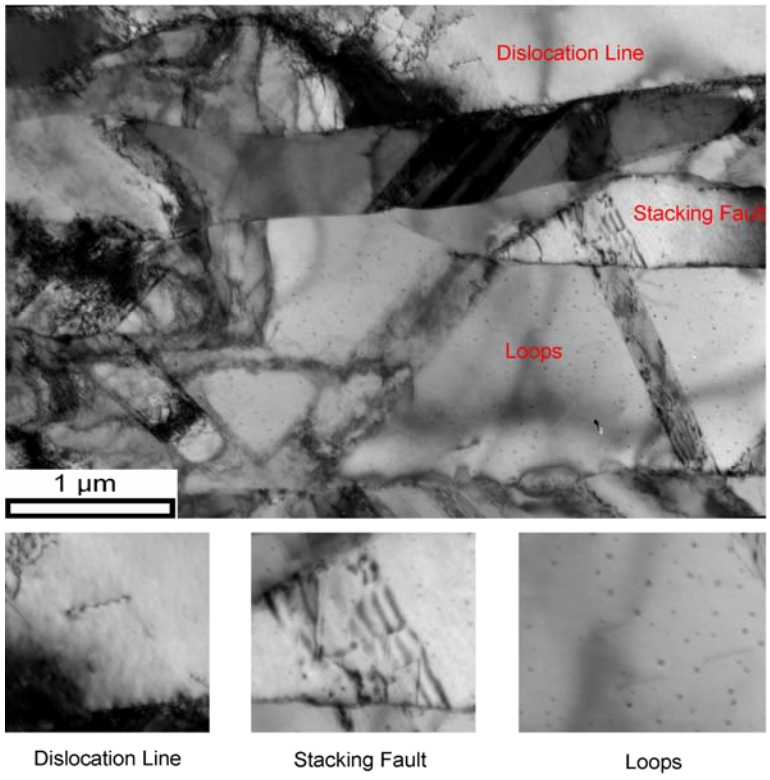

Figure 96. Dislocation line, stacking fault and loops in Cu laterally solidified grain.

It is believed that dislocation loops are mainly produced during the solidification process. These loops result from the collapse of super saturated vacancy clusters trapped in the solid because of the high quenching rate [44,45]. Additionally, it is possible for dislocation lines to be generated at the S-L interface [46].

Stacking faults (SF) are believed to be formed during RLS as a result of misattachment of atoms on the S-L interface due to the very high attached velocity, and after RLS as a result of the high tensile stress in the solid during cooling process.

There is a thermal expansion mismatch in which the metal volume shrinks much more than the substrate with decreasing temperature. After RLS, the SF likely are formed at the GB because of the presence of many dislocations there, and then propagate to the center of the grain due to the high stress (shown in Figure 98). It is believed to be unlikely that SF structures are formed at the S-L interface, especially in Ag films. In many grains such as in Figure 101, stacking faults are found to run across grains forward and backward with respect to the growth direction, and are always connected with at least one end to grain boundaries. This provides evidence that they are much more likely generated in the solid after RLS than in the S-L interface during RLS.

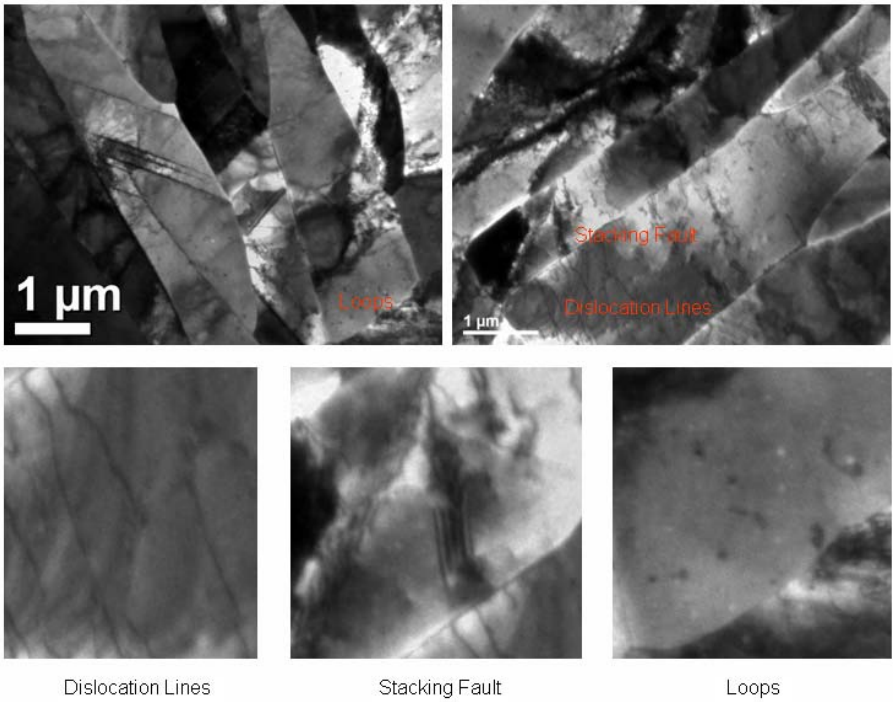

Figure 97. Dislocation lines, SF and loops in Ag laterally solidified grains. Some of Ag loops have been etched away by HF and developed voids.

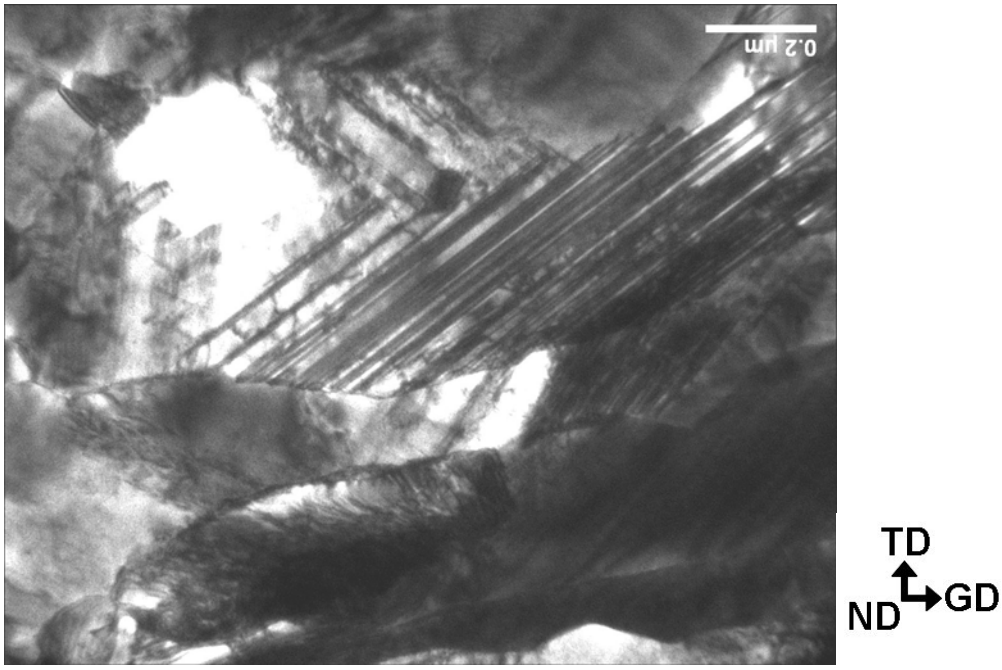

Figure 98. SF form in the GB of Ag and propagate to the center due to the high stress after RLS.

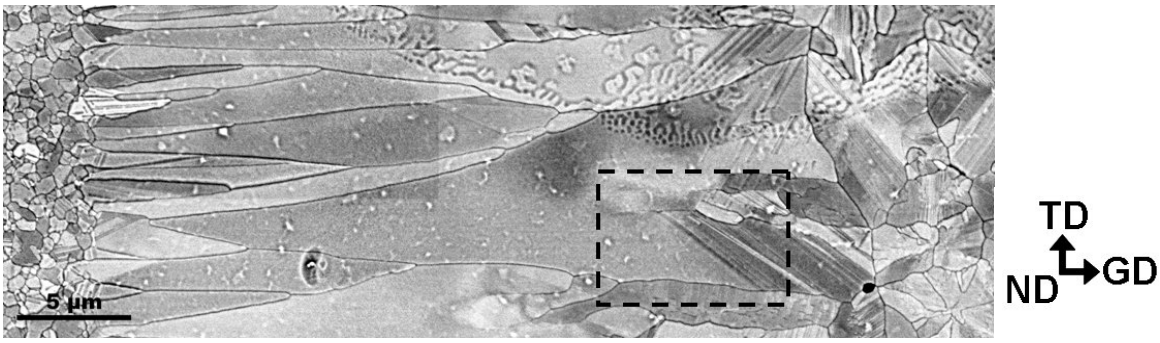

Figure 99. SF form in the splintering position of Cu and propagate to GB during RLS.

However, although it is very hard to see the evidence of the SF formation during RLS, it is still very possible to form a lot of SF in the super rapid solidification, i.e. at the end of RLS. As shown in Figure 99, the SF in the rectangular is very possible to start at the splintering point and then propagate to the GB during RLS, where the SF will not stop at the right end of splintering point if SF are generated from GB. Therefore, these SF is believed to be formed during RLS but no conclusion about this formation yet.

The analysis of the SF density based on the TEM images has been conducted and is shown in Figure 100 and Figure 101. Because the true SF density is somehow related to the SF lines visible in bright field

illumination, these lines are counted and reported in Table 9. The white boxes in Figure 100 are the picked areas analyzed in zone I, II and III for counting in Cu200. It is found that in Cu200 the SF lines in the zone I and II are in the same range, but in zone III forms significantly more SF. Considering that zone I and zone II solidify with lower velocity than zone III, it is reasonable that less SF form and more SF are removed during cooling process in zone I and II.

In Figure 100 the area was analyzed in zone I in Ag200 where the very dense SF lines are formed at the beginning of RLS. This heavy density makes it impossible to count the SF lines very accurately and therefore the comparison between zone I, II and III was not possible.

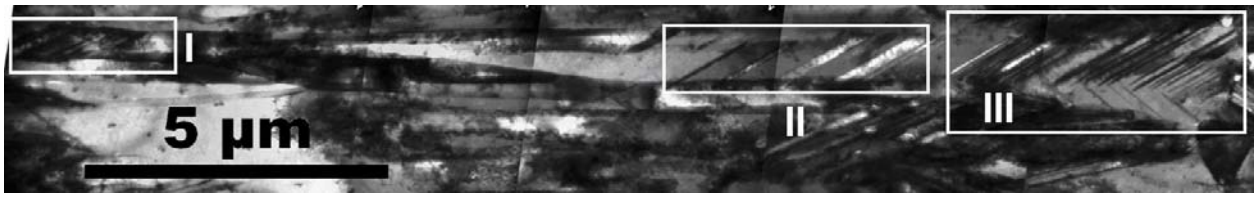

Figure 100. TEM SF analysis for Cu200 (E/E_{CM}=1.6)).

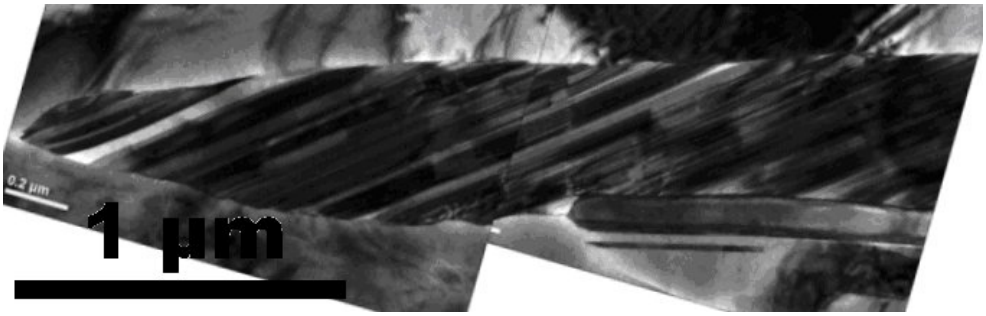

Figure 101. TEM SF analysis for Ag200 (E/E_{CM}=2.3).

The similar analysis of the SF density based on the SEM images has been conducted and is shown in Figure 102. The three white boxes in Cu200 and Ag200 represent the areas analyzed in zone I, II and III for counting. It is found that the SF lines in SEM analysis are much less than what is found in TEM. This is because that SEM is operated at a lower magnification and cannot detect the tiny lines. Also the beam in TEM can penetrate the whole sample but the beam in SEM cannot. So, the information from SEM is less than what from TEM.

The SF lines observed by TEM and SEM in the Cu200 and Ag200 are listed in Table 9, where the error bar is huge in Ag analysis but not be able to estimate. There are three reasons for the absence of the error bar. Firstly, the picked areas are biased where only the areas with sharp SF lines are chosen by the detector for this study. Secondly the picked areas are very limited with only 1~6 areas being analyzed for each number, therefore the sample pool is not big enough to estimate the error bar. Thirdly, the SF lines in Ag200 are too dense to count, which makes problem for the error bar estimation.

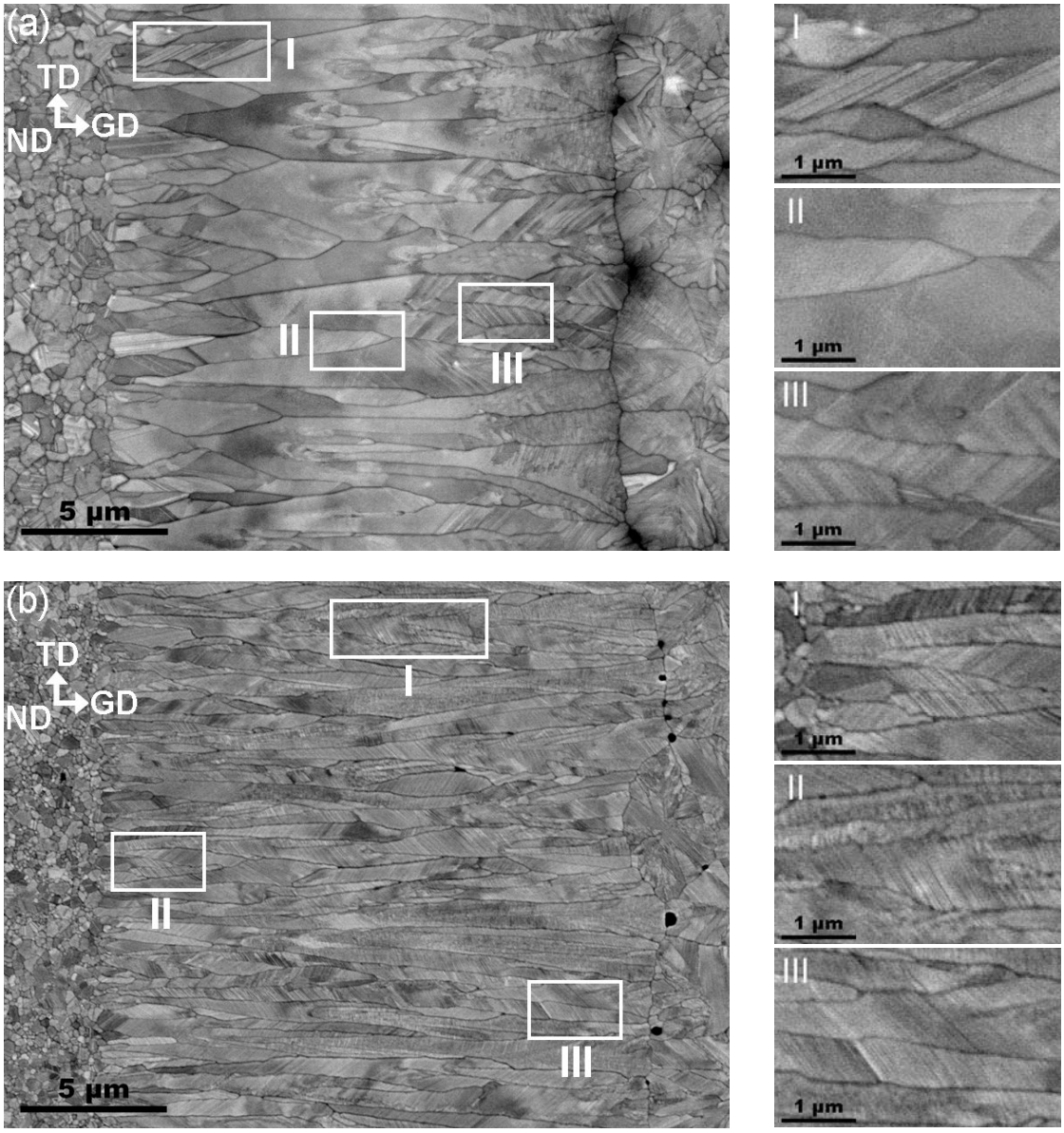

Figure 102. SEM SF analysis for (a) Cu200 (E/E_{CM}=1.7) and (b) Ag (E/E_{CM}=2.3).

Table 9. The number of SF lines, which corresponding to the SF density in Cu and Ag films.

Tool	Material	SF Line Density (in GD) (#/μm)			SF Line Density (in Normal Direction of SF) (#/μm)		
		Zone I	Zone II	Zone III	Zone I	Zone II	Zone III
TEM	Cu200	1.06	1.24	3.75	2.26	2.03	6.39
	Ag200	28.77	42.68	46.53	59.60	65.60	106.29
SEM	Cu200	2.73	2.03	7.50	5.97	3.10	10.61
	Ag200	21.05	20.70	18.82	29.77	24.31	23.92

However, although a lot of problems for SF density analysis, some trends for Cu200 Ag200 can be still concluded by these limited data:

1. In copper films, many more SF lines form in zone III.
2. The SF line density of Ag200 is much higher than that in Cu200. This is consistent with the SF energy of Ag which is in the order of 4X greater than that of Cu.
3. In this work, both TEM and SEM give a similar result. As a result, the following defect analysis is based on SEM data.

6.2.2 SF Formation in Cu, Ag and Au Films

Although the statistic study cannot be conducted at present, SEM microstructure of zone I, II and III was randomly chosen in Cu100, Cu200, Cu500 and Cu1000, and the data are shown from Figure 103 to Figure 106.

Obviously, in every condition such as the different energy ratio and film thickness, the SF line density is the lowest in zone II and highest in zone III. Since RLS grows up from the sputtering grains where the texture (slight <100> in ND and random in GD) is different with the kinetically favored <100> texture in GD and TD, most of grains in zone I grow fast and many SF and dislocations form in order to turn to the favored <100> orientation. It is found that some of grains first form a lot of SF in zone I and suddenly expand themselves to a very wide dimension. This suggests that grains form SF during the process of forming the <100> GD texture in zone I, i.e. SF formation can help strong <100> texture formation in zone I. Most of the SF may be formed during RLS due to the misattachment of the atoms on the S-L interface in this region.

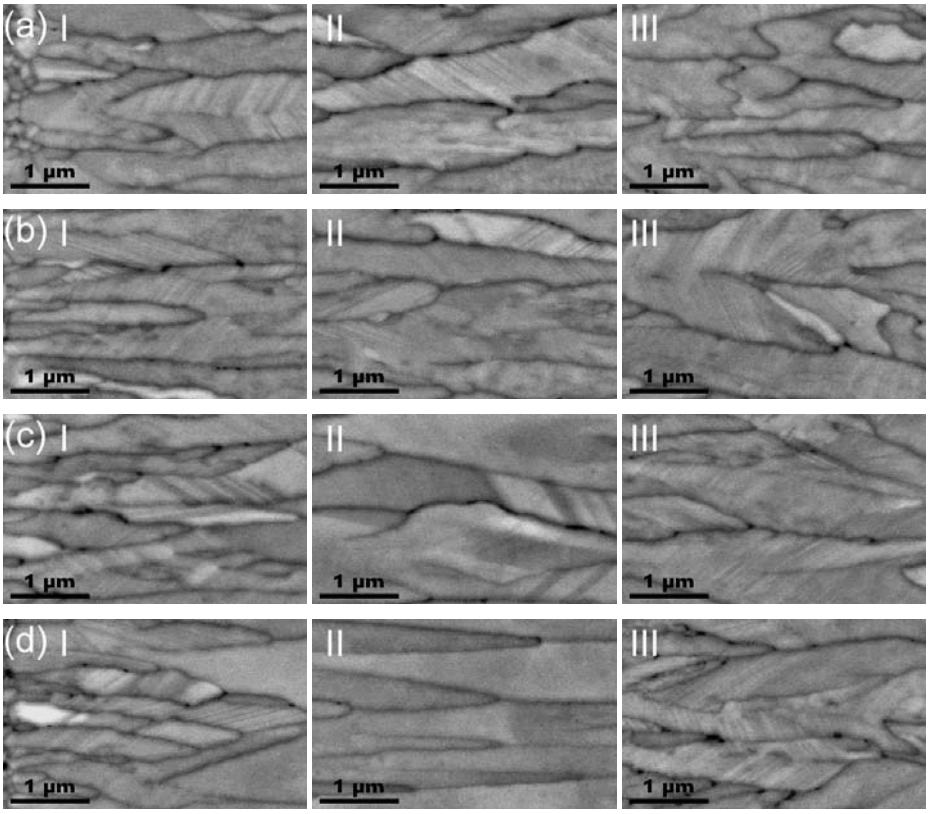

Figure 103. SEM SF analysis for Cu100: (a) E/E_{CM}=1.2, (b) E/E_{CM}=1.7, (c) E/E_{CM}=2.3 and (d) E/E_{CM}=3.0.

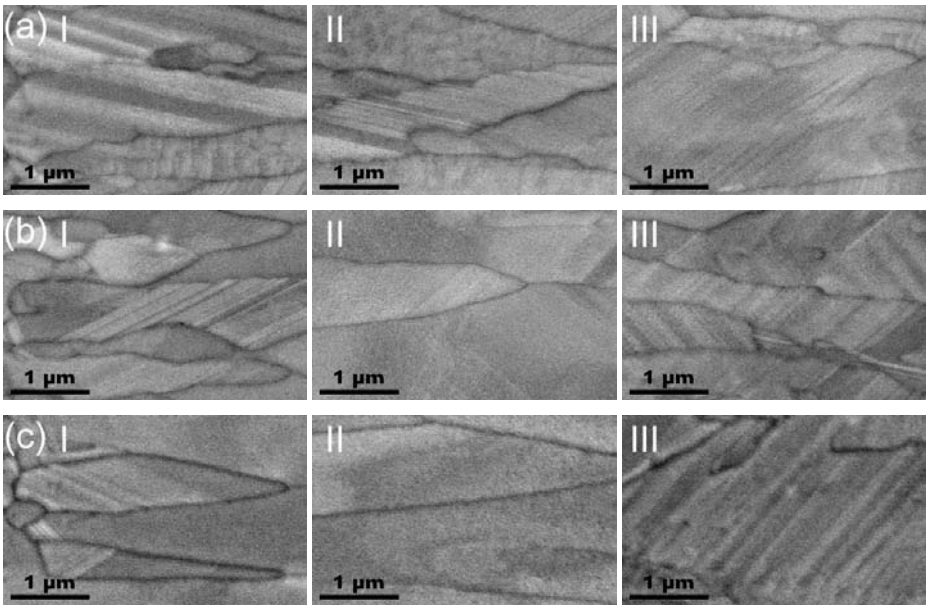

Figure 104. SEM SF analysis for Cu200: (a) E/E_{CM}=1.2, (b) E/E_{CM}=1.7 and (c) E/E_{CM}=2.3.

In zone II most of survived grains from zone I have <100> texture in GD and therefore not much SF formed. The SF formation in this region should be mainly induced by the stress after RLS, which decreases the density of the formed <100> texture.

However, the impurity in copper films leads to zone III, where a lot of SF are formed again. In this region, SF are mainly generated by stress after RLS and also by atom misattachment to the S-L interface due to the super high velocity. The SF formed in zone III will decrease the intensity of the <100> texture.

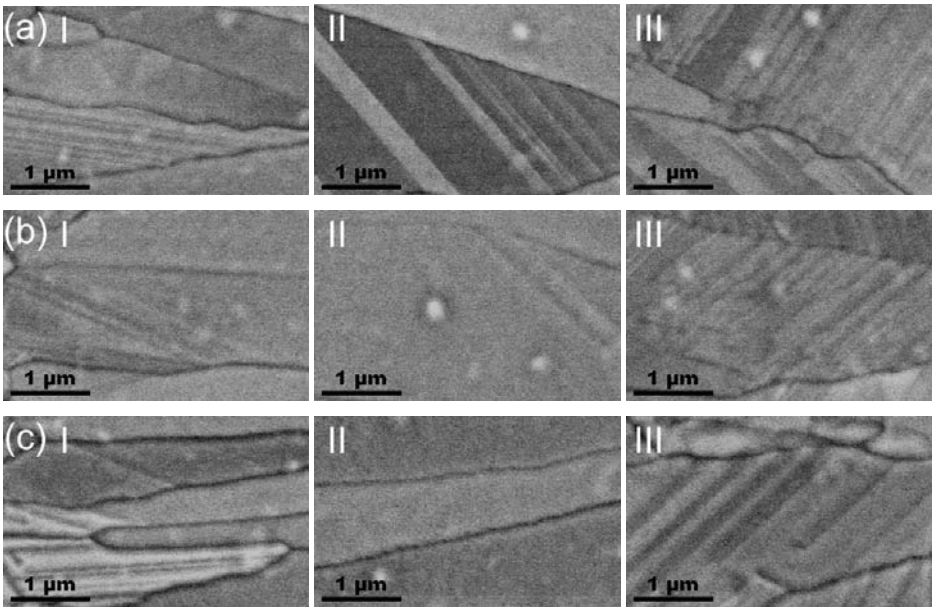

Figure 105. SEM SF analysis for Cu500: (a) E/E_{CM}=1.2, (b) E/E_{CM}=1.7 and (c) E/E_{CM}=2.3.

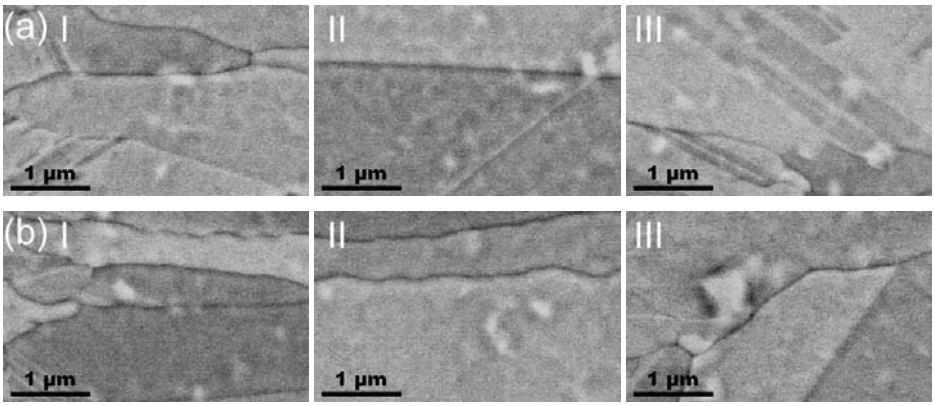

Figure 106. SEM SF analysis for Cu1000: (a) E/E_{CM}=1.2 and (b) E/E_{CM}=1.7.

By comparing the zone II treated by different energy ratio in the same films (shown in Figure 107), the SF lines density is found to decrease with the increasing energy ratio. When the film is treated by a higher energy, more fluence is transferred to the Si substrate before the melted liquid reaches the melting point, therefore the volume mismatch between the copper films and the substrate is less than those treated with lower laser energy. This volume mismatch generates a stress and leads to the SF formation. So, it is reasonable that more SF lines are always formed when treated with a lower energy.

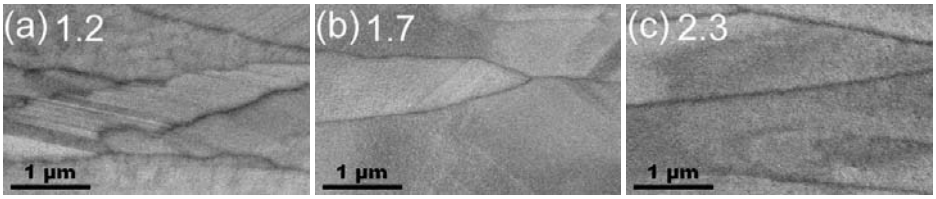

Figure 107. SEM SF analysis for Cu200: (a) E/E_{CM}=1.2, (b) E/E_{CM}=1.7 and (c) E/E_{CM}=2.3.

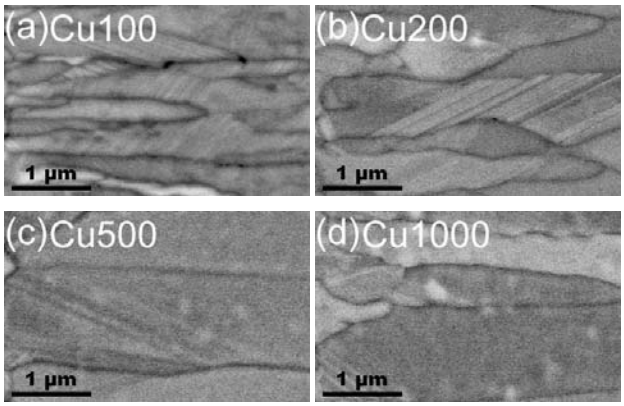

Figure 108. SEM SF analysis for zone I with E/E_{CM}=2.3 in different thickness copper films: (a) Cu100, (b) Cu200, (c) Cu500 and (d) Cu1000.

In addition, SF line densities are found to decrease with the increasing film thickness as shown in Figure 108. When the films are treated by the same energy ratio, the same temperature can be reached even if the thickness is different. However, much more fluence in the thicker films is transferred to the Si substrate before the melting point is reached, and then the volume mismatch is less than those generated in the thinner films. And also the more energy will be absorbed by the SF generated in the thicker films. As a result, the SF line density is the highest in Cu100.

The SF microstructure of Ag100 and Ag200 is shown in Figure 109. Because very heavy SF density is found everywhere in Ag films at each condition and all of them look like that in Figure 109, it was not possible to do any further analysis on Ag films with present method. But obviously most of SF in Ag100 and Ag200 are generated by stress after RLS because of the low SF energy. These huge amounts of SF distort Ag100 and Ag200 a lot and drive the formed texture far away from <100> direction.

The SF microstructure of Au200 is shown in Figure 110. The bubbles and wrinkles formed in Au200 cause problem for the SF analysis. However it is clear that the SF line density in Au films is of the same order of Cu films.

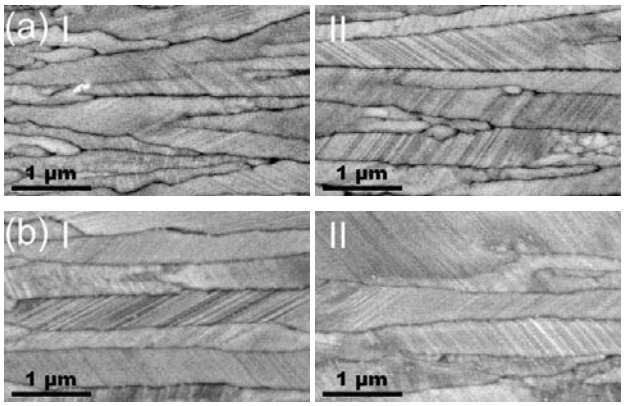

Figure 109. SEM SF analysis for Ag200: (a) E/E_{CM}=1.7 and (b) E/E_{CM}=2.3.

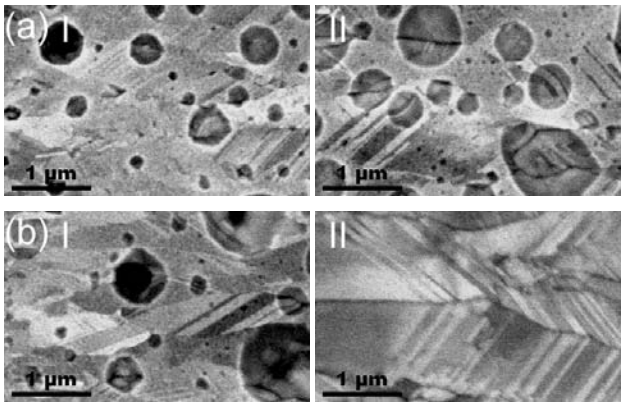

Figure 110. SEM SF analysis for Au2000: (a) E/E_{CM}=1.7 and (b) E/E_{CM}=2.3.

6.2.3 Splintering Process in Cu, Ag and Au Films

The splintering process is during RLS is related with the low angle grain boundary (LAGB) formation, which keeps the mean grain width in zone II in a stable range. The LAGB formed by the splintering process is always stretched in the GD direction, which suggests that the splintering process is formed during RLS. The mechanism is still unclear but is assumed to have relationship with the formation of the dislocations. Here no further discuss on the mechanism but only some observations are noted.

The Figure 111 to Figure 114 show the microstructure of Cu100, Cu200, Cu500 and Cu1000 treated with the energy ratio of 1.2, 1.7 and 2., where the splintering process is found in the circled locations.

Obviously the splintering increases with the increasing energy ratio and decreases with the increasing film thickness. No splintering process has been found in Cu1000, which can explain the continuous growth of the grain width in Cu1000 (the result has been discussed in chapter 4).

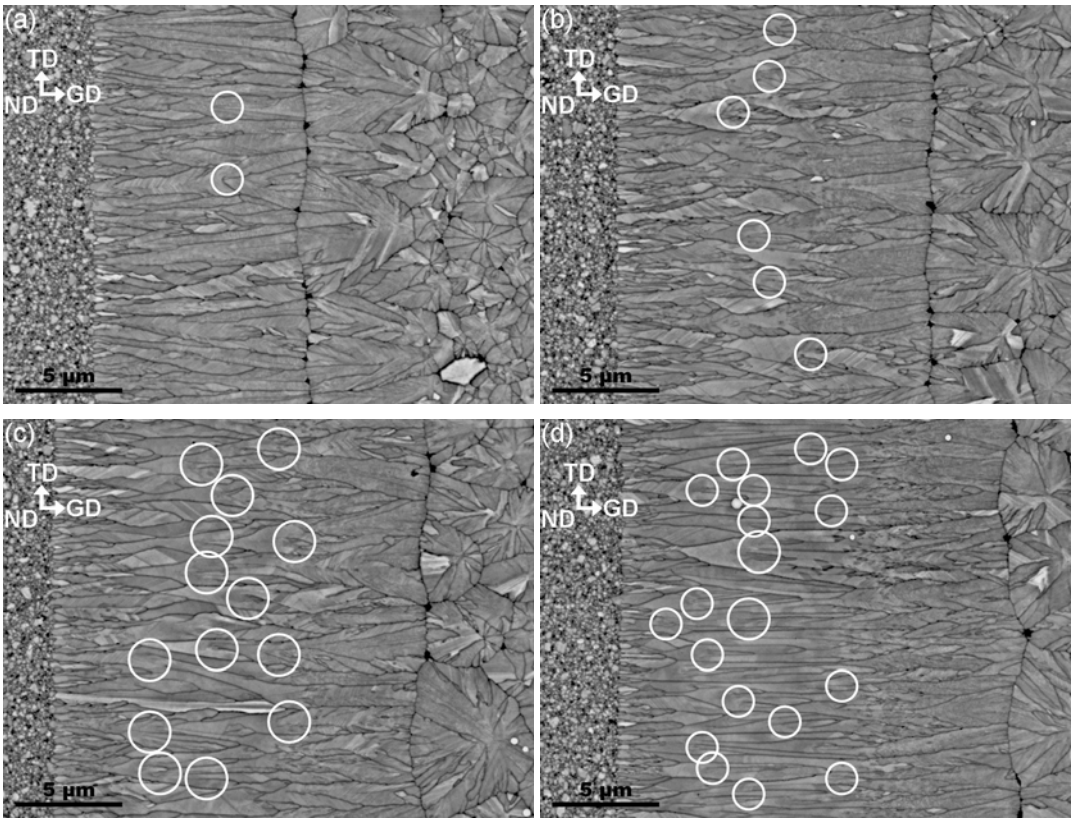

Figure 111. SEM analysis for splintering in Cu100: (a) E/E_{CM}=1.2, (b) E/E_{CM}=1.7, (c) E/E_{CM}=2.3 and (d) E/E_{CM}=3.0.

As seen in Figure 115 and Figure 116, splintering can be found in all RLS conditions for Ag100 and Ag200. Ag can form much more splintering than Cu, which may be the reason of the very small grain width in zone II.

Shown in Figure 117, splintering can be found in Au200 treated with energy ratio of 2.3. No SEM image is provided for the other energy ratio due to the bubbles and wrinkles on the surface.

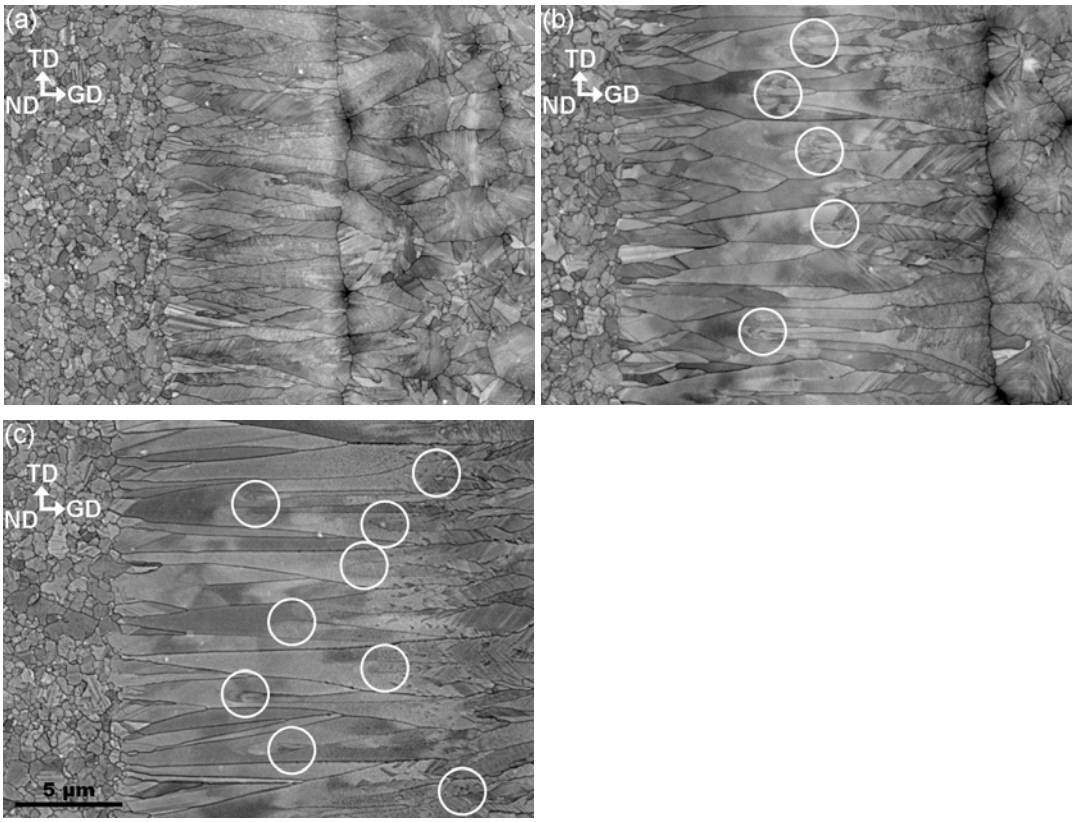

Figure 112. SEM analysis for splintering in Cu200: (a) E/E_{CM}=1.2, (b) E/E_{CM}=1.7 and (c) E/E_{CM}=2.3.

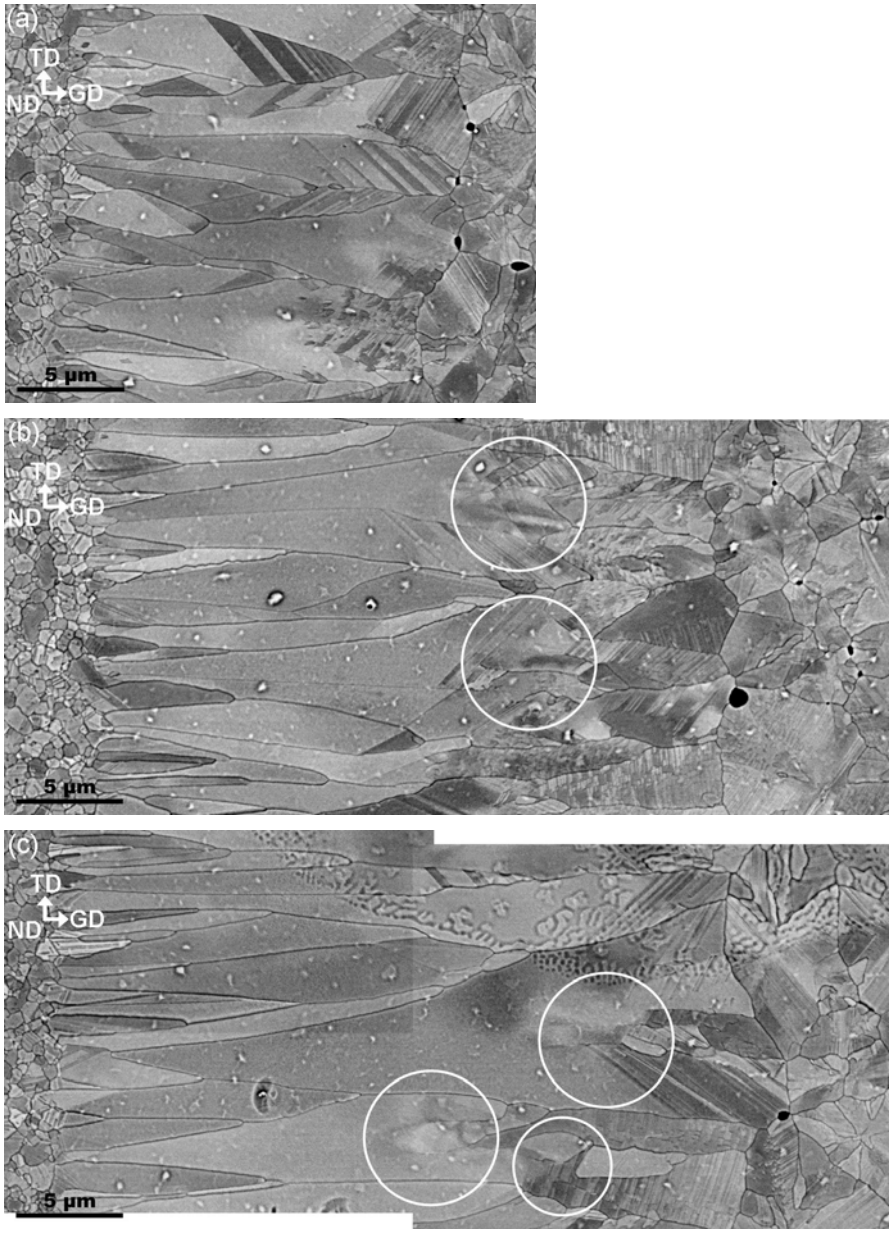

Figure 113. SEM analysis for splintering in Cu500: (a) E/E_{CM}=1.2, (b) E/E_{CM}=1.7 and (c) E/E_{CM}=2.3.

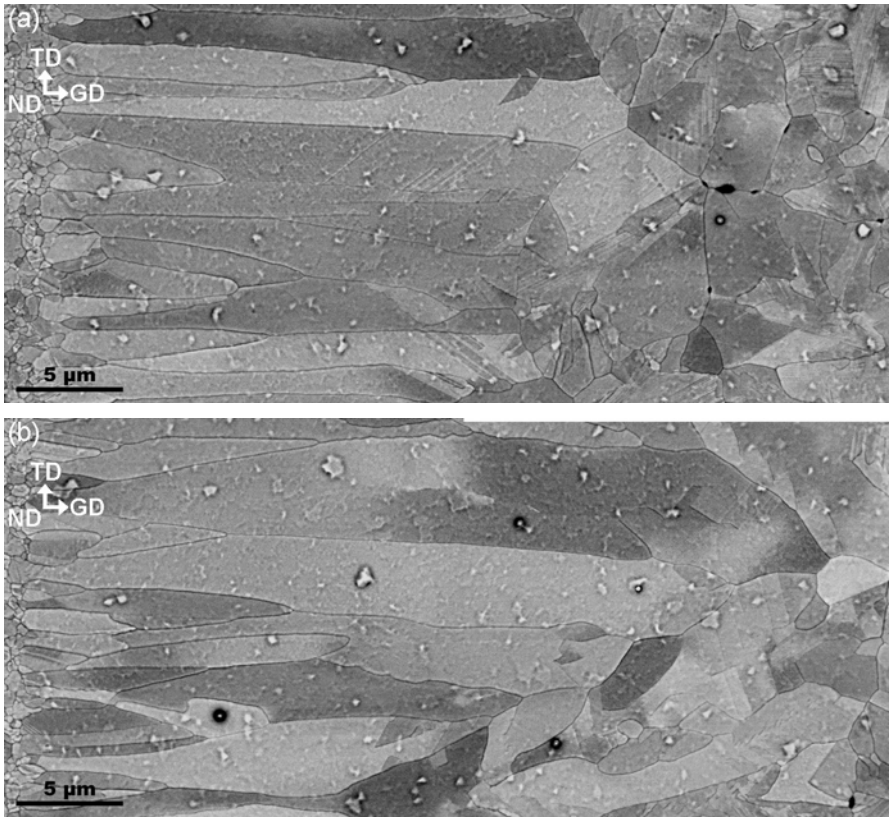

Figure 114. SEM analysis for splintering in Cu1000: (a) E/E_{CM}=1.2 and (b) E/E_{CM}=1.7.

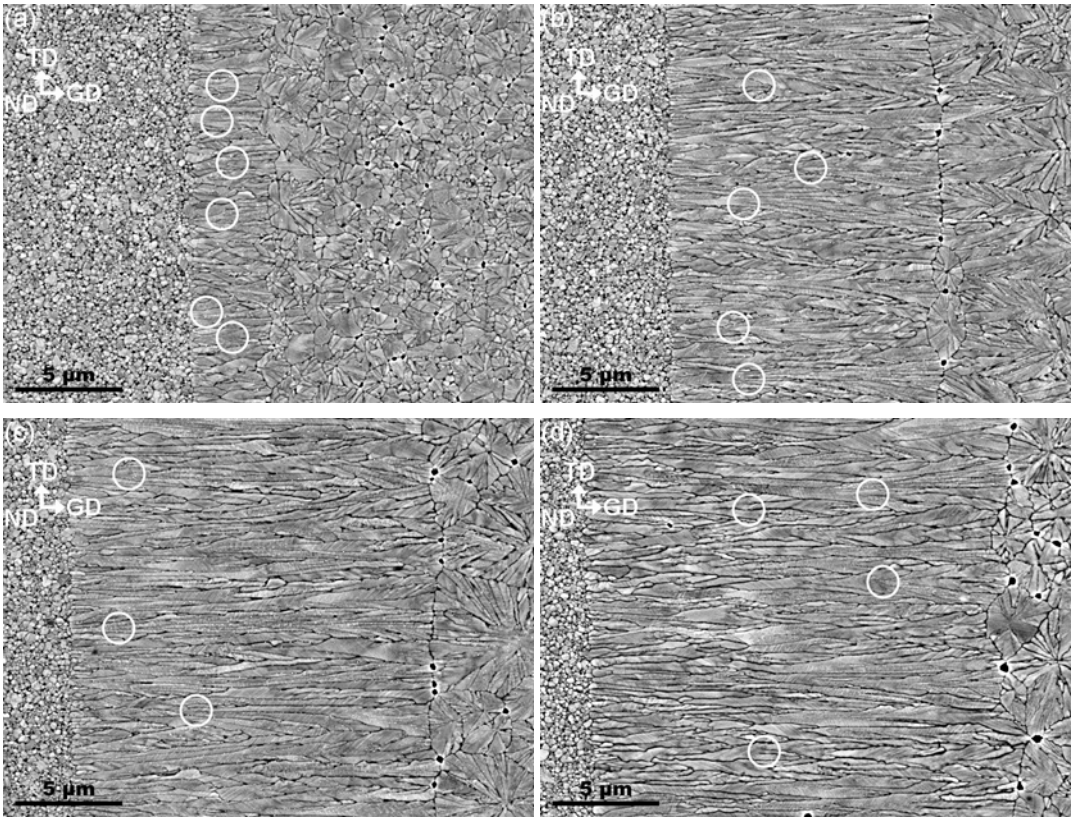

Figure 115. SEM analysis for splintering in Ag100: (a) E/E_{CM}=1.2, (b) E/E_{CM}=1.7, (c) E/E_{CM}=2.3 and (d) E/E_{CM}=3.0.

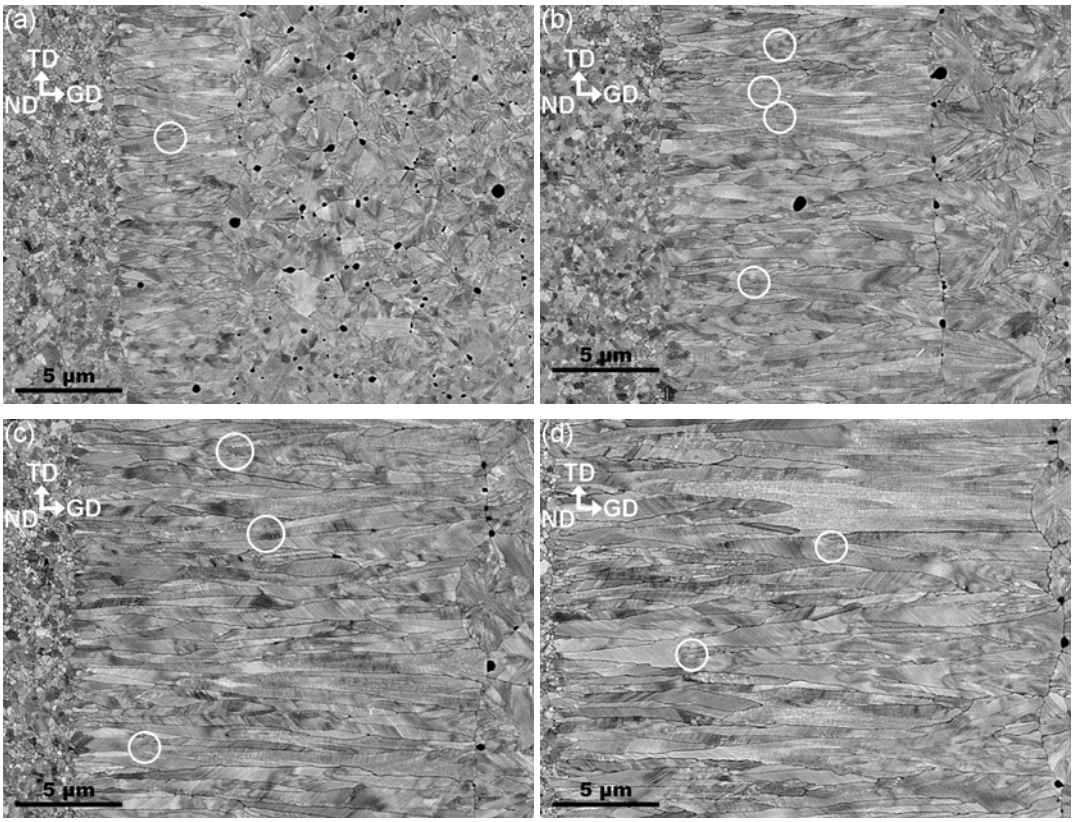

Figure 116. SEM analysis for splintering in Ag200: (a) E/E_{CM}=1.2, (b) E/E_{CM}=1.7, (c) E/E_{CM}=2.3 and (d) E/E_{CM}=3.0.

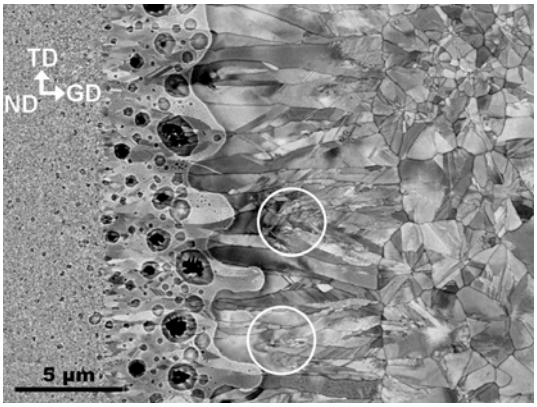

Figure 117. SEM analysis for splintering in Au200: (a) E/E_{CM}=2.3.

6.2.4 Summary

In this chapter, the SF and splintering process are discussed. Combined with the previous experimental results, such as microstructure, grain size and texture formation, some conclusions can be made for this research:

1. The SF in zone I are mainly formed during RLS due to the misattachment of atoms, which helps grains to achieve <100> texture in GD.
2. The SF in zone II are mainly formed after RLS due to the stress, which decreases the texture formation.
3. The SF in zone III are mainly formed not only during RLS due to the high growth velocity, but also after RLS due to the stress, which decreases the texture formation.
4. Splintering is a process to generate LAGB during RLS and maintains a stable grain size in zone II.

7.0 SUMMARY

In this work, the academic question about the mechanism of texture formation in rapid solidification of pure FCC metals has been identified:

1. <100> texture is formed by thermodynamic anisotropy and amplified by dendritic growth during rapid solidification.
2. SF formed at the beginning of RLS accelerates the <100> texture formation, but reduces the <100> texture formation at the later stage of RLS.
3. Large grains with low SF and dislocations can be obtained by increasing the thickness or the input laser energy.

APPENDIX A

GRAIN ORIENTATION ANALYSIS VIA TEM

A.1 CONVERGENT BEAM ELECTRON DIFFRACTION (CBED)

The diffraction contrast images and electron micro-diffraction patterns were collected from representative selections of groups of Cu grains in the RLS region by a convergent beam. Grain orientations relative to the growth direction and film normal were obtained by comparison with computer simulated TEM diffraction patterns and Kikuchi maps (using the software package Desktop Microscopist, Virtual Laboratories).

The formation of Kikuchi pattern is well known as the geometric model shown in Figure 118[63].

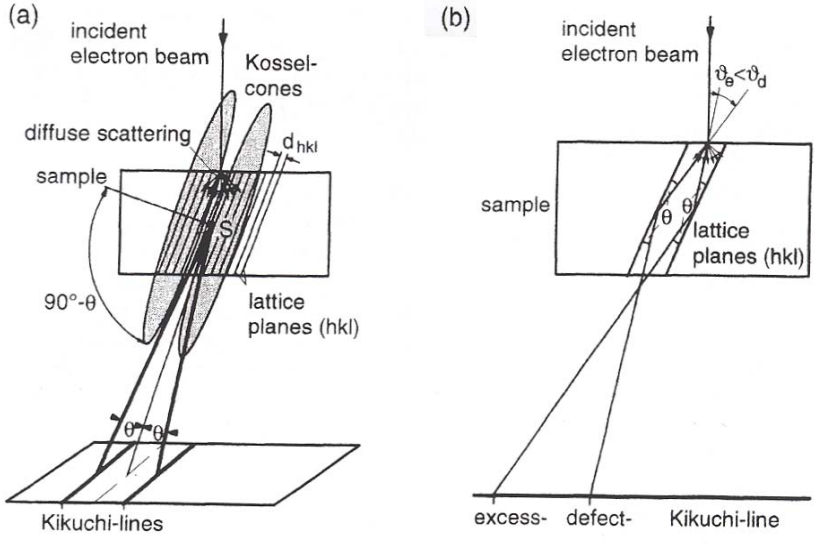

Figure 118. Schematic representation of Kikuchi diffraction pattern formation. [63]

In general, a Kikuchi pattern is similar to Figure 119, where $\overrightarrow{QO}$ is the incident beam, and axis 1, 2 and 3 can be located in the Kikuchi pattern map. The distances of $\overrightarrow{AB}$, $\overrightarrow{AC}$, $\overrightarrow{BC}$, $\overrightarrow{OA}$, $\overrightarrow{OB}$ and $\overrightarrow{OC}$ are measured by hand. Camera Length (L) is given by TEM or can be calculated by:

$$L \approx \frac{AB}{\theta_{axis1,2}} = \frac{AB}{\cos^{-1}\left(\frac{\overrightarrow{axis1}\cdot\overrightarrow{axis2}}{\left|\overrightarrow{axis1}\right|\cdot\left|\overrightarrow{axis2}\right|}\right)}$$

Equation 17

Then, the normal orientation ($\overrightarrow{QO}$) can be determined by:

$$\cos\left(\theta_{OQA}\right) = \cos\left(\tan^{-1}\left(\frac{OA}{L}\right)\right) \approx \cos\left(\frac{OA}{L}\right) = \frac{\overrightarrow{QO}\cdot axis1}{|QA|\cdot|axis1|}$$
$$\cos\left(\theta_{OQB}\right) = \cos\left(\tan^{-1}\left(\frac{OB}{L}\right)\right) \approx \cos\left(\frac{OB}{L}\right) = \frac{\overrightarrow{QO}\cdot axis2}{|QB|\cdot|axis2|}$$

Equation 18

The growth direction of grain ($\vec{G}$) in Kikuchi pattern analysis is rotated and pointed to the right by calibration of images and diffraction pattern. In order to find out $\vec{G}$, $\overrightarrow{OE}$ is added in the Figure 119 which is the normal direction of ΔABQ plane, and $\overrightarrow{OF}$ normal to the ΔACQ plane. α (angle between $\overrightarrow{AB}$ and $\vec{G}$) and β (angle between $\overrightarrow{AC}$ and $\vec{G}$) should be measured.

We can get the direction of $\overrightarrow{AB}$ by:

$$\overrightarrow{AB} = \overrightarrow{EO}\times\overrightarrow{QO} = \left(\overrightarrow{QA}\times\overrightarrow{QB}\right)\times\overrightarrow{QO}$$
$$\overrightarrow{AC} = \overrightarrow{FO}\times\overrightarrow{QO} = \left(\overrightarrow{QA}\times\overrightarrow{QC}\right)\times\overrightarrow{QO}$$

Equation 19

From the geometry properties, $\vec{G}$ can be calculated where $\vec{G}$ can be set as a unit indices:

$$\overrightarrow{QO}\cdot\vec{G} = 0$$
$$\frac{\left|\overrightarrow{AB}\cdot\vec{G}\right|}{\left|\overrightarrow{AB}\right|\cdot\left|\vec{G}\right|} = \left|\cos\alpha\right|$$
$$\frac{\left|\overrightarrow{AC}\cdot\vec{G}\right|}{\left|\overrightarrow{AC}\right|\cdot\left|\vec{G}\right|} = \left|\cos\beta\right|$$

Equation 20

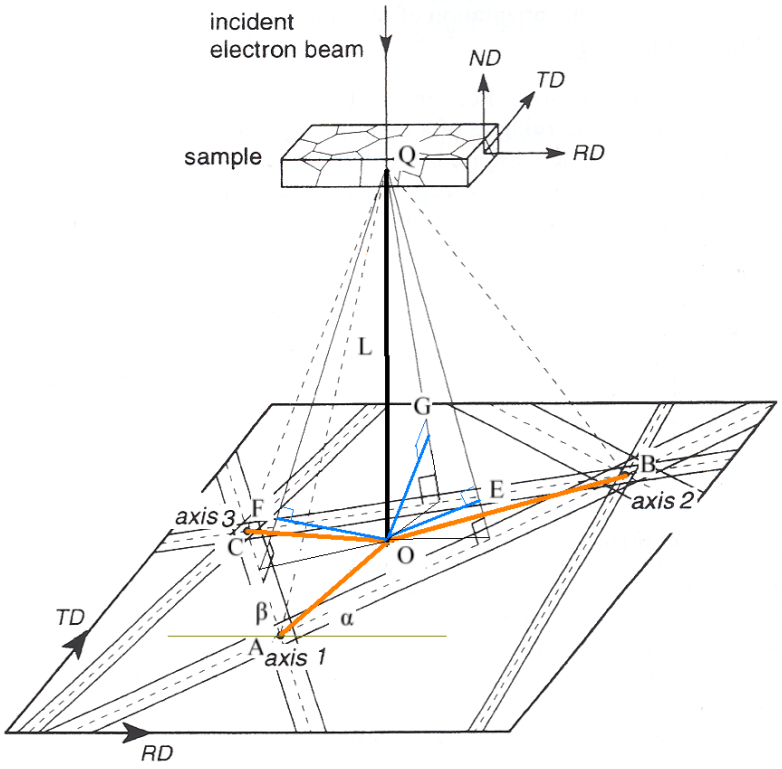

Figure 119. Geometric analysis of Kikuchi diffraction pattern. [63]

A.2 GEOMETRIC MODEL – COORDINATE ROTATION

The directions of $\vec{g}\ \vec{p}\ \vec{n}$ are represented as miller indices in $\vec{i}\ \vec{j}\ \vec{k}$ system of crystals. But in the pole Figure, the miller indices ($\vec{i}\ \vec{j}\ \vec{k}$) of crystals are posted in the coordination of $\vec{g}\ \vec{p}\ \vec{n}$. So, the coordination is changed by the following mathematical method.

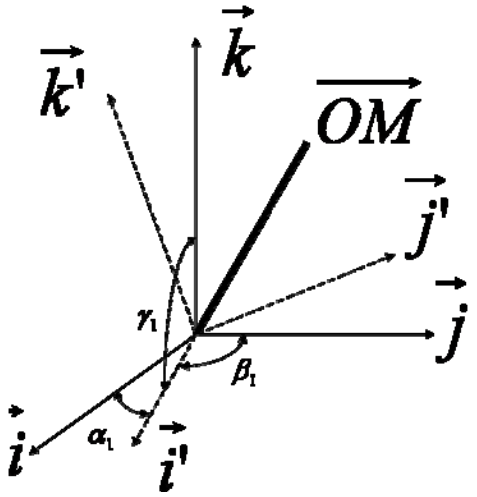

Figure 120. Schematic representation of coordination change. [64]

Table 10. Angles between the new coordination and the initial coordination. [64]

	$\vec{i}$	$\vec{j}$	$\vec{k}$
$\vec{i}'$	α_1	β_1	γ_1
$\vec{j}'$	α_2	β_2	γ_2
$\vec{k}'$	α_3	β_3	γ_3

The initial coordination $\vec{i}\ \vec{j}\ \vec{k}$ changing to a new coordination $\vec{i}'\ \vec{j}'\ \vec{k}'$ is shown in Figure 120 and the angles between the new one and the old one are listed in Table 10.

Then, if $\overrightarrow{OM} = x\vec{i} + y\vec{j} + z\vec{k} = x'\vec{i}' + y'\vec{j}' + z'\vec{k}'$, we can get:

$$\begin{aligned} x &= x'\cos\alpha_1 + y'\cos\alpha_2 + z'\cos\alpha_3 \\ y &= x'\cos\beta_1 + y'\cos\beta_2 + z'\cos\beta_3 \\ z &= x'\cos\gamma_1 + y'\cos\gamma_2 + z'\cos\gamma_3 \end{aligned}$$ **Equation 21**

Also,

$$\begin{aligned} x' &= x\cos\alpha_1 + y\cos\beta_1 + z\cos\gamma_1 \\ y' &= x\cos\alpha_2 + y\cos\beta_2 + z\cos\gamma_2 \\ z' &= x\cos\alpha_3 + y\cos\beta_3 + z\cos\gamma_3 \end{aligned}$$ **Equation 22**

In our experiment, the initial system is $\vec{i} = (100)$, $\vec{j} = (010)$, $\vec{k} = (001)$. The new system is $\vec{g}\ \vec{p}\ \vec{n}$. Then, $\vec{i}'\ \vec{j}'\ \vec{k}'$ represent the coordination of $\vec{i}\ \vec{j}\ \vec{k}$ in $\vec{g}\ \vec{p}\ \vec{n}$:

$$\begin{aligned} \vec{i}' &= \vec{i} = x'_1\vec{g} + y'_1\vec{p} + z'_1\vec{n} \\ \vec{j}' &= \vec{j} = x'_2\vec{g} + y'_2\vec{p} + z'_2\vec{n} \\ \vec{k}' &= \vec{k} = x'_3\vec{g} + y'_3\vec{p} + z'_3\vec{n} \end{aligned}$$ **Equation 23**

From equation, we get:

$$\begin{aligned} &x'_1 = \cos\alpha_1, y'_1 = \cos\alpha_2, z'_1 = \cos\alpha_3 \\ &x'_2 = \cos\beta_1, y'_1 = \cos\beta_2, z'_1 = \cos\beta_3 \\ &x'_3 = \cos\gamma_1, y'_1 = \cos\gamma_2, z'_1 = \cos\gamma_3 \end{aligned}$$, **Equation 24**

Thus, the new $\vec{i}'\ \vec{j}'\ \vec{k}'$ can be represented as:

$$\begin{aligned} \vec{i}' &= \cos\alpha_1 \cdot \vec{g} + \cos\alpha_2 \cdot \vec{p} + \cos\alpha_3 \cdot \vec{n} \\ \vec{j}' &= \cos\beta \cdot \vec{g} + \cos\beta_2 \cdot \vec{p} + \cos\beta_3 \cdot \vec{n} \\ \vec{k}' &= \cos\gamma_1 \cdot \vec{g} + \cos\gamma_2 \cdot \vec{p} + \cos\gamma_3 \cdot \vec{n} \end{aligned}$$ **Equation 25**

BIBLIOGRAPHY

1. D. A. Porter, K. E. Easterling: Transformations in Metals and Alloys (2nd edition); CRC Press, Taylor & Francis Group (2004)

2. Monde A. Otooni (Ed.): Elements of Rapid Solidification; Springer-Verlag Berlin Heidelberg (Germany) (1998)

3. B. L. Jones, G. M. Weston: Orientation Relations Between Dendrites Grown in a Highly Undercooled Melt; Journal of Crystal Growth; vol. 7; p. 143-146 (1970)

4. D. Turnbuli, R. E. Cech: Microscopic Observation of the Solidification of Small Metal Droplets; Journal of Applied Physics; vol. 21; p. 804-811 (1950)

5. T. S. Srivatsan, T. S. Sudarshan: Rapid Solidification of Discontinuously Reinforced Composite Materials; Rapid Solidification of Nonferrous Alloys.

6. M. J. Tenwick, H. A. Davies: The Melt Spinning and Multilayer Deposition of Pure Copper; vol. 63; p. L1-L4 (1984)

7. J. E. Kline and J. P. Leonard: Thin Solid Films; vol. 488; p 306 (2005)

8. D. Walton, B. Chalmers: The Origin of the Preferred Orientation in the Columnar Zone of Ingots; Transactions of the Metallurgical Society of Aime; vol. 215; p. 447-457 (1959)

9. D.T.J. Hurle, Mechanisms of growth of metal single crystals from the melt, Prog. Mater. Sci. 10, 79 (1962).

10. J.A. Spittle, Preferred orientations in cast metals, Mater. Sci. Technol. 21, 546 (2005).

11. Tomoko Goto, Hazime Murakami, Keizo Tanaka, Masamitsu Nagano: Fiber Textures in Copper and Iron Filaments Produced by the Glass Coated Melt Spinning; p. 557-561 (1976)

12. V.G. Sheplevich, Texture of rapidly solidified foils of aluminum, lead, and their alloys, Physics of Metals and Metallography 94, 199 (2002).

13. M. van Rooyen, N. M. van der Pers, L. Katgerman, Th. H. de Keijser, E. J. Mittemeijer: Relation between Solidification Morphology and Texture of Melt-spun Al and Al-alloys; Rapidly Quenched Metals; p. 823-826 (1985)

14. K. Kang, Y.F. Lu, L.H. Lewis, Q. Li, A.R. Moodenbaugh and Y.S. Choi, Large magnetoresistance in rapidly solidified bismuth, J. Appl. Phys. 98, 073704 (2005).

15. A. Hellawell, P. M. Herbert, The Development of Preferred Orientations During the Freezing of Metals and Alloys, Proc. R. Soc. (London) A, 269, 560 (1962).

16. W.J. Boettinger, S.R. Coriell, A.L. Greer, A. Karma, W. Kurz, M. Rappaz and R. Trivedi, Solidification microstructures-- recent developments, future directions, Acta Mater. 48, 43 (2000).

17. M.E. Glicksman and A.O. Lupulescu, Dendritic crystal growth in pure materials, J. Cryst. Growth 264, 541 (2004).

18. A.M. Mullis and R.F. Cochrane, Grain refinement and the stability of dendrites growing into undercooled pure metals and alloys, J. Appl. Phys. 82, 3783 (1997).

19. H. Biloni, W. J. Boettinger: Physical Metallurgy (fourth edition); Elsevier Science BV; p. 704-709 (1996)

20. R.L. Davidchack, B.B. Laird: Direct Calculation of the Crystal–melt Interfacial Free Energies for Continuous Potentials-- Application to the Lennard-Jones System; Journal of Chemical Physics; vol. 118; p. 7651-7657 (2003)

21. E. Burke, J. Q. Broughton, G. H. Gilmer: Crystallization of Fcc (111) and (100) Crystal-melt Interfaces: A Comparison by Molecular Dynamics for the Lennard-Jones System; J. Chem. Phys.; vol. 89(2); p. 1030-1041 (1988)

22. X. Zhang, A. Atrens: Rapid Solidification Characteristics in Melt Spinning; Materials Science and Engineerign; vol. A159; p: 243-251 (1992)

23. W. Pfleging, A. Vörckel, H. Duddek, D. A. Wesner, and E. W. Kreutz: Excimer-laser patterning of copper in LDE (laser dry etching); Applied Surface Science; vol. 109; p. 194-551, (1997)

24. M. Shimada, M. Moriyama, K. Ito, S. Tsukimoto, and M. Murakami: Electrical Resistivity of Polycrystalline Cu Interconnects with Nano-scale Linewidth; J. Vac. Sci. Technol.; vol. A 24; p. 190-194 (2006)

25. S. P. Murarka: Materials Aspects of Copper Interconnection Technology for Semiconductor Applications; Mater. Sci. Technol; vol. 17; p. 749-758 (2001)

26. C. S. Hau-Riege: An Introduction to Cu Electromigration; Microelectronics Reliability; vol. 44; p. 195-205 (2004)

27. C. K. Hu, L.M. Gignac, E. Liniger, C. Detavernier, S. G. Malhotra, and A. Simon: Effect of Metal Liner on Electromigration in Cu Damascene lines; J. Appl. Phys.; vol. 98; p. 124501-124508 (2005)

28. John P. Leonard: Determination of the Absolute Fluence Profile in Pulsed Laser Processing Using Melt-induced Phase Changes in an Amorphous Silicon Thin Film; Review of Scientific Instruments; vol. 77; p. 053101 (2006)

29. J. A. Spittle: Preferred Orientations in Cast Metals; Materials Science and Technology; vol. 21(5); p. 546-549 (2005)

30. V. G. Shepelevich, P. A. Siutsova, E. Yu. Neumerzhytskaya, E. S. Gutko, K. V. Kuckorecko: Texture of Rapidly Solidified Foils of Aluminum and Its Alloys; Journal of Alloys and Compounds; vol. 403; p. 267-269 (2005)

31. G. L. F. Powell, L. M. Hogan: The Undercooling of Copper and Copper-Oxygen; Transactions of the Metallurgical Society of AIME; vol. 242; p. 2133-2138 (1968)

32. David R. Gaskell: Introduction to the Thermodynamics of Materials (3rd edition); Taylor & Francis (1995)

33. Charles Kittel: Introduction to Solid State Physics (7th edition); John Wiley and Sons Inc (1996)

34. E. D. Palik: Handbook of Optical Constants of Solids; Academic Press (1985)

35. J. Emiliano Rubio, Martin Jaraiz, Ignacio Martin-Bragado, Jesus M. Hernandez-Mangas, Juan Barbolla: Atomistic Monte Carlo Simulations of Three-dimensional Polycrystalline Thin Films; vol. 94; p. 163-168 (2003)

36. E. Grant, D.J. Jensen, B. Ralph: A determination of the texture of a directionally solidified sample of high-purity copper; Journal of Materials Science; vol. 21; p. 1688-1692 (1986)

37. D. A. West, B. L. Adams: Analysis of Orientation Clustering in a Directionally Solidified Nickel-based Ingot; Metallurgical and Materials Transactions A; vol. 28; p. 229-236 (1997)

38. G. F. Boilling, J. J. Kramer, W. A. Tiller: Preferred Orientations Developed During the Solidification of High-Purity Lead; Transactions of the Metallurgical Society of AIME; vol. 227; p. 47-51 (1963)

39. S. M. Copley, D. Beck, O. Esquivel: Laser Melt Quenching and Alloying; AIP Conf. Proc.; vol. 50; p. 161-172 (1978)

40. J. Eric Kline, John P. Leonard: Suppression of Dewetting in Pulsed Laser Melting of Thin Metallic Films on SiO_2; Mater. Res. Soc. Symp. Proc.

41. A. Kulovits, R. Zhong, J. M. K. Wiezorek, J. P. Leonard: Electron Microscopy of Geometrically Confined Copper Thin Films after Rapid Lateral Solidification (in press)

42. Martin Rost, Joachim Krug; Coarsening of Surface Structures in Unstable Epitaxial Growth; Physical Review E; vol. 55(4); p. 3952-3957 (1997)

43. M. Y. Yan, K. N. Tu, A. V. Vairagar, S. G. Mhaisalkar, A. Krishnamoorthy: Confinement of Electromigration Induced Void Propagation in Cu Interconnect by a Buried Ta Diffusion Barrier Layer; Applied Physics Letters; vol. 87; p. 261906 (2005)

44. Mats Hillert, Martin Schwind, Malin Selleby: Trapping of Vacancies by Rapid Solidification; Acta materialia; vol. 50; p. 3283-3291 (2002)

45. G. Hennig: Vacancies and Dislocation Loops in Quenched Crystals of Graphite; vol. 36; p. 1482-1486 (1965)

46. K. A. Jackson: The Origin of Dislocations and Sub-structure Arrangements in Copper Single Crystals; Philosophical Magazine; vol. 14; p. 1131-1142 (1966)

47. Ch. A. Gandin, M. Rappaz, D. West, B. L. Adams: Grain Texture Evolution During the Columnar Growth of Dendritic Alloys; Metallurgical and Materials Transactions A; vol. 26; p. 1543-1551 (1995)

48. B. S. Mitin, N. V. Edneral, M. M. Serov, V. B. Yakovlev: Formation of Solidification Textures upon Quenching of Molten Pure Metals on a Rotating Heat Absorber.

49. D. Y. Li, J. A. Szpunar: Surface {111} Fibre Texture of a Strip-Cast Aluminum; Scripta Metallurgica et Materialia; vol. 28; p. 1377-1382 (1993)

50. K.A. Jackson: Kinetic Processes; Wiley-VCH, (2004)

51. K.I. Dragnevski, R.F. Cochrane, A.M. Mullis: The Mechanism for Spontaneous Grain Refinement in Undercooled Pure Cu Melts; Materials Science and Engineering A; vol. 375-377; p. 479-484 (2004)

52. K.F. Kobayashi, P.H. Shingu: The solidification process of highly undercooled bulk Cu-O melts; Journal of Materials Science; vol. 23; p. 2157-2166 (1988)

53. S. E. Battersby, R. F. Cochane, A. M. Mullis: Microstructural Evolution and Growth Velocity-Undercooling Relationships in the Systems Cu, Cu-O, and Cu-Sn at High Undercooling; Journal of Materials Science; vol. 35; p. 1365-1373 (2000)

54. D. Y. Li, J. A. Szpunar: A Possible Role for Surface Packing Density in the Formation of {111} Texture in Solidified FCC Metals; Journal of Materials Science Letters; vol. 13; p. 1521-1523 (1994).

55. W. J. Boettinger, S. R. Coriell, R. Trivedi: Rapid Solidification Processing: Principles and Technologies; Claitor's Publishing, Baton Rouge; p. 13 (1988)

56. Robert F. Cochrane, Sharon E. Battersby, Andrew M. Mullis: The mechanisms for spontaneous grain refinement in undercooled Cu–O and Cu–Sn melts; Materials Science and Engineering A; vol. 304–306; p. 262–266 (2001)

57. Toshio Suzuki, Shigeru Toyoda, Takateru Umeda, Yasuo Kimura: Dendrite Growth from the Supercooled Melt; Journal of Crystal Growth; vol. 38; p. 123-128 (1977)

58. R. Willneker, D. M. Herlach, B. Feuerbacher: Evidence of Nonequilibrium Processes in Rapid Solidification of Undercooled Metals; Physical Review Letters; vol. 62(23);p. 2707-2710 (1989)

59. Robert E. Reed Hill. Physical Metallurgy Principles (2^{nd} Ed). D. van Nostrand Co. (1973), (New York)

60. K. Barmak, A. Gungor, C. Cabral, J. M. E. Harper: Annealing Behaviour of Cu and Dilute Cu-alloy Films- Precipitation, Grain Growth, and Resistivity; Journal of Applied Physics; vol. 94; p. 1605-1616 (2003)

61. K. Sieradzki, K. Bailey, T. L. Alford: Agglomeration and Percolation Conductivity; Applied Physics Letters; vol. 79; p. 3401-3403 (2001)

62. Valerie Randle, Olaf Engler: Introduction to Texture Analysis. CRC Press, Overseas Publishers Association; p. 127-152 (2000)

63. Diguang Wu, Bin Zhang(Ed.): Calculus; Zhejiang University Press; p. 45-47 (1995), Olaf Engler: Introduction to Texture Analysis. CRC Press, Overseas Publishers Association; p. 127-152 (2000)

64. Diguang Wu, Bin Zhang(Ed.): Calculus; Zhejiang University Press; p. 45-47 (1995)